UNIVERSIDAD AUTÓNOMA DE BAJA CALIFORNIA

FACULTAD DE CIENCIAS

MAESTRÍA EN CIENCIAS E INGENIERÍA

"QUANTUM TRANSPORT IN KEKULÉ-MODULATED TWO-DIMENSIONAL MATERIALS"

T E S I S

QUE PARA OBTENER EL TÍTULO DE:

MAESTRO EN CIENCIAS

PRESENTA:

LUIS EDUARDO SÁNCHEZ GONZÁLEZ

Dr. Ramón Carrillo Bastos
Director de Tesis

Dr. Jesús Alberto Maytorena Córdova
Codirector de Tesis

Ensenada, Baja California, México, octubre de 2025

UNIVERSIDAD AUTÓNOMA DE BAJA CALIFORNIA

FACULTAD DE CIENCIAS

"QUANTUM TRANSPORT IN KEKULÉ-MODULATED TWO-DIMENSIONAL MATERIALS"

T E S I S P R O F E S I O N A L

PRESENTA:

LUIS EDUARDO SÁNCHEZ GONZÁLEZ

APROBADO POR:

Dr. Ramón Carrillo Bastos
Director

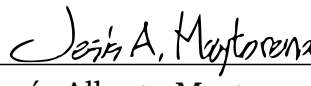

Dr. Jesús Alberto Maytorena Córdova
Co-Director

Dr. Francisco Mireles Higuera
Sinodal

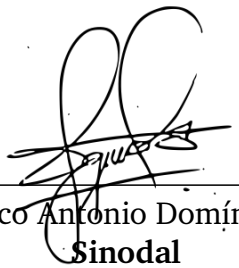

Dr. Francisco Antonio Domínguez Serna
Sinodal

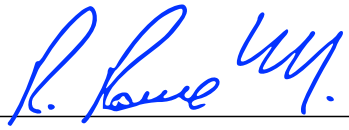

Dr. Roberto Romo Martínez
Sinodal

To my mother, with love.

Acknowledgments

Alone we can do so little;
together we can do so much.
Helen Keller

I would like to express my deepest gratitude to my mother, Gabriela González, and my brother, Nicolás Sánchez, for their unconditional support, patience, and love throughout my master's studies. To Katheri Guardiola, thank you for your companionship during this journey, for listening to me, and for your unwavering encouragement. Above all, to my mother, Gabriela, thank you for your tireless effort, for always providing me with a dignified life, and for giving me the opportunity to pursue my education. Words fall short to express how grateful I am for all that you have done for me. *All my achievements are dedicated to you.*

I am also sincerely thankful to my friends in Ensenada. In particular, Edmundo, thank you for your constant support and for making my experience in Ensenada more meaningful and enjoyable. Your help over these two years has truly been invaluable. To my friends in Saltillo, thank you as well for your enduring support from afar and for keeping in touch despite the distance.

My deepest appreciation goes to Dr. Ramón Carrillo, not only for his guidance throughout the development of this thesis but also for his trust, patience, and steadfast support that extended beyond the academic sphere. His mentorship has been fundamental to my formation and will undoubtedly remain a cornerstone of my academic and professional path.

I would also like to extend my gratitude to the members of my thesis committee: Dr. Jesús Maytorena, Dr. Francisco Mireles, Dr. Roberto Romo, and Dr. Francisco Domínguez, for their time, insightful comments, and valuable contributions. I am equally grateful to all the professors who took part in my academic training during the master's program. As Isaac Newton once said, *"If I have seen further, it is by standing on the shoulders of giants."*

Finally, I acknowledge the Consejo Nacional de Humanidades, Ciencias y Tecnologías (CONAHCyT), now the Secretaría de Ciencia, Humanidades, Tecnología e Innovación (SECIHTI), for the financial assistance granted during my graduate studies. Scholarship No. 1275287.

Luis E. Sánchez González
Ensenada, November 25th 2025

“There’s plenty of room at the bottom”
- Richard Feynman

Abstract of the thesis presented by Luis Eduardo Sánchez González as a partial requirement to obtain the degree of Master in Science. Ensenada, Baja California, México, november 2025.

Quantum transport in Kekulé-modulated two-dimensional materials

Two-dimensional materials are promising candidates for the next generation of electronic and optoelectronic devices due to their novel physical properties. Among them, graphene stands out for its exceptional electronic behavior. Beyond pristine graphene, space-modulated materials such as Kekulé-distorted graphene, characterized by a $\sqrt{3} \times \sqrt{3}$ superlattice, exhibit rich valley phenomena. In this work, we study the electronic structure and optical response of Dirac materials featuring Kekulé modulation.

Inspired by representative two-dimensional Dirac systems, we introduce a hybrid model, a α-$\mathcal{T}_3$ model featuring a Kekulé pattern modulation. Such a hybrid system may result from the deposition of adatoms in a hexagonal lattice, where the two sublattices are displaced in the perpendicular direction, like in germanene and silicene. We derive analytical expressions for the energy dispersion and the eigenfunctions using a tight-binding approximation of nearest-neighbor hopping electrons. The energy spectrum consists of a double-cone structure with Dirac points at zero momentum caused by Brillouin zone folding and a doubly degenerate flat band owing to destructive quantum interference effects.

Furthermore, we study the spectrum of intraband and interband transitions through the joint density of states, the optical conductivity, and the Drude spectral weight for three Kekulé phases: Kek-Y, Kek-O, and Kek-α. We identify unique features such as intervalley transitions, multistep conductivity profiles, and a characteristic and tunable absorption window arising from the intervalley response. Additionally, we study the influence of finite temperature, revealing thermal broadening effects and a resonance peak associated with intervalley coupling.

Our findings highlight distinctive signatures in the optical conductivity that may serve as a viable signature for detecting Kekulé periodicity in two-dimensional materials.

Keywords: Dirac materials, Kekulé modulation, optical conductivity.

Abstract approved by:

Dr. Ramón Carrillo Bastos

Thesis Director

Resumen de la tesis presentada por Luis Eduardo Sánchez González como requisito parcial para obtener el grado de Maestro en Ciencias. Ensenada, Baja California, México, noviembre de 2025.

Transporte cuántico en materiales bidimensionales con periodicidad Kekulé

Los materiales bidimensionales (2D) son candidatos prometedores para la próxima generación de dispositivos electrónicos y optoelectrónicos debido a sus novedosas propiedades físicas. Entre ellos, el grafeno destaca por su excepcional comportamiento electrónico. Más allá del grafeno prístino, los materiales modulados espacialmente, como el grafeno con distorsión Kekulé, caracterizado por una superred de $\sqrt{3} \times \sqrt{3}$, presentan una rica física de valle. En este trabajo, estudiamos las propiedades electrónicas y la respuesta óptica de materiales de Dirac con periodicidad Kekulé.

Inspirados en sistemas bidimensionales de Dirac representativos, introducimos un modelo híbrido: el modelo α-$\mathcal{T}_3$ con periodicidad Kekulé. Este sistema híbrido puede originarse a partir del depósito de atomos en la superficie sobre una red hexagonal, en la que los dos subredes están desplazadas en dirección perpendicular, como ocurre en materiales como el germaneno y el siliceno. Derivamos expresiones analíticas para la estructura de bandas y las funciones de onda empleando un modelo de amarre fuerte a primeros vecinos. El espectro de energía exhibe una estructura de doble cono con puntos de Dirac en el centro de la zona de Brillouin, producto del plegamiento de la zona, y una banda plana doblemente degenerada, resultado de la interferencia cuántica destructiva.

Asimismo, analizamos el espectro de transiciones intra- e interbanda a través de la densidad conjunta de estados, la conductividad óptica y el peso espectral de Drude para tres fases Kekulé: Kek-Y, Kek-O y Kek-α. Identificamos características únicas, como transiciones entre valles, perfiles escalonados en la conductividad y una ventana de absorción característica y ajustable, originada por la respuesta intervalle. Además, estudiamos el efecto de la temperatura finita, observando un ensanchamiento térmico del espectro y un pico de resonancia asociado al acoplamiento intervalle.

Nuestros resultados revelan firmas distintivas en la conductividad óptica que podrían servir como indicadores viables para detectar la periodicidad Kekulé en materiales bidimensionales.

Palabras clave: materiales de Dirac, periodicidad Kekulé, conductividad óptica.

Resumen aprobado por:

Dr. Ramón Carrillo Bastos

Director de tesis

Contents

List of Figures

1

Introduction

Carbon is one of the most extensively studied elements and forms the backbone of organic chemistry. Its significance arises from its wide range of applications across different fields, including electronics [1] and medicine [2]. For this reason, theoretical and experimental research on carbon-based materials has become an active area of investigation, playing a central role in nanoscience and nanotechnology [3]. Moreover, carbon exhibits a rich variety of allotropes. Among the most well-known are diamond and graphite (three-dimensional), but during the 20th century, additional forms were discovered, such as fullerenes (zero-dimensional) [4] and carbon nanotubes (one-dimensional) [5].

The existence of two-dimensional crystals at finite temperature was long considered impossible, due to thermal fluctuations destroying long-range positional order. This belief was grounded in the Mermin-Wagner theorem [6], which shows that continuous symmetries cannot be spontaneously broken in one or two dimensions at finite temperature having sufficient short-range interactions. However, in 2004, A.K. Geim and K.S. Novoselov from the University of Manchester reported a two-dimensional carbon structure [7], known as *graphene*, composed of carbon atoms arranged in a hexagonal lattice resembling a honeycomb. This groundbreaking discovery sparked intense interest in this novel material due to its remarkable electronic [8–10], optical [11, 12], mechanical [13, 14], thermal [15], and chemical [16, 17] properties. Consequently, graphene has inspired many scientific studies and led to the emergence of a new class of materials: *two-dimensional materials*.

Beyond its technological potential [18], graphene has sparked deep theoretical interest. A key theoretical interest lies in its novel and distinct electronic and transport properties. In graphene, electrons behave as massless relativistic fermions described by the Dirac equation [8, 19]. This feature makes graphene a bridge between condensed matter physics and high-energy physics [20]. As a result, there has been growing interest in identifying other systems where electrons mimic massless Dirac fermions—collectively known as Dirac materials [21]. Some notable examples include the α-$\mathcal{T}_3$ model [22], graphene with Kekulé distortion [23–25], and the orthorhombic borophene structure

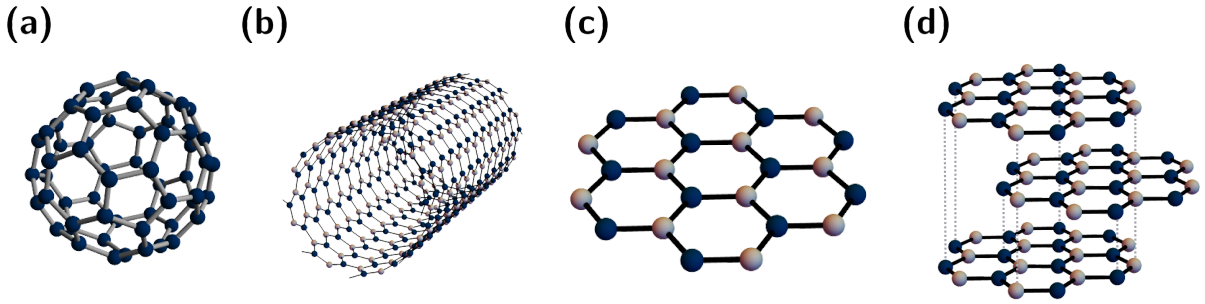

Figure 1.1: Allotropes of carbon. **(a)** Fullerenes (C_{60}) are molecules consisting of wrapped graphene by the introduction of pentagons on the hexagonal lattice. **(b)** Carbon nanotubes are rolled-up cylinders of graphene. **(c)** Graphene is a honeycomb lattice of carbon atoms. **(d)** Graphite can be viewed as a stack of graphene layers.

8-*Pmmn* [26, 27], among others.

Although graphene exhibits remarkable electronic behavior, its gapless band structure presents a fundamental limitation for electronic device applications. The absence of an energy gap between the conduction and valence bands leads to a finite minimal conductivity, making it difficult to switch off electrical current [28]. For this reason, engineering a tunable bandgap is a central goal in graphene-based electronics. One promising approach involves modifying the band structure through external electromagnetic fields, which can induce metal-insulator transitions. For example, circularly polarized light can open a bandgap in graphene's spectrum [29]. A related challenge in probing the spectral properties of Dirac systems is that transport experiments typically require electrical contacts, which may introduce complications. Optical methods offer a powerful alternative, providing access to electronic properties through non-invasive, contact-free measurements. In the case of graphene, numerous optical experiments using electromagnetic radiation have unveiled essential features of its band structure and dynamics [30].

A primary physical property to investigate in a new material is its response to an external electromagnetic field. The optical conductivity, for instance, provides valuable insight into the nature and shape of the energy bands. Other optical properties, such as polarization rotations (known as the Kerr and Faraday effects), also offer information about the band structure and have been widely studied in recent years. Furthermore, in Dirac systems, the valley degree of freedom has been shown to play a significant role in optical phenomena, leading to the emergence of an entirely new research field known as valleytronics [31], which aims to study and manipulate the valley index for applications in electronic and optoelectronic devices [32].

Another promising route to engineer the electronic spectrum of graphene involves modifying its lattice structure through spatial modulation. In particular, spatial bond modulation can induce exotic effects in the electronic properties of two-dimensional materials [33–37]. One of the most interesting examples of spatial modulation is the

Kekulé distortion in the graphene honeycomb lattice [23–25, 38], where the lattice acquires a bond density wave with superlattice unit cell $\sqrt{3} \times \sqrt{3}$ larger than the original unit cell. As a result, Brillouin zone folding brings the K, K' points to the center of the Brillouin zone (Γ point). Experiments suggest two types of Kekulé modulations in graphene with distinct low-energy spectrum [25, 39]: the so-called Kek-Y phase with two Dirac cones with different velocities, and the Kek-O phase with a doubly degenerate massive Dirac band. Several mechanisms have been proposed to generate phases with different Kekulé distortions, such as surface atom adsorption [40–44], electron-phonon interactions [45, 46], electron-electron interactions [47, 48], biaxial strain [49, 50], and heterostructures [51–53], indicating its ubiquitousness in hexagonal lattices [54]. For instance, the Kek-M phase has been theoretically proposed, where the enlargement of the primitive cell is achieved by periodically adjusting the onsite potential [55–57], suggesting the possibility of realizing other Kekulé-like phases without bond modulation. Theoretical studies have shown that a specific type of Kekulé phase leads to an energy gap, highlighting the importance of identifying the response associated with such a phase [25]. In this context, electrical and optical signatures offer a promising avenue for studying and understanding the mechanism behind the Kekulé phase [56, 58–64].

From a topological perspective, Kekulé-distorted graphene was first proposed as a novel platform hosting fractionally charged topological excitations [34]. Mechanical strain applied to graphene-based heterostructures with Kekulé patterning also gives rise to intriguing topological effects [65]. Moreover, Kekulé distortion is one of the suggested mechanisms behind the superconducting and correlated insulating states behavior in magic-angle twisted bilayer graphene [66–71], further increasing the interest in the study of Kekulé-patterned superlattices.

Beyond lattice distortions such as the Kekulé pattern, another exciting avenue in two-dimensional materials research involves systems with flat bands due to their unique electronic and transport properties, making them ideal platforms for exploring novel physical phenomena [36, 72–81]. The observation of correlated insulator states and signatures of unconventional superconductivity in twisted bilayer graphene [73] has further fueled the interest in systems hosting flat bands close to the Fermi level [82, 83].

Line graphs [75, 84–86], such as the kagome and pyrochlore lattices, along with bipartite lattices like the Lieb and dice lattices [75, 87–89], naturally host flat bands in their energy spectrum thanks to destructive interference between electron wavefunctions. The α-$\mathcal{T}_3$ model [22, 90, 91] is a simple example of flat-band system which continuously evolves between the graphene and dice lattice by modulation of a hopping parameter. Its crystal structure consists of a honeycomb lattice, with an additional site at the center of each hexagon that couples to neighboring atoms with only one of the sublattices, hosting a flat band and Dirac cones close to the Fermi level. Numerous studies are dedicated to unraveling the mechanisms behind the emergence of flat bands in Dirac systems [80, 92, 93] and how they give rise to a variety of quantum phases [94, 95]. The optical response of flat bands has also been studied [96–100], but since the group velocity in these bands vanishes, identifying clear optical signatures in the low-frequency range seems challenging.

In this context, the present thesis aims to study quantum transport in two-dimensional

materials with Kekulé modulation. As the main contribution, we propose a new model, a α-$\mathcal{T}_3$ model featuring a $\sqrt{3} \times \sqrt{3}$ Kekulé pattern modulation (Kek-α) [101]. We focus on analyzing the impact that different Kekulé phases (Kek-Y, Kek-O, and Kek-α) have on the electronic and optical properties of the system. The structure of the thesis is as follows:

- Chapter 2: Two-dimensional Dirac materials. We reviewed the electronic properties of well-known Dirac materials, including pristine graphene, Kekulé-distorted graphene, the α-$\mathcal{T}_3$ model, and buckled honeycomb lattices.
- Chapter 3: Linear optical conductivity. We introduce the basics of linear response theory, emphasizing the Kubo formalism and its application to calculating optical conductivity. As an illustrative example, we present a detailed derivation of the optical conductivity of graphene.
- Chapter 4: Kekulé-modulated $\alpha - \mathcal{T}_3$ model. A hybrid model combining the α-$\mathcal{T}_3$ lattice and Kekulé modulation is introduced and studied. Analytical expressions for the band structure and eigenstates are obtained using a tight-binding approximation.
- Chapter 5: Optical response of Kekulé systems. The optical conductivity of the Kek-Y, Kek-O, and Kek-α phases is computed and analyzed. We discuss the main features that characterize the optical signatures of Kekulé periodicity.
- Chapter 6: Conclusions. Finally, we summarize the main results of this thesis and present a conclusion.

2

Two-dimensional Dirac materials

2.1 Pristine graphene

2.1.1 Lattice geometry

In a graphene lattice, carbon atoms are arranged in a hexagonal pattern forming a crystal structure reminiscent of a honeycomb, as shown in Fig. 2.1(a). This crystal can be viewed as two superimposed triangular Bravais lattice with two atoms per unit cell, labeled A and B [102–105]. The lattice vectors that generate the entire crystal from the unit cell are given by

$$\mathbf{a}_1 = \frac{a}{2}(\sqrt{3}, 3), \qquad \mathbf{a}_2 = \frac{a}{2}(-\sqrt{3}, 3), \tag{2.1.1}$$

where $a \approx 1.42$ Å is the nearest-neighbor distance between carbon atoms. The vectors connecting a site on sublattice A to its three nearest neighbors are

$$\boldsymbol{\delta}_1 = \frac{a}{2}(\sqrt{3}, 1), \qquad \boldsymbol{\delta}_2 = \frac{a}{2}(-\sqrt{3}, 1), \qquad \boldsymbol{\delta}_3 = a(0, -1). \tag{2.1.2}$$

Due to the periodicity of the lattice, the corresponding reciprocal lattice vectors $\{\mathbf{b}_j\}$ satisfy the condition $\mathbf{a}_i \cdot \mathbf{b}_j = 2\pi\delta_{ij}$. Using Eq. 2.1.1, we find

$$\mathbf{b}_1 = \frac{2\pi}{3a}(\sqrt{3}, 1), \qquad \mathbf{b}_2 = \frac{2\pi}{3a}(-\sqrt{3}, 1). \tag{2.1.3}$$

Figure 2.1(b) shows the reciprocal lattice, which also forms a hexagonal structure. The shaded region represents the Brillouin zone (BZ), defined as the Wigner–Seitz cell of the reciprocal lattice. The six corners of the BZ are particularly important, known as the Dirac points [103]. By symmetry, these six points can be reduced to two inequivalent ones, labeled $K_\pm$, given by

$$\mathbf{K}_\pm = \left(\pm\frac{4\pi}{3\sqrt{3}a}, 0\right). \tag{2.1.4}$$

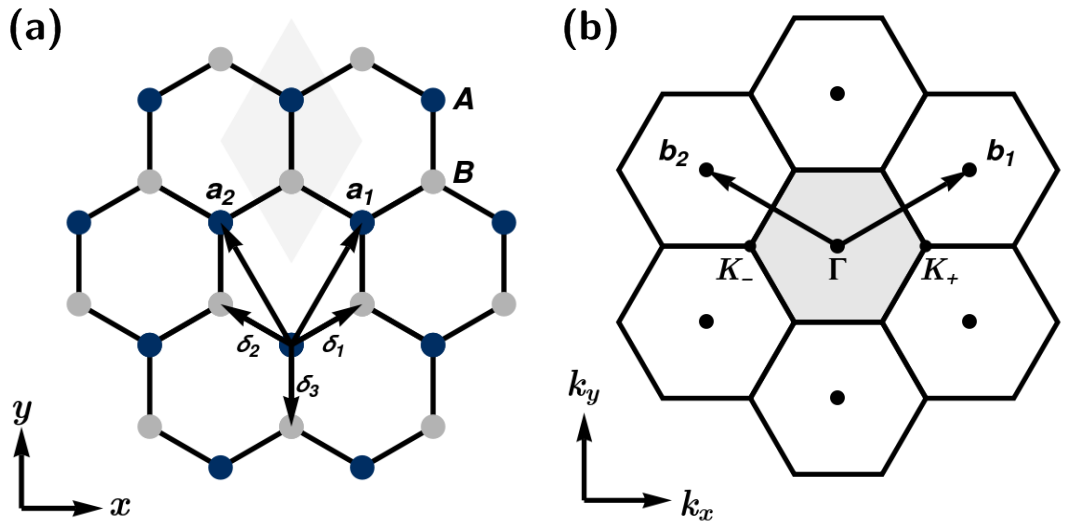

Figure 2.1: (a) Graphene lattice with primitive vectors $\mathbf{a}_1$ and $\mathbf{a}_2$. The vectors $\boldsymbol{\delta}_i$ connect each atom to its three nearest neighbors. The gray parallelogram represents the unit cell. **(b)** Reciprocal lattice of graphene with reciprocal vectors $\mathbf{b}_1$ and $\mathbf{b}_2$. The first Brillouin zone is shown as the gray hexagon.

Simple rotations can generate the remaining corners from $\mathbf{K}_\pm$. These points play a central role in the physics of graphene [8, 103].

2.1.2 Tight-binding model

In its ground state, an isolated carbon atom has the electronic configuration $1s^2\,2s^2\,2p^2$, with six electrons bound to the nucleus, four of which are valence electrons. Carbon can increase the effective number of orbitals available for bonding through a process known as hybridization. In graphene, the $2s$, $2p_x$, and $2p_y$ orbitals hybridize to form three sp^2 orbitals, which generate strong covalent σ bonds between neighboring carbon atoms [3, 102]. These σ bonds give rise to σ bands that lie far below the Fermi energy, as shown in Fig. 2.2(b), and are therefore usually neglected when analyzing the electronic properties of graphene [102, 103].

The fourth valence electron occupies the p_z orbital, which is oriented perpendicular to the plane defined by the σ bonds (see Fig. 2.2(a)). The overlap between adjacent p_z orbitals leads to two π bands, which govern the low-energy electronic excitations in graphene. In the following, we describe the electronic structure of these π bands using a nearest-neighbor tight-binding model.

The tight-binding Hamiltonian for graphene, considering only nearest-neighbor hopping, is given by

$$H = \sum_i \varepsilon_A a_i^\dagger a_i + \sum_j \varepsilon_B b_j^\dagger b_j - t \sum_{\langle ij \rangle} (a_i^\dagger b_j + b_j^\dagger a_i), \tag{2.1.5}$$

where ε_A and ε_B are the on-site energies of the A and B sublattices, and $t \approx 2.7\,\text{eV}$ is the

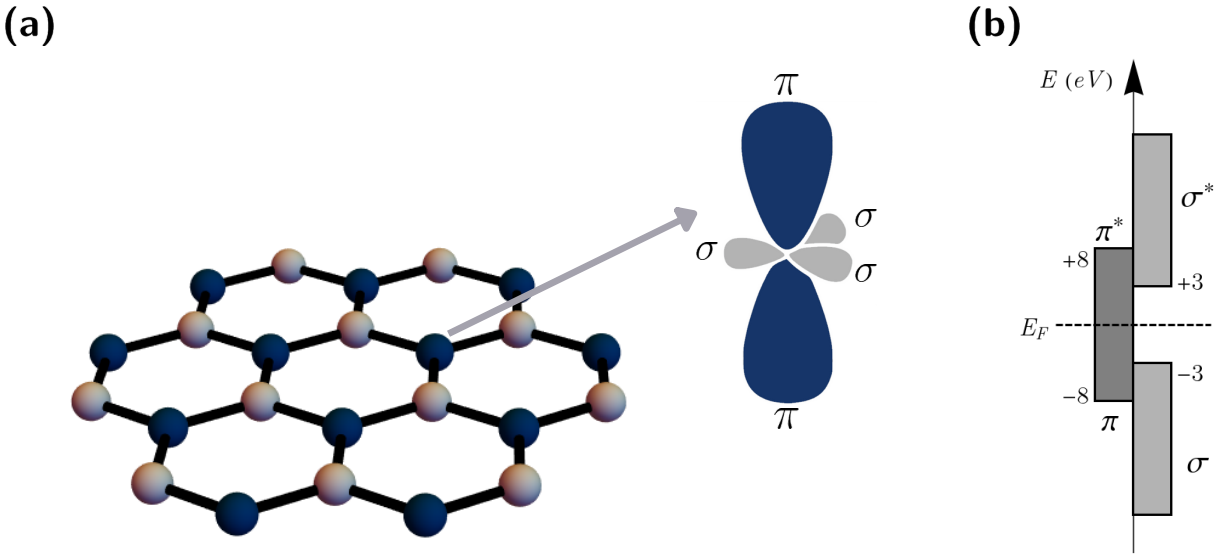

Figure 2.2: **(a)** Graphene lattice and its electronic orbitals. The σ orbitals form strong covalent bonds with neighboring carbon atoms, while the π orbitals are responsible for charge carrier conduction. **(b)** Schematic showing that the π bands lie near the Fermi level E_F, whereas the σ and σ^* bands are separated by a large energy gap. Adapted from [3].

hopping parameter between neighboring p_z orbitals [103]. Since atoms on sublattices A and B are identical, we may set $\varepsilon_A = \varepsilon_B = 0$ without loss of generality, corresponding to a global shift in the energy spectrum.

In terms of the lattice geometry, the tight-binding Hamiltonian for graphene (or any honeycomb lattice) can be written as

$$H = -t \sum_{\mathbf{r}} \sum_{n=1}^{3} a_{\mathbf{r}}^{\dagger} b_{\mathbf{r}+\boldsymbol{\delta}_n} + \text{H.c.}, \tag{2.1.6}$$

where $\mathbf{r}$ runs over the positions of the A sublattice, $\boldsymbol{\delta}_n$ are the vectors connecting each A site to its three nearest B-site neighbors, and t is the nearest-neighbor hopping parameter.

To analyze the system in momentum space, we express the creation and annihilation operators in their Fourier representations:

$$a_{\mathbf{r}} = \frac{1}{\sqrt{N}} \sum_{\mathbf{k}\in \mathrm{BZ}} e^{i\mathbf{k}\cdot\mathbf{r}} a_{\mathbf{k}}, \qquad a_{\mathbf{r}}^{\dagger} = \frac{1}{\sqrt{N}} \sum_{\mathbf{r}} e^{-i\mathbf{k}\cdot\mathbf{r}} a_{\mathbf{r}}^{\dagger}, \tag{2.1.7}$$

where N is the number of unit cells, and $\mathbf{k} = (k_x, k_y)$ denotes the crystal momentum within the Brillouin zone. In momentum space, the Hamiltonian takes the form

$$H = \sum_{\mathbf{k}} \Psi_{\mathbf{k}}^{\dagger} \mathcal{H}(\mathbf{k}) \Psi_{\mathbf{k}} \tag{2.1.8}$$

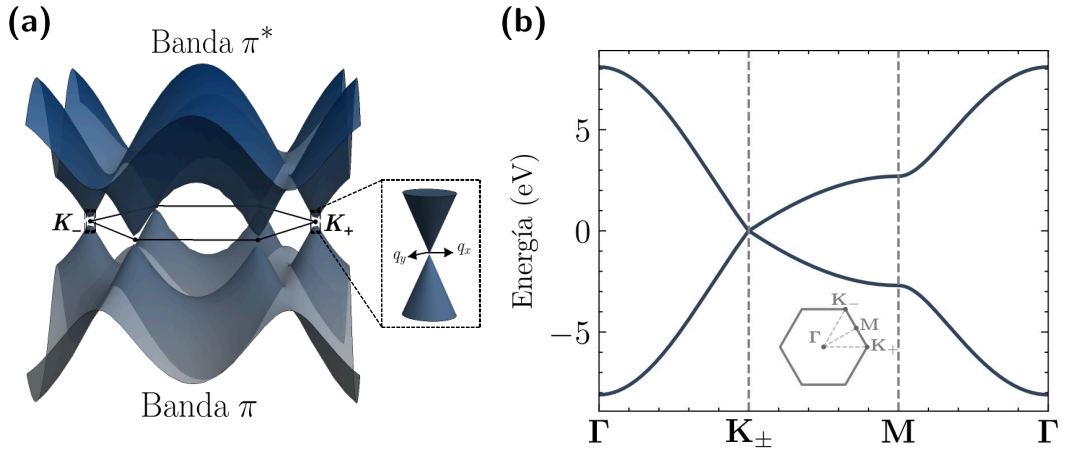

Figure 2.3: (a) Band structure of the π-bands of graphene from the nearest-neighbor tight-binding model. The inset shows the linear dispersion around a Dirac point. **(b)** Dispersion relation along a high-symmetry path in the Brillouin zone, with $t = 2.7\,\text{eV}$.

where

$$\Psi_{\mathbf{k}} = \begin{pmatrix} a_{\mathbf{k}} \\ b_{\mathbf{k}} \end{pmatrix}, \qquad \mathcal{H}(\mathbf{k}) = \begin{pmatrix} 0 & f(\mathbf{k}) \\ f^*(\mathbf{k}) & 0 \end{pmatrix}, \qquad f(\mathbf{k}) = -t \sum_{n=1}^{3} e^{i\mathbf{k}\cdot\boldsymbol{\delta}_n}. \tag{2.1.9}$$

Here $\mathcal{H}(\mathbf{k})$ is the Bloch Hamiltonian and $f(\mathbf{k})$ is the structure factor which encodes the lattice geometry through the nearest-neighbor vectors $\boldsymbol{\delta}_n$.

A compact and insightful way to express the Bloch Hamiltonian is in terms of the Pauli matrices:

$$\mathcal{H}(\mathbf{k}) = \boldsymbol{\lambda}(\mathbf{k}) \cdot \boldsymbol{\sigma}, \tag{2.1.10}$$

where $\boldsymbol{\lambda}(\mathbf{k}) = (\mathbb{R}\text{e}\{f(\mathbf{k})\}, \mathbb{I}\text{m}\{f(\mathbf{k})\})$ and $\boldsymbol{\sigma} = (\sigma_x, \sigma_y)$ are the Pauli matrices acting on the sublattice (pseudospin) space.

The corresponding Schrödinger equation is $\mathcal{H}(\mathbf{k})\,|\psi(\mathbf{k})\rangle = E(\mathbf{k})\,|\psi(\mathbf{k})\rangle$, and upon diagonalization, the energy dispersion relation becomes

$$E_\eta(\mathbf{k}) = \eta |f(\mathbf{k})|, \tag{2.1.11}$$

where $\eta = \pm$ labels the conduction and valence bands. Substituting the explicit form of $f(\mathbf{k})$, the dispersion relation simplifies to the well-known form:

$$E_\eta(\mathbf{k}) = \eta t \sqrt{3 + 2\cos\left(\sqrt{3}k_x a\right) + 4\cos\left(\frac{\sqrt{3}}{2}k_x a\right)\cos\left(\frac{3}{2}k_y a\right)}. \tag{2.1.12}$$

As shown in Fig. 2.3, the π and π^* bands touch at the corners of the Brillouin zone, i.e., $E_\eta(\mathbf{K}_\pm) = 0$, which corresponds to the Fermi level. The band crossing at the Dirac points, characterized by a linear dispersion, identifies graphene as a Dirac semimetal.

Finally, the eigenstates of the system can be parametrized in terms of the vector $\boldsymbol{\lambda}(\mathbf{k})$ as

$$\left|\psi_\eta(\mathbf{k})\right\rangle = \frac{1}{\sqrt{2}}\begin{pmatrix} 1 \\ \eta e^{i\varphi(\mathbf{k})} \end{pmatrix}, \tag{2.1.13}$$

where $\eta = \pm$ is the band index and $\varphi(\mathbf{k}) = \tan^{-1}[\mathbb{I}\mathrm{m}\{f(\mathbf{k})\}/\mathbb{R}\mathrm{e}\{f(\mathbf{k})\}]$ is the azimuthal angle of $\boldsymbol{\lambda}(\mathbf{k})$.

2.1.3 Dirac massless fermions

Many of the physical properties of graphene and related materials are studied in the low-energy regime. In graphene, the low-energy approximation consists of expanding the Hamiltonian around the points $\mathbf{K}_\xi$. Here, the parameter $\xi = \pm$ is introduced to denote the so-called valley index, which distinguishes expressions corresponding to the $\mathbf{K}_+$ and $\mathbf{K}_-$ points, respectively. In Fig. 2.3, it can be seen that the energy bands touch at two points, which correspond to the corners of the Brillouin zone (BZ). Regions far from these points correspond to high-energy states.

At low energies, the Bloch Hamiltonian can be expanded to first order around the $\mathbf{K}_\xi$ points as

$$\mathcal{H}(\mathbf{k}) \approx \mathcal{H}(\mathbf{K}_\xi) + (\mathbf{k}-\mathbf{K}_\xi)\cdot\nabla_{\mathbf{k}}\mathcal{H}(\mathbf{k})\big|_{\mathbf{k}=\mathbf{K}_\xi} + \mathcal{O}(\mathbf{k}^2). \tag{2.1.14}$$

Note that performing a Taylor expansion of a Hamiltonian—or more generally, of a matrix—is equivalent to expanding each of its elements individually. This leads to the expression

$$f_\xi(\mathbf{q}) = \hbar\frac{3t}{2a}(\xi q_x - i q_y), \tag{2.1.15}$$

where $\mathbf{q} = \mathbf{k} - \mathbf{K}_\xi$. Thus, we recover the low-energy Hamiltonian

$$\mathcal{H}_\xi(\mathbf{q}) = \hbar v_F \begin{pmatrix} 0 & \xi q_x - i q_y \\ \xi q_x + i q_y & 0 \end{pmatrix}, \tag{2.1.16}$$

where the Fermi velocity [103] is given by $v_F = \frac{3ta}{2\hbar} \approx 10^6$ m/s, which is constant and independent of energy or momentum. This contrasts with the free-electron case, where the velocity depends on the momentum and the effective mass.

Just like the full Bloch Hamiltonian $\mathcal{H}(\mathbf{k})$, the low-energy Hamiltonian can be written in terms of Pauli matrices:

$$\mathcal{H}_\xi(\mathbf{q}) = v_F\, \mathbf{p}\cdot\boldsymbol{\sigma}_\xi, \tag{2.1.17}$$

where $\mathbf{p} = \hbar\mathbf{q}$ is the momentum measured relative to the $\mathbf{K}_\xi$ points, and $\boldsymbol{\sigma}_\xi = (\xi\sigma_x, \sigma_y)$. The eigenvalue equation $\mathcal{H}_\xi(\mathbf{q})\left|\Psi_\xi(\mathbf{q})\right\rangle = \varepsilon_\xi(\mathbf{q})\left|\Psi_\xi(\mathbf{q})\right\rangle$ yields the low-energy dispersion relation

$$\varepsilon_\eta(\mathbf{q}) = \eta\hbar v_F|\mathbf{q}|, \tag{2.1.18}$$

and the corresponding eigenstates are

$$\left|\Psi_\eta^\xi(\mathbf{q})\right\rangle = \frac{1}{\sqrt{2}}\begin{pmatrix} 1 \\ \eta e^{i\xi\theta_\mathbf{q}} \end{pmatrix}, \tag{2.1.19}$$

where $\theta_{\mathbf{q}} = \tan^{-1}(q_y/q_x)$ is the azimuthal angle in momentum space.

It is important to note that the dispersion relation in Eq. 2.1.18 closely resembles that of ultra-relativistic particles described by the massless Dirac equation [19]. This implies that, near the six corners of the first Brillouin zone, electrons in graphene behave as massless Dirac fermions [8]. This resemblance is the reason why the points K_+ and K_- are referred to as Dirac points.

Although it is common to treat each valley $\mathbf{K}_\xi$ independently, one can also consider the valley as an internal degree of freedom and combine both valleys into a unified expression. The resulting full low-energy Hamiltonian reads

$$\mathcal{H}(\mathbf{q}) = \begin{pmatrix} v_F \mathbf{p}\cdot\boldsymbol{\sigma}_+ & \mathbf{0} \\ \mathbf{0} & v_F \mathbf{p}\cdot\boldsymbol{\sigma}_- \end{pmatrix}. \tag{2.1.20}$$

This Hamiltonian describes low-energy electrons in graphene and strongly resembles the Dirac Hamiltonian, with the Fermi velocity replacing the speed of light. In analogy with relativistic quantum mechanics, the Pauli matrices here act not on real spin, but on the sublattice (A/B) and valley degrees of freedom—this is referred to as pseudospin [106, 107]. Another useful analogy lies in the band index $\eta = \pm$, which plays the role of particle type: a carrier in the conduction band (+) behaves as a particle, while one in the valence band (−) behaves as an antiparticle, commonly referred to as a hole.

2.2 Kekulé-distorted graphene

A density wave (DW) is a phase of matter characterized by a spatial modulation of a physical quantity, such as charge, spin, or bond strength, often accompanied by a periodic lattice distortion [108]. In graphene, such a distortion can emerge in the form of a bond-order wave where strong and weak bonds alternate periodically across the lattice. This phenomenon, known as the *Kekulé distortion*, has been experimentally realized through several techniques [23, 24, 38].

The Kekulé distortion is that the lattice acquires a bond density wave with superlattice unit cell $\sqrt{3} \times \sqrt{3}$ larger than the original unit cell. As a result, Brillouin zone folding brings the K and K' points to the center of the Brillouin zone (Γ point). Experiments suggest two types of Kekulé modulations in graphene: the so-called Kek-Y pattern characterized by a bond configuration resembling 'Y'-shaped motifs in the hexagonal lattice, and the Kek-O pattern features a more symmetric 'O'-like distribution of alternating bonds, reminiscent of the bond pattern in benzene, as shown in Fig. 2.4. These distinct textures result in qualitatively different low-energy electronic behaviors.

The first experimental observation of Kekulé distortion in graphene was reported by Gutiérrez et al., who grew a monolayer of graphene epitaxially on a Cu(111) substrate [23]. In this system, the topmost copper layer exhibits a periodic arrangement of vacancies, which interact with the graphene layer and induce a spontaneous Kek-Y bond modulation [see Fig. 2.4 (a)]. This mechanism is often called the "ghost adatom" effect, as the missing copper atoms mimic the role of virtual adatoms that locally modulate the graphene lattice. On the other hand, the Kek-O phase has been observed under differ-

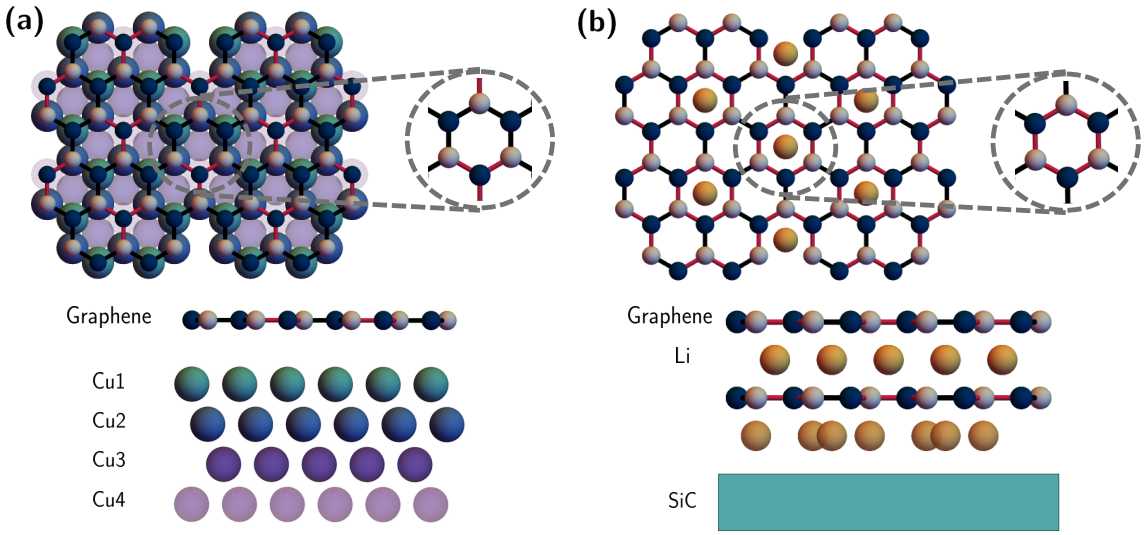

Figure 2.4: (a) Schematic representation of the experimental setup used to induce the Kek-Y distortion in graphene: a monolayer graphene is grown epitaxially on a Cu(111) substrate. Adapted from [23]. **(b)** Setup leading to the Kek-O distortion: Li-intercalated bilayer graphene supported on SiC, where adatoms stabilize the Kek-O pattern. Adapted from [24]. In both, the inset shows the resulting enlarged unit cell of the superlattice.

ent conditions, such as in Li-intercalated bilayer graphene supported on SiC [24] [see Fig. 2.4 (b)] and in mono- and bilayer graphene upon potassium doping [109]. In this case, the Kekulé modulation arises from the presence of adatoms or local strain fields that modify the hopping amplitudes between carbon atoms. This highlights an important distinction: Kek-Y distortions are typically induced by substrate vacancies (ghost adatoms). In contrast, Kek-O patterns are often stabilized by real adatoms that directly modify the carbon–carbon bonding. More recently, it has been observed that placing a graphene monolayer on a SiO_2 substrate can lead to the emergence of both Kek-Y and Kek-O phases, due to local deformations induced in the graphene lattice [39].

From a theoretical standpoint, Kekulé distortions are understood as short-wavelength modulations characterized by wavevectors that connect the inequivalent Dirac points K and K' points, thus inducing intervalley coupling [25, 45, 110]. The bond modulation mimics the Peierls instability in one dimension and can be viewed as a two-dimensional analog of the Su–Schrieffer–Heeger model [111]. A wide range of mechanisms have been proposed to generate Kekulé-ordered phases in graphene and related systems [40–54, 112], indicating its ubiquitousness in hexagonal lattices [54], suggesting the possibility of realizing other Kekulé-like phases without bond modulation.

2.2.1 Real-space formulation

Kekulé textures (Kek-O and Kek-Y) have been theoretically proposed and analyzed within a tight-binding framework [25]. Let us consider the graphene lattice as defined in the

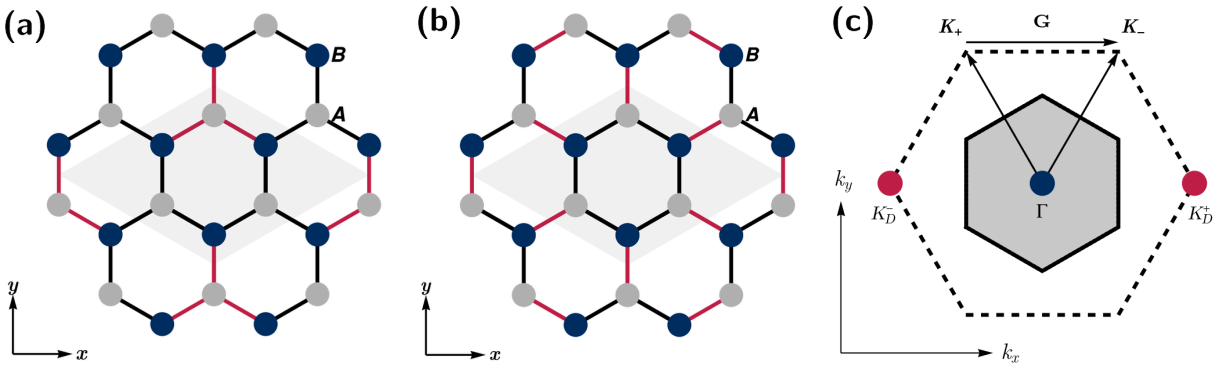

Figure 2.5: Kekulé-distorted graphene in real and reciprocal space. Real-space representation of graphene with **(a)** Kek-Y distortion ($\nu = 1$) and **(b)** Kek-O distortion ($\nu = 0$), where the periodic modulation of strong and weak bonds is illustrated using red and black lines. The gray parallelogram indicates the enlarged unit cell of the Kekulé superlattice. **(c)** Brillouin zone folding in reciprocal space: the original Brillouin zone of pristine graphene (dashed black hexagon) is folded due to the Kekulé modulation. The Dirac points at $\mathbf{K}_+$ and $\mathbf{K}_-$ (red dots) are connected by the Kekulé wavevector $\mathbf{G} = \mathbf{K}_+ - \mathbf{K}_-$, and folded onto the center (Γ) of the mini Brillouin zone (blue dot).

previous section, using the same lattice vectors and nearest-neighbor displacements $\boldsymbol{\delta}_n$. In this setting, the bond modulation can be introduced as a bond-density wave that periodically modulates the nearest-neighbor hopping amplitudes according to the expression:

$$t_{\mathbf{r},n}/t = 1 + 2\mathbb{R}\mathrm{e}\left\{\tilde{\Delta} e^{i(p\mathbf{K}_+ + q\mathbf{K}_-)\cdot\boldsymbol{\delta}_n + i\mathbf{G}\cdot\mathbf{r} - i2\pi(p+q)/3}\right\}, \tag{2.2.1}$$

where $t_{\mathbf{r},n}$ denotes the hopping amplitude between a site at position $\mathbf{r}$ and its nearest neighbor in the direction $\boldsymbol{\delta}_n$, and t is the uniform hopping of pristine graphene. The vector $\mathbf{G} = \mathbf{K}_+ - \mathbf{K}_-$ corresponds to the Kekulé wavevector, which couples the two inequivalent valleys in momentum space. The complex amplitude $\tilde{\Delta} = e^{i2\pi(p+q+m)/3}\Delta_0$ encodes the Kekulé modulation, where Δ_0 is the real-valued modulation strength and $p, q \in \mathbb{Z}_3$, $m \in \mathbb{Z}$. This parameter is often referred to as the Kekulé parameter and determines the type and orientation of the modulation.

To classify the possible textures, it is convenient to introduce the index

$$\nu = 1 + q - p \bmod 3, \tag{2.2.2}$$

which distinguishes between the two main Kekulé patterns: Kek-Y ($\nu = \pm 1$) and Kek-O ($\nu = 0$), as shown in Fig 2.5. Within this framework, the tight-binding Hamiltonian of graphene with a Kekulé distortion takes the following real-space form:

$$H = -\sum_{\mathbf{r}}\sum_{n=1}^{3} t_{\mathbf{r},n} a_{\mathbf{r}}^{\dagger} b_{\mathbf{r}+\boldsymbol{\delta}_n} + \mathrm{H.c.}, \tag{2.2.3}$$

where $a_{\mathbf{r}}^{\dagger}$ and $b_{\mathbf{r}+\boldsymbol{\delta}_n}$ are the creation and annihilation operators for electrons on sublattices A and B, respectively. In the absence of any modulation, i.e., when $t_{\mathbf{r},n} = t$,

this Hamiltonian reduces to the standard tight-binding model for pristine graphene, as introduced in Eq. (2.1.6).

2.2.2 Transformation to momentum space

The Kek-O and Kek-Y superlattices share a hexagonal mini Brillouin zone, whose reciprocal lattice vectors are reduced by a factor of $1/\sqrt{3}$ and rotated by 30° for the original Brillouin zone of pristine graphene [see Fig. 2.6 (c)]. Due to this superlattice periodicity, the Dirac points $\mathbf{K}_\pm$ of unmodulated graphene are folded onto the center of the mini Brillouin zone (Γ point) and coupled by the bond-density wave characterized by the Kekulé wavevector $\mathbf{G} = \mathbf{K}_+ - \mathbf{K}_-$, as shown in Fig 2.6 (c).

We perform a Fourier transform of the tight-binding Hamiltonian. The momentum-space Hamiltonian becomes:

$$\begin{aligned} H = &-\sum_{\mathbf{k}} a^\dagger_{\mathbf{k}} f(\mathbf{k}) b_{\mathbf{k}} - a^\dagger_{\mathbf{k}+\mathbf{G}} \Delta f(\mathbf{k} + p\mathbf{K}_+ + q\mathbf{K}_-) b_{\mathbf{k}} \\ &- a^\dagger_{\mathbf{k}-\mathbf{G}} \Delta^* f(\mathbf{k} - p\mathbf{K}_+ - q\mathbf{K}_-) b_{\mathbf{k}} + \text{H.c.}, \end{aligned} \tag{2.2.4}$$

where $f(\mathbf{k}) = \sum_n e^{i\mathbf{k}\cdot\boldsymbol{\delta}_n}$ is the structure factor corresponding to nearest-neighbor hopping. The crystal momentum $\mathbf{k}$ still varies over the original Brillouin zone. To restrict the description to the reduced Brillouin zone of the superlattice, we introduce a basis that includes the momenta $\mathbf{k}, \mathbf{k} \pm \mathbf{G}$. We define a six-component spinor $\Psi_{\mathbf{k}} = (a_{\mathbf{k}}, a_{\mathbf{k}-\mathbf{G}}, a_{\mathbf{k}+\mathbf{G}}, b_{\mathbf{k}}, b_{\mathbf{k}-\mathbf{G}}, b_{\mathbf{k}+\mathbf{G}})^{\mathrm{T}}$, and write the Hamiltonian in 6×6 matrix form as:

$$H = -\Psi^\dagger_{\mathbf{k}} \begin{pmatrix} \mathbf{0} & \mathcal{F}_\nu(\mathbf{k}) \\ \mathcal{F}^\dagger_\nu(\mathbf{k}) & \mathbf{0} \end{pmatrix} \Psi_{\mathbf{k}} \tag{2.2.5}$$

Here, the off-diagonal block $\mathcal{F}_\nu(\mathbf{k})$ encodes the coupling between the A and B sublattices at different momenta and is given by:

$$\mathcal{F}_\nu = \begin{pmatrix} f_0 & \tilde{\Delta} f_{\nu+1} & \tilde{\Delta}^* f_{-\nu-1} \\ \tilde{\Delta}^* f_{1-\nu} & f_{-1} & \tilde{\Delta} f_\nu \\ \tilde{\Delta} f_{\nu.1} & \tilde{\Delta}^* f_{-\nu} & f_1 \end{pmatrix}, \tag{2.2.6}$$

where $\tilde{\Delta} = e^{i\frac{2\pi}{3}(p+q)}\Delta$ is the complex Kekulé parameter, and the functions $f_n(\mathbf{k})$ are defined as shifted structure factors $f_n(\mathbf{k}) = f(\mathbf{k} + n\mathbf{G})$. The full derivation, including the detailed basis transformation and intermediate steps, is provided in Appendix A.

2.2.3 Low energy Hamiltonian

An effective Hamiltonian for low energies can be obtained considering $\Delta_0 \ll 1$ and by noticing that the rows and columns of the matrix $\mathcal{F}$ associated with modes $a_{\mathbf{k}}$, and $b_{\mathbf{k}}$, lead to high energy bands, thus negligible in the low energy limit. Consequently, in this limit the spectrum is primarily determined by four modes, denoted as $u_{\mathbf{k}} =$

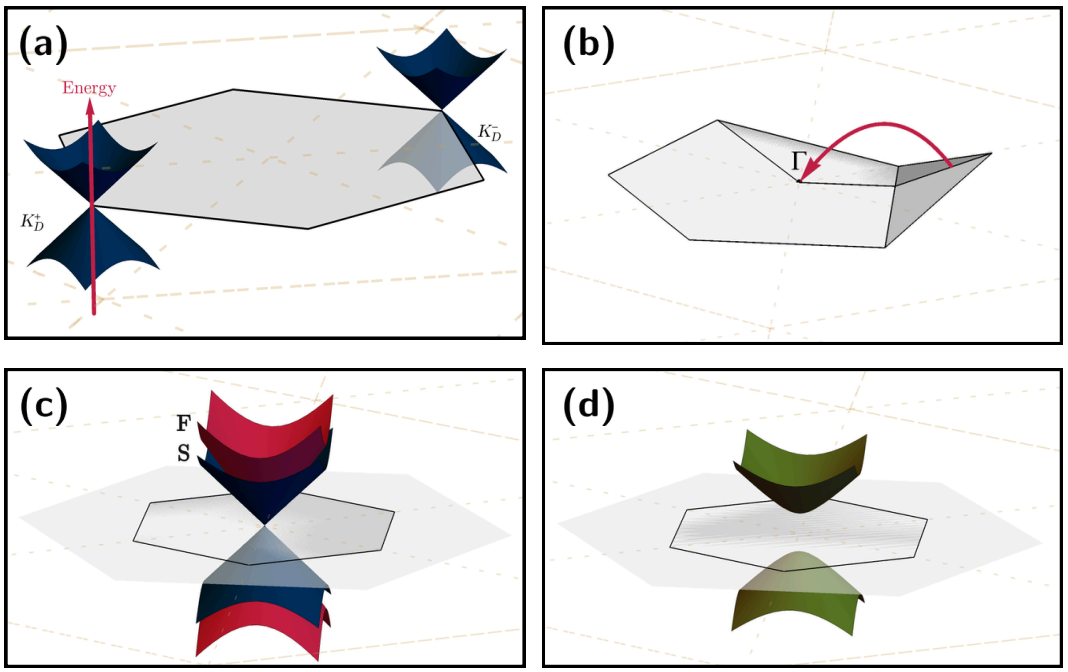

Figure 2.6: **(a)** Brillouin zone of pristine graphene in reciprocal space, shown as a gray hexagon. The two inequivalent valleys are situated in the corners of the hexagon. **(b)** Brillouin zone folding induced by the Kekulé modulation, which brings the valleys onto the Γ point of the mini Brillouin zone. **(c)** Energy dispersion relation of Kek-Y model, showing two concentric Dirac cones with different Fermi velocities. **(d)** Energy dispersion relation of Kek-O model, featuring a gapped Dirac spectrum.

$(a_{\mathbf{k}-\mathbf{G}}, a_{\mathbf{k}+\mathbf{G}}, b_{\mathbf{k}-\mathbf{G}}, b_{\mathbf{k}+\mathbf{G}})$. Projecting onto this subspace results in the reduction of the six-band Hamiltonian to an effective four-band Hamiltonian

$$H = -u_{\mathbf{k}}^{\dagger}\begin{pmatrix} \mathbf{0} & h_{\nu}(\mathbf{k}) \\ h_{\nu}^{\dagger}(\mathbf{k}) & \mathbf{0} \end{pmatrix} u_{\mathbf{k}}, \qquad h_{\nu} = \begin{pmatrix} f_{-1} & \tilde{\Delta} f_{\nu} \\ \tilde{\Delta}^{*} f_{-\nu} & f_{1} \end{pmatrix}. \tag{2.2.7}$$

We identify the K valley with $+\mathbf{G}$ and the K' valley with $-\mathbf{G}$. The $\mathbf{k}$-dependence of f_{ν} may be linearized near $\mathbf{k} = 0$, leading to

$$f_0(k_x, k_y) = -3t, \qquad f_{\pm 1}(k_x, k_y) = \hbar v_F(\mp k_x + i k_y), \tag{2.2.8}$$

where $v_F = 3at/2\hbar$ is the Fermi velocity. The corresponding 4-component Dirac equation has the form

$$\mathcal{H}\begin{pmatrix} \Psi_{K'} \\ \Psi_K \end{pmatrix} = \varepsilon \begin{pmatrix} \Psi_{K'} \\ \Psi_K \end{pmatrix}, \qquad \mathcal{H}(\mathbf{k}) = \begin{pmatrix} v_F \mathbf{p}\cdot\boldsymbol{\sigma} & \tilde{\Delta} Q_{\nu} \\ \tilde{\Delta}^{*} Q_{\nu}^{\dagger} & v_F \mathbf{p}\cdot\boldsymbol{\sigma} \end{pmatrix}, \tag{2.2.9}$$

with the spinors defined as:

$$\Psi_{K'} = \begin{pmatrix} -\psi_{B,K'} \\ \psi_{A,K'} \end{pmatrix}, \qquad \Psi_K \begin{pmatrix} \psi_{A,K} \\ \psi_{B,K} \end{pmatrix}. \tag{2.2.10}$$

Here, the Dirac operator $\mathbf{p}\cdot\boldsymbol{\sigma}$ acts on the sublattice degrees of freedom, and σ_0 is the identity matrix. Additionally, we adopt the valley-isotropic representation for Dirac spinors. The matrix Q_ν depends on the Kekulé texture and takes the form:

$$Q_\nu = \begin{pmatrix} f^*_{-\nu} & 0 \\ 0 & -f_\nu \end{pmatrix} = \begin{cases} 3t\sigma_z, & \nu = 0 \\ \nu_F(\nu p_x - p_y i)\sigma_0, & |\nu| = 1 \end{cases} . \tag{2.2.11}$$

The low-energy band structure is obtained by solving the eigenvalue problem $\mathcal{H}(\mathbf{k})\Psi(\mathbf{k}) = \varepsilon(\mathbf{k})\Psi(\mathbf{k})$. For the Kek-Y distortion ($|\nu| = 1$), the energy spectrum consists of two concentric Dirac cones with different Fermi velocities

$$\varepsilon^Y_{\eta,\xi}(\mathbf{k}) = \eta\hbar v_F(1 + \xi\Delta_0)k, \tag{2.2.12}$$

where $\eta = \pm$ labels the conduction and valence bands, and $\xi = \pm$ distinguishes the internal and external Dirac cones. The corresponding eigenstates are:

$$\psi^Y_{\eta,\xi}(\mathbf{k}) = \begin{pmatrix} \eta e^{-i\theta} \\ \xi\eta \\ \xi \\ e^{i\theta} \end{pmatrix}, \tag{2.2.13}$$

where where $k = |\mathbf{k}|$ and $\theta = \tan^{-1}(k_x/k_y)$. In contrast, for the Kek-O distortion ($\nu = 0$), the two Dirac cones are degenerate but an energy gap opens:

$$\varepsilon^O_\eta(\mathbf{k}) = \eta\sqrt{(\hbar v_F k)^2 + (3\Delta_0 t)^2} \tag{2.2.14}$$

with eigenstates of the form:

$$\psi^O_{\eta,0}(\mathbf{k}) = \frac{1}{\sqrt{2}}\frac{1}{d^O(\mathbf{k})}\begin{pmatrix} \eta d^O(\mathbf{k}) \\ \hbar v_F k e^{i\theta} \\ 3\Delta_0 t \\ 0 \end{pmatrix}, \qquad \psi^O_{\eta,1}(\mathbf{k}) = \frac{1}{\sqrt{2}}\frac{1}{d^O(\mathbf{k})}\begin{pmatrix} -\hbar v_F k e^{-i\theta} \\ -\xi d^O(\mathbf{k}) \\ 0 \\ 3\Delta_0 t \end{pmatrix}, \tag{2.2.15}$$

where the normalization factor is defined as $2d^O(\mathbf{k}) = \varepsilon^O_+(\mathbf{k}) - \varepsilon^O_-(\mathbf{k})$.

Thus, in the Kek-Y phase, the low-energy excitations consist of massless Dirac fermions with two distinct Fermi velocities, while in the Kek-O phase, the spectrum features a gapped massive Dirac spectrum [see Fig. 2.6 (c) and (d)]. Specifically, the two concentric Dirac cones emerging in Kek-Y distorted graphene are characterized by different velocities: the internal (fast) cone ($\mathbf{F}_\pm$) has a velocity $v_F(1 + \Delta_0)$, while the external (slow) cone ($\mathbf{S}_\pm$) propagates with velocity $v_F(1 - \Delta_0)$. This splitting leads to rich low-energy dynamics, which strongly contrast with the degenerate and gapped nature of the Kek-O phase.

2.3 α-$\mathcal{T}_3$ model

Beyond lattice distortions such as the Kekulé pattern, another exciting direction in the study of two-dimensional materials involves systems hosting *flat bands*, which exhibit

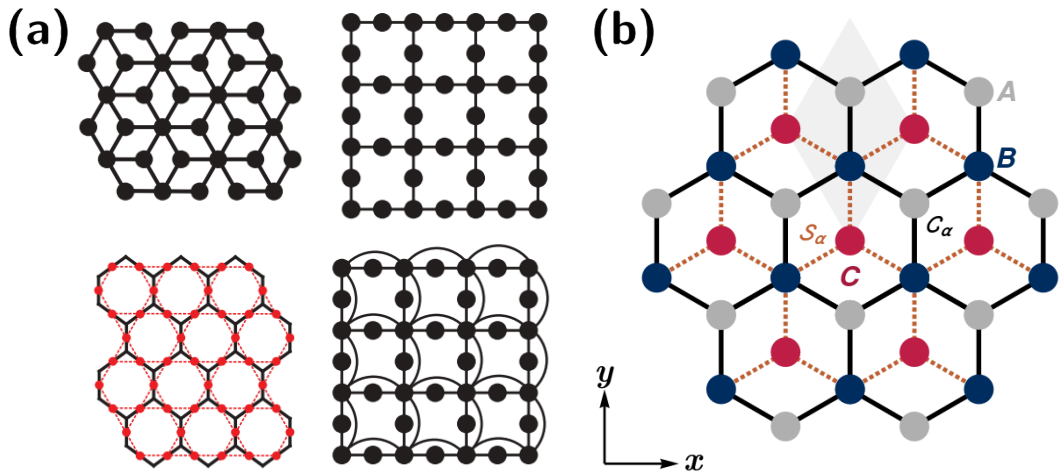

Figure 2.7: (a) Examples of flat-band lattices: the dice lattice, Lieb lattice, Kagome lattice (shown in red as the line graph of the honeycomb lattice), and Tasaki's decorated square lattice. Adapted from [75]. **(b)** Schematic of the α–$\mathcal{T}_3$ lattice. It consists of three inequivalent sites (A, B, and C), with A–B and B–C hoppings weighted by $\mathcal{C}_\alpha$ and $\mathcal{S}_\alpha$, respectively.

highly nontrivial electronic and transport properties. These systems provide an ideal platform to explore strongly correlated and topological phases of matter [36, 72–81]. In particular, the discovery of correlated insulator states and signatures of unconventional superconductivity in twisted bilayer graphene [73] has intensified the search for flat-band systems near the Fermi level [82, 83].

Flat bands can emerge in tight-binding models due to destructive quantum interference between different hopping paths. This mechanism naturally appears in line-graph lattices such as kagome and pyrochlore [75, 84–86], as well as in certain bipartite lattices including the Lieb and dice lattices [75, 87–89]. In these cases, specific sublattice connectivity leads to the formation of compact localized states, resulting in an energy band that is perfectly flat over the entire Brillouin zone.

A simple and pedagogical example of a flat-band system is the α-$\mathcal{T}_3$ model [22, 90, 91], which interpolates between graphene and the dice lattice by tuning a single hopping parameter. The model consists of a honeycomb lattice (rim atom) with an additional atom located at the center of each hexagon (a hub atom), connected only to one sublattice. For $\alpha = 0$, the model reduces to pristine graphene, whereas for $\alpha = 1$, it becomes the dice lattice, where the flat band coexists with a pair of Dirac cones. This tunability makes the α-$\mathcal{T}_3$ model an excellent platform for exploring the interplay between flat-band physics and Dirac-like dispersion.

2.3.1 Low energy Hamiltonian

The unit cell of the α-$\mathcal{T}_3$ lattice contains three inequivalent sites: A, B, and C. The A and B atoms form the conventional honeycomb lattice as in graphene, while the C atoms

(located at the centers of the hexagons) are connected only to B sites. The lattice can be viewed as three interpenetrating triangular Bravais sublattices, as shown in Fig. 2.7(b). In this configuration, the A and C sites are commonly referred to as rim atoms, since they occupy the outer vertices of each unit cell and are only connected to the central site. The B atoms, in contrast, are known as hub atoms, as they lie at the center of each hexagon and mediate the coupling between rim sites.

The tight-binding Hamiltonian can be expressed as:

$$H = -t \sum_{\mathbf{r}} \sum_{n=1}^{3} \left[\mathcal{C}_\alpha b_{\mathbf{r}}^\dagger a_{\mathbf{r}+\boldsymbol{\delta}_n} + \mathcal{S}_\alpha b_{\mathbf{r}}^\dagger c_{\mathbf{r}-\boldsymbol{\delta}_n} \right] + \text{H.c.}, \tag{2.3.1}$$

where $\mathcal{C}_\alpha = 1/\sqrt{1+\alpha^2}$ and $\mathcal{S}_\alpha = \alpha/\sqrt{1+\alpha^2}$ weight the hopping amplitudes between A–B and B–C sites, respectively. The dimensionless parameter $0 \leq \alpha \leq 1$ continuously interpolates between graphene ($\alpha = 0$) and the dice lattice ($\alpha = 1$), ensuring normalized total hopping amplitude. An alternative parametrization uses a phase angle ϕ, with $\alpha = \tan\phi$, which is convenient for Berry-phase considerations.

After performing a Fourier transform, as in previous sections, the Bloch Hamiltonian takes the form:

$$\mathcal{H}(\mathbf{k}) = \begin{pmatrix} 0 & \mathcal{C}_\alpha f(\mathbf{k}) & 0 \\ \mathcal{C}_\alpha f^*(\mathbf{k}) & 0 & \mathcal{S}_\alpha f(\mathbf{k}) \\ 0 & \mathcal{S}_\alpha f^*(\mathbf{k}) & 0 \end{pmatrix}, \tag{2.3.2}$$

where $f(\mathbf{k})$ is the structure factor, defined as in the previous section. Close to the Dirac points $\mathbf{K}_\xi$, the structure factor can be expanded as:

$$f_\xi(\mathbf{k}) = \hbar v_F (\xi k_x - i k_y), \tag{2.3.3}$$

where $\xi = \pm 1$ is the valley index and v_F is the Fermi velocity. This leads to the low-energy Dirac Hamiltonian:

$$\mathcal{H}_\xi(\mathbf{k}) = \hbar v_F \mathbf{k} \cdot \mathbf{S}_\xi, \tag{2.3.4}$$

where $\mathbf{S}_\xi = (\xi S_x, S_y)$ are pseudo-spin-1 operators defined by:

$$S_x = \begin{pmatrix} 0 & \mathcal{C}_\alpha & 0 \\ \mathcal{C}_\alpha & 0 & \mathcal{S}_\alpha \\ 0 & \mathcal{S}_\alpha & 0 \end{pmatrix}, \qquad S_y = \begin{pmatrix} 0 & -i\mathcal{C}_\alpha & 0 \\ i\mathcal{C}_\alpha & 0 & -i\mathcal{S}_\alpha \\ 0 & i\mathcal{S}_\alpha & 0 \end{pmatrix}. \tag{2.3.5}$$

Solving the eigenvalue problem, we find the energy dispersion that contains three bands:

$$\varepsilon_\eta(\mathbf{k}) = \eta \hbar v_F |\mathbf{k}|, \tag{2.3.6}$$

where η is the index band, $\eta = 1$ for the conduction band, $\eta = -1$ for the valence band, and $\eta = 0$ for the flat band. The eigenfunctions for each band are given by

$$\psi_{\eta,\xi}(\mathbf{k}) = \frac{1}{\sqrt{2}} \begin{pmatrix} \xi \mathcal{C}_\alpha e^{-i\xi\theta} \\ \eta \\ \xi \mathcal{S}_\alpha e^{i\xi\theta} \end{pmatrix}, \qquad \psi_{0,\xi}(\mathbf{k}) = \begin{pmatrix} \xi \mathcal{C}_\alpha e^{-i\xi\theta} \\ 0 \\ -\xi \mathcal{S}_\alpha e^{i\xi\theta} \end{pmatrix}, \tag{2.3.7}$$

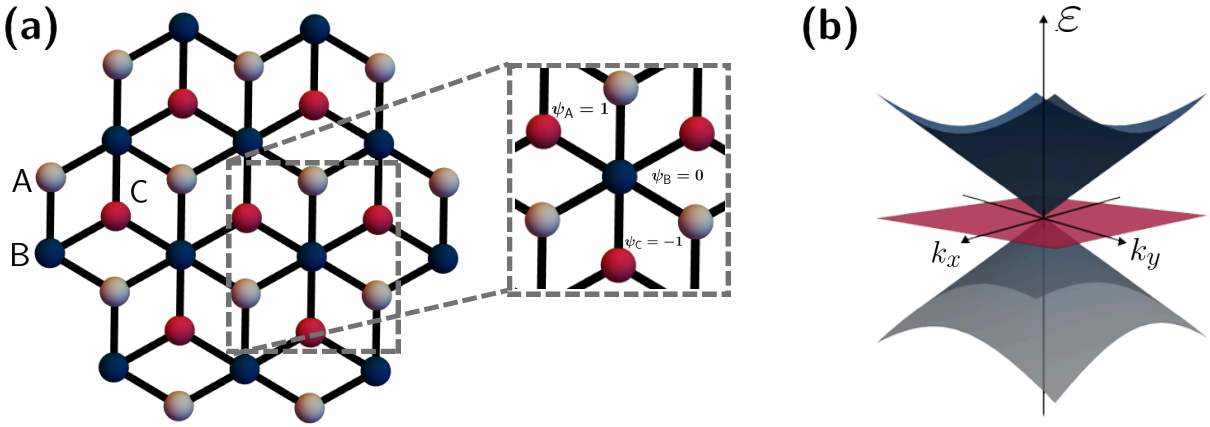

Figure 2.8: (a) Schematic illustration of destructive quantum interference in the dice (α-$\mathcal{T}_3$) lattice. Wavefunction amplitudes on the A and C sublattices are configured such that their contributions to the central hub (B) site cancel exactly, i.e., $\psi_B \propto \psi_A + \psi_C = 0$. This interference condition prevents occupation of the B sites and results in the formation of localized eigenstates associated with the flat band. **(b)** Energy dispersion of the α-$\mathcal{T}_3$ model in momentum space, showing the coexistence of Dirac cones and an exactly flat band at zero energy.

with $\theta = \arctan\left(k_y/k_x\right)$.

Importantly, the model exhibits Dirac cones at the Fermi level, accompanied by an exactly flat band at zero energy, as shown in Fig. 2.8 (b). This flat band originates from destructive quantum interference between different hopping paths, stemming from the topology and symmetry of the lattice [88].

To understand the microscopic origin of this interference, consider the dice lattice (or α-$\mathcal{T}_3$ model with $\alpha = 1$), the flat band emerges due to interference between hopping amplitudes from the peripheral A and C sublattices to the hub sites B [see Fig. 2.8 (a)]. In the eigenstates associated with the flat band, the wavefunction amplitudes on A and C are arranged such that their contributions to the B sites cancel exactly. More precisely, because each B site couples symmetrically to both A and C neighbors, the condition for zero amplitude at the hub requires:

$$\psi_B \propto \psi_A + \psi_C = 0. \tag{2.3.8}$$

This cancellation condition prevents the particle from occupying or propagating through the B sites, effectively localizing the eigenstates around them. The result is a macroscopically degenerate, non-dispersive band whose energy is independent of momentum—that is, a flat band.

Since the kinetic energy is quenched in flat bands, electron–electron interactions become dominant. As a result, flat-band systems are natural platforms for interaction-driven phenomena such as flat-band ferromagnetism, Wigner crystallization [113], and unconventional superconductivity [73]. This makes the α-$\mathcal{T}_3$ model a paradigmatic setting for exploring strongly correlated physics in two-dimensional systems.

3

Linear optical conductivity

3.1 Linear response theory

In order to understand the optical conductivity of materials, it is essential to first establish the theoretical foundation provided by linear response theory. This framework describes how a physical system initially in equilibrium responds to external perturbations, such as electric or magnetic fields, within the regime where the response is proportional to the perturbation.

Linear response theory is widely applicable, encompassing phenomena such as electric polarization **P**, magnetization **M**, and electric current **J**, each induced by their respective external fields. These responses can be generally written as space- and time-convolutions involving appropriate response functions:

$$P_i(\mathbf{r},t) = \int d\mathbf{r}' \int dt'\, \chi_{ij}(\mathbf{r},\mathbf{r}',t-t')E_j(\mathbf{r}',t') \tag{3.1.1}$$

$$M_i(\mathbf{r},t) = \int d\mathbf{r}' \int dt'\, \chi^M_{ij}(\mathbf{r},\mathbf{r}',t-t')H_j(\mathbf{r}',t') \tag{3.1.2}$$

$$J_i(\mathbf{r},t) = \int d\mathbf{r}' \int dt'\, \sigma_{ij}(\mathbf{r},\mathbf{r}',t-t')E_j(\mathbf{r}',t') \tag{3.1.3}$$

Here, χ_{ij} is the electric susceptibility tensor, χ^M_{ij} is the magnetic susceptibility tensor, and σ_{ij} is the optical conductivity tensor. The integrals over $\mathbf{r}'$ extend over the volume of the system, reflecting the non-local nature of the response in both space and time. This non-locality implies that a perturbation at point $\mathbf{r}'$ and time t' can affect the system's response at another point $\mathbf{r}$ and a later time $t > t'$. Importantly, no response occurs before the perturbation is applied, which is a manifestation of causality. As such, the response functions are said to be retarded.

When the equations above are transformed into the frequency and momentum domain, the space-time convolutions reduce to simple products:

$$P_i(\mathbf{q},\omega) = \chi_{ij}(\mathbf{q},\omega)E_j(\mathbf{q},\omega) \tag{3.1.4}$$

$$M_i(\mathbf{q},\omega) = \chi^M_{ij}(\mathbf{q},\omega)H_j(\mathbf{q},\omega) \tag{3.1.5}$$

$$J_i(\mathbf{q},\omega) = \sigma_{ij}(\mathbf{q},\omega)E_j(\mathbf{q},\omega) \tag{3.1.6}$$

This frequency-domain formulation reveals fundamental analytic properties of the response functions. One such consequence is encoded in the Kramers–Kronig relations, which connect the real and imaginary parts of a causal response function via a Hilbert transform. These relations ensure that any physically meaningful response function must satisfy causality, meaning that the system cannot respond before the perturbation is applied.

3.1.1 Kubo formalism

In quantum mechanics, linear response theory allows the calculation of changes in observable physical quantities in terms of equilibrium correlations, thereby establishing a connection between the microscopic properties of the system and its macroscopic response. When an equilibrium quantum system is perturbed, its response manifests as a modification of its energy levels and associated physical properties. This behavior is characterized through the response function, which relates the external perturbation to the system's response. Assuming the perturbation is weak, the response is proportional to the perturbation, which simplifies the analysis and allows one to derive explicit relations between the system observables and the parameters of the perturbation [114].

Let us consider a quantum system initially in thermal equilibrium at temperature T, described by a time-independent Hamiltonian H_0, with eigenvalues $\{E_n\}$ and eigenstates $\{|n\rangle\}$. The system is described by the thermal density matrix:

$$\rho_0 = \frac{1}{Z_0} e^{-H_0/k_B T} = \frac{1}{Z_0} \sum_n e^{-E_n/k_B T} |n\rangle \langle n| , \tag{3.1.7}$$

where $Z_0 = \sum_n e^{-E_n/k_B T}$ is the partition function and k_B is the Boltzmann constant. The equilibrium expectation value of an observable A is then given by:

$$\langle A \rangle = \mathrm{Tr}\rho_0 A = \frac{1}{Z_0} \sum_n e^{-E_n/k_B T} \langle n|A|n\rangle . \tag{3.1.8}$$

At time $t = t_0$, the system is perturbed by a time-dependent term $V(t)$, so that the full Hamiltonian becomes:

$$H(t) = H_0 + V(t)\Theta(t - t_0), \tag{3.1.9}$$

where $\Theta(t - t_0)$ is the Heaviside step function, acting as a switch to activate the perturbation at $t = t_0$.

The goal is to compute the expectation value of the observable A at a time $t > t_0$, taking into account the system's time evolution due to external perturbation. In the interaction picture, the states evolve as:

$$|\hat{n}(t)\rangle = e^{iH_0 t/\hbar} |n(t)\rangle , \tag{3.1.10}$$

where $|n(t)\rangle$ satisfies the time-dependent Schrödinger equation:

$$i\hbar \frac{\partial}{\partial t} |n(t)\rangle = H(t) |n(t)\rangle . \tag{3.1.11}$$

In the interaction representation, the dynamics is governed by the perturbation $\hat{V}(t)$:

$$i\hbar \frac{\partial}{\partial t} |\hat{n}(t)\rangle = \hat{V}(t) |\hat{n}(t)\rangle , \tag{3.1.12}$$

where $\hat{V}(t) = e^{iH_0 t/\hbar} V(t) e^{-iH_0 t/\hbar}$ is the perturbation in the interaction picture. Similarly, the evolution of the system can be described using the time-evolution operator as $|\hat{n}(t)\rangle = \hat{U}(t) |n\rangle$, which, under the assumption of weak perturbations, can be approximated to first order as:

$$\hat{U}(t) \approx 1 - \frac{i}{\hbar} \int_{t_0}^{t} \hat{V}(t') dt' . \tag{3.1.13}$$

Thus, the time evolution of the expectation value $\langle A(t) \rangle$ for $t > t_0$ is:

$$\langle A(t) \rangle = \frac{1}{Z_0} \sum_n e^{-E_n/k_B T} \langle n| \hat{U}^\dagger(t) \hat{A}(t) \hat{U}(t) |n\rangle . \tag{3.1.14}$$

Keeping only terms up to first order in $\hat{V}(t)$, we obtain:

$$\langle n| \hat{U}^\dagger(t) \hat{A}(t) \hat{U}(t) |n\rangle \approx \langle n| \hat{A}(t) |n\rangle - \frac{i}{\hbar} \int_{t_0}^{t} \langle n| [\hat{A}(t), \hat{V}(t')] |n\rangle \, dt' , \tag{3.1.15}$$

where $\hat{A}(t) = e^{iH_0 t/\hbar} A(t) e^{-iH_0 t/\hbar}$ is the observable in the interaction picture. Therefore, Eq. (3.1.14) becomes:

$$\langle A(t) \rangle = \left\langle \hat{A}(t) \right\rangle_0 - \frac{i}{\hbar} \int_{t_0}^{t} \left\langle [\hat{A}(t), \hat{V}(t')] \right\rangle_0 dt' , \tag{3.1.16}$$

where $\langle \cdot \rangle_0$ denotes the expectation value with respect to the equilibrium Hamiltonian H_0.

As described above is the Kubo formalism [115], which establishes a fundamental connection between the system's response and its equilibrium correlations. The *Kubo formula* [Eq. (3.1.16)] shows that the response of an observable A to an external perturbation $V(t)$ is governed by the temporal correlations of the system in equilibrium. These correlations describe how internal fluctuations propagate and couple to the external perturbation, providing a detailed description of the system's dynamical properties.

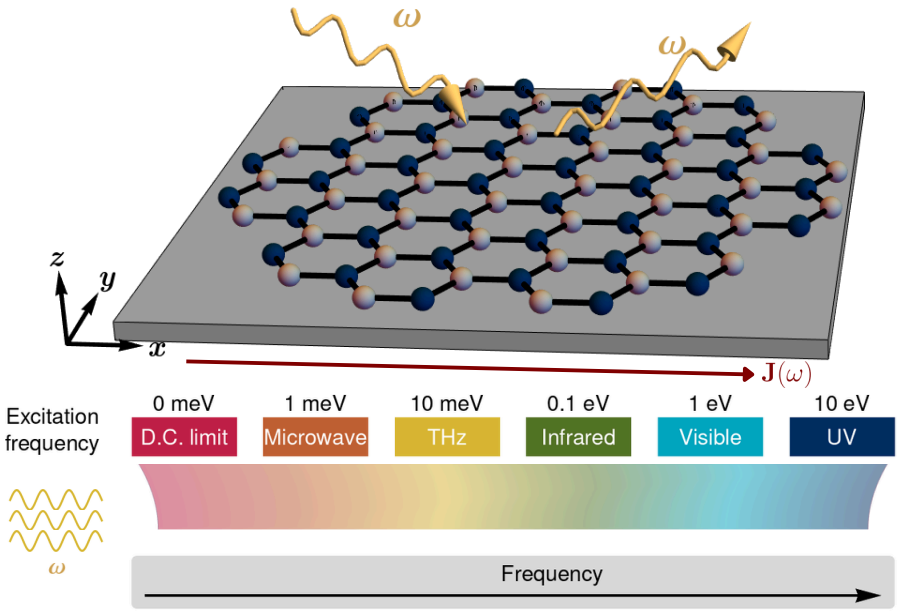

Figure 3.1: Schematic representation of the optical excitation process in a two-dimensional material. An incident electromagnetic wave of frequency ω interacts with the sample, inducing an optical current $\mathbf{J}(\omega)$ associated with electronic transitions of energy $\hbar\omega$. This current re-emits radiation with modified amplitude and phase, giving rise to the reflected signal that encodes the material's optical response. Below, the electromagnetic spectrum is shown with the corresponding frequency and energy ranges.

3.2 Response function of optical conductivity

In general, two-dimensional (2D) materials exhibit strong light-matter interaction [116], which can be characterized by their optical conductivity (see Fig 3.1). Optical conductivity characterizes the response of a system of charged particles to an external electromagnetic wave oscillating at a finite frequency. Experimentally, several techniques have been employed to probe this quantity, including infrared (IR) spectroscopy [11, 12, 117], scattering-type scanning near-field optical microscopy (s-SNOM) [118], electron energy-loss spectroscopy (EELS) [119], and more recent developments such as four-dimensional scanning transmission electron microscopy (4D-STEM) spectroscopy [120] and near-field scanning techniques [121].

On the theoretical approach, linear response theory provides a robust framework to compute the optical conductivity. In the following, we present the derivation of the corresponding response function using the Kubo formalism.

We consider a homogeneous electron system subjected to a plane electromagnetic wave described by a magnetic vector potential and an electric field:

$$\mathbf{A}(\mathbf{r},t) = \mathbf{A}_0 e^{i(\mathbf{q}\cdot\mathbf{r}-\omega t)}, \qquad \mathbf{E}(\mathbf{r},t) = \mathbf{E}_0 e^{i(\mathbf{q}\cdot\mathbf{r}-\omega t)}, \tag{3.2.1}$$

respectively, where ω is the frequency and $\mathbf{q}$ is the wavevector of the incoming radiation, with $|\mathbf{A}_0|$ and $|\mathbf{E}_0|$ denoting the amplitudes of the vector potential and electric field, respectively. In linear response theory, the external electromagnetic wave induces an electric current in the system proportional to the applied field:

$$\langle J_i^e(\omega)\rangle = \sum_{j=\{x,y\}} \sigma_{ij}(\omega) E_j(\omega), \tag{3.2.2}$$

where $\sigma_{ij}(\omega)$ is the optical conductivity tensor, which characterizes the current response along the $\hat{e}_i$ direction to an electric field along $\hat{e}_j$. Here, i and j denote Cartesian coordinates. The operator $J_i^e(\omega)$ represents the quantum current density, and its expectation value $\langle J_i^e(\omega)\rangle$ is the quantity measured in experiments [122]. The Hamiltonian for a non-relativistic charged particle in the presence of an electromagnetic field is given by:

$$H(t) = \frac{1}{2m} |\mathbf{p} - e\mathbf{A}(\mathbf{r}, t)|^2, \tag{3.2.3}$$

where $\mathbf{p} = -i\hbar\nabla$ is the momentum operator, m is the particle mass, and e its electric charge. Neglecting second-order terms in the vector potential (justified in the weak field regime), the Hamiltonian can be separated into the unperturbed (equilibrium) part and the external perturbation:

$$H(t) = \frac{\mathbf{p}\cdot\mathbf{p}}{2m} - \frac{e}{m}\mathbf{p}\cdot\mathbf{A}(\mathbf{r}, t), \tag{3.2.4}$$

where the perturbation is defined as:

$$V(t) = -\frac{e}{m}\mathbf{p}\cdot\mathbf{A}(\mathbf{r}, t). \tag{3.2.5}$$

The total current density operator derived from this Hamiltonian consists of two contributions:

$$\mathbf{J}^e(\mathbf{r}, t) = \mathbf{J}^P(\mathbf{r}, t) + \mathbf{J}^D(\mathbf{r}, t), \tag{3.2.6}$$

where $\mathbf{J}^P$ is the paramagnetic current and $\mathbf{J}^D$ is the diamagnetic current:

$$\text{Paramagnetic:} \qquad \mathbf{J}^P(\mathbf{r}, t) = \frac{\hbar e}{m}\mathbb{I}\mathrm{m}\{\psi^*(\mathbf{r}, t)\nabla\psi(\mathbf{r}, t)\}, \tag{3.2.7}$$

$$\text{Diamagnetic:} \qquad \mathbf{J}^D(\mathbf{r}, t) = -\frac{e^2}{m}\mathbf{A}(\mathbf{r}, t)\rho. \tag{3.2.8}$$

Here, $\psi(\mathbf{r}, t)$ is the particle's wavefunction and $\rho = |\psi(\mathbf{r}, t)|^2$ is the probability density. The paramagnetic current corresponds to the conventional quantum mechanical probability current, while the diamagnetic part arises due to the interaction with the external field.

Taking expectation values, the total electric current becomes:

$$\langle \mathbf{J}^e(t)\rangle = \langle \mathbf{J}^P(t)\rangle + \langle \mathbf{J}^D(t)\rangle. \tag{3.2.9}$$

To study the time evolution of this quantity and derive an expression for the optical conductivity, we employ the Kubo formula [Eq. (3.1.16)]. Within linear response theory, the diamagnetic term is already first-order in the perturbation, so its expectation value can be evaluated in equilibrium:

$$\langle J_i^D(t)\rangle = -\frac{e^2}{m}A_i(\mathbf{r},t)\langle\rho\rangle_0. \tag{3.2.10}$$

On the other hand, the paramagnetic contribution is evaluated using the Kubo formula:

$$\langle J_i^P(t)\rangle = -\frac{i}{\hbar}\int_{t_0}^{t} dt'\ \left\langle[\hat{J}_i^P(t),\hat{V}(t')]\right\rangle_0, \tag{3.2.11}$$

where we have assumed that the equilibrium current vanishes, i.e., $\langle J_i^P(t)\rangle_0 = 0$. The perturbation $V(t)$ can be expressed in terms of the current operator by noting that:

$$\mathbf{J}^P = e\frac{\partial H_0}{\partial \mathbf{p}} = e\frac{\mathbf{p}}{m}. \tag{3.2.12}$$

In the long-wavelength limit ($\mathbf{q}\to 0$), the electromagnetic fields become time-dependent only: $\mathbf{A}(t) = \mathbf{A}_0 e^{-i\omega t}$ and $\mathbf{E}(t) = \mathbf{E}_0 e^{-i\omega t}$. From Maxwell's equations, we have the relation $\mathbf{E}(t) = -\partial_t \mathbf{A}(t) = i\omega\mathbf{A}(t)$, so the perturbation becomes:

$$V(t) = \frac{i}{\omega}\mathbf{J}^P\cdot\mathbf{E}(t). \tag{3.2.13}$$

Substituting this expression into the Kubo formula and taking $t_0\to-\infty$, neglecting transient effects, we obtain:

$$\langle J_i^P(t)\rangle = \frac{1}{\hbar\omega}\sum_j\int_{-\infty}^{t} dt'\ \left\langle[\hat{J}_i^P(t),\hat{J}_j^P(t')]\right\rangle_0 E_j(t'). \tag{3.2.14}$$

To obtain an expression for the optical conductivity in the frequency domain, we take the Fourier transform of the current expectation value:

$$\langle J_i^e(\omega)\rangle = \int_{-\infty}^{\infty} dt\ e^{i\omega t}\langle J_i^P(t)\rangle + \int_{-\infty}^{\infty} dt\ e^{i\omega t}\langle J_i^D(t)\rangle. \tag{3.2.15}$$

The first integral corresponds to the Fourier transform of the paramagnetic contribution:

$$\langle J_i^P(\omega)\rangle = \frac{1}{\hbar\omega}\sum_j\int_0^{\infty} d\tau\ e^{i\omega\tau}\langle[\hat{J}_i(\tau),\hat{J}_j^P(0)]\rangle_0 E_j(\omega), \tag{3.2.16}$$

where we changed variables to $\tau = t - t'$.

The second integral corresponds to the Fourier transform of the diamagnetic contribution. Using the relation $\mathbf{E}(t) = i\omega\mathbf{A}(t)$, the diamagnetic term in the frequency domain becomes:

$$\langle J_i^D(\omega)\rangle = -\frac{ne^2}{m}\frac{E_i(\omega)}{i\omega}. \tag{3.2.17}$$

where $n = \langle \rho \rangle_0$ is the density of particles. Thus, the total current becomes:

$$\langle J_i^e(\omega) \rangle = \sum_j \left[\frac{1}{\hbar\omega} \int_0^\infty d\tau \, e^{i\omega\tau} \left\langle [\hat{J}_i^P(\tau), \hat{J}_j^P(0)] \right\rangle_0 + \frac{ie^2 n}{m\omega} \delta_{ij} \right] E_j(\omega). \tag{3.2.18}$$

From this expression, we identify the optical conductivity as a function of the frequency of the external electric field:

$$\sigma_{ij}(\omega) = \frac{i}{\tilde{\omega}} \left[\Pi_{ij}(\omega) + \frac{e^2 n}{m} \delta_{ij} \right], \tag{3.2.19}$$

where the current–current correlation function is defined as

$$\Pi_{ij}(\omega) = \frac{1}{i\hbar} \int_0^\infty d\tau \, e^{i\tilde{\omega}\tau} \left\langle [\hat{J}_i^P(\tau), \hat{J}_j^P(0)] \right\rangle_0, \tag{3.2.20}$$

Here, we have introduced an artificial relaxation mechanism by replacing $\omega \to \tilde{\omega} = \omega + i\eta$, where $\eta > 0$ accounts for dissipation effects [123]. This parameter ensures convergence of the integral and should be taken to zero at the end of the calculation, $\eta \to 0^+$.

For Dirac systems, it is possible to define an appropriate diamagnetic contribution such that the Kubo formula for the conductivity takes a simplified form [124]:

$$\sigma_{ij}(\omega) = \frac{i}{\tilde{\omega}} [\Pi_{ij}(\omega) - \Pi_{ij}(0)], \tag{3.2.21}$$

where $\Pi_{ij}(0) = \lim_{\tilde{\omega}\to 0} \Pi_{ij}(\omega)$. This expression is particularly convenient for evaluating the optical response of Dirac systems to external electromagnetic fields.

3.2.1 Spectral form of the optical conductivity tensor

The Kubo formula for the optical conductivity can be rewritten in its spectral representation by explicitly expanding the current-current correlation function. For a two-dimensional system in equilibrium, the retarded correlation function takes the form

$$\Pi_{ij}(\omega) = \frac{1}{i\hbar} \int_0^\infty dt \, e^{i\tilde{\omega}t} \int \frac{d^2k}{(2\pi)^2} \sum_\lambda f(\varepsilon_\lambda) \langle \psi_\lambda(\mathbf{k}) | [\hat{J}_i^P(\tau), \hat{J}_j^P(0)] | \psi_\lambda(\mathbf{k}) \rangle, \tag{3.2.22}$$

where $f(\varepsilon_\lambda) = \{\exp[(\varepsilon_\lambda - \varepsilon_F)/k_B T] + 1\}^{-1}$ is the Fermi-Dirac distribution function for fermions, and $\varepsilon_\lambda(\mathbf{k})$, $|\psi_\lambda(\mathbf{k})\rangle$ are the eigenvalues and eigenstates of the equilibrium Hamiltonian.

After performing the time integral, the correlation function takes the spectral form:

$$\Pi_{ij}(\omega) = e^2 \int \frac{d^2k}{(2\pi)^2} \sum_{\lambda,\lambda'} [f(\varepsilon_\lambda) - f(\varepsilon'_\lambda)] \frac{\langle \psi_\lambda(\mathbf{k}) | v_i | \psi_{\lambda'}(\mathbf{k}) \rangle \langle \psi_{\lambda'}(\mathbf{k}) | v_j | \psi_\lambda(\mathbf{k}) \rangle}{\varepsilon_\lambda - \varepsilon_{\lambda'} + \hbar\tilde{\omega}}, \tag{3.2.23}$$

where the velocity operator is defined as $v_i = (1/e)\hat{J}_i^P$. Hence, using Eq. (3.2.21), we recover the following expression for the optical conductivity:

$$\sigma_{ij}(\omega) = -ie^2\hbar \int \frac{d^2k}{(2\pi)^2} \sum_{\lambda,\lambda'} \left(\frac{f(\varepsilon_\lambda) - f(\varepsilon'_\lambda)}{\varepsilon_\lambda - \varepsilon_{\lambda'}} \right) \frac{\langle \psi_\lambda(\mathbf{k}) | v_i | \psi_{\lambda'}(\mathbf{k}) \rangle \langle \psi_{\lambda'}(\mathbf{k}) | v_j | \psi_\lambda(\mathbf{k}) \rangle}{\varepsilon_\lambda - \varepsilon_{\lambda'} + \hbar\tilde{\omega}}. \tag{3.2.24}$$

To better visualize the different contributions to the optical conductivity, it is convenient to split the summation over λ, λ' into two parts: intraband ($\lambda = \lambda'$) and interband ($\lambda \neq \lambda'$) contributions:

$$\begin{aligned}
\sigma_{ij}(\omega) = &- ie^2\hbar \int \frac{d^2k}{(2\pi)^2} \sum_{\lambda} \lim_{\lambda' \to \lambda} \left(\frac{f(\varepsilon_\lambda) - f(\varepsilon_{\lambda'})}{\varepsilon_\lambda - \varepsilon_{\lambda'}} \right) \frac{\langle \psi_\lambda(\mathbf{k}) | v_i | \psi_{\lambda'}(\mathbf{k}) \rangle \langle \psi_{\lambda'}(\mathbf{k}) | v_j | \psi_\lambda(\mathbf{k}) \rangle}{\varepsilon_\lambda - \varepsilon_{\lambda'} + \hbar\tilde{\omega}} \\
&- ie^2\hbar \int \frac{d^2k}{(2\pi)^2} \sum_{\substack{\lambda',\lambda \\ \lambda' \neq \lambda}} \left(\frac{f(\varepsilon_\lambda) - f(\varepsilon_{\lambda'})}{\varepsilon_\lambda - \varepsilon_{\lambda'}} \right) \frac{\langle \psi_\lambda(\mathbf{k}) | v_i | \psi_{\lambda'}(\mathbf{k}) \rangle \langle \psi_{\lambda'}(\mathbf{k}) | v_j | \psi_\lambda(\mathbf{k}) \rangle}{\varepsilon_\lambda - \varepsilon_{\lambda'} + \hbar\tilde{\omega}}, \\
= &\, \sigma_{ij}^{\text{intra}}(\omega) + \sigma_{ij}^{\text{inter}}(\omega),
\end{aligned} \tag{3.2.25}$$

where $\sigma_{ij}^{\text{intra}}(\omega)$ denotes the intraband contribution, which can be written as

$$\sigma_{ij}^{\text{intra}}(\omega) = i\frac{e^2}{\tilde{\omega}} \sum_{\lambda} \int \frac{d^2k}{(2\pi)^2} \left(-\frac{\partial f(\varepsilon_\lambda)}{\partial \varepsilon_\lambda} \right) \langle \psi_\lambda(\mathbf{k}) | v_i | \psi_\lambda(\mathbf{k}) \rangle \langle \psi_\lambda(\mathbf{k}) | v_j | \psi_\lambda(\mathbf{k}) \rangle . \tag{3.2.26}$$

Using the Kramers-Kroning relations, we obtain that:

$$\lim_{\eta^+ \to 0} \frac{1}{x \pm i\eta^+} = \mathcal{P}\left(\frac{1}{x}\right) \mp i\pi\delta(x), \tag{3.2.27}$$

the intraband conductivity can be decomposed into a delta peak at zero frequency and a purely imaginary dispersive part:

$$\sigma_{ij}^{\text{intra}}(\omega) = D_{ij}\delta(\omega) + i\mathbb{I}\text{m}\{\sigma_{ij}^{\text{intra}}(\omega)\}, \tag{3.2.28}$$

where $D_{ij} = \pi \lim_{\omega \to 0}[\omega\, \mathbb{I}\text{m}\{\sigma_{ij}^{\text{intra}}\}]$ is the Drude weight. This quantity characterizes the charge stiffness, i.e., the ability of the system to carry a persistent current. Importantly, D_{ij} is finite in metals but vanishes in insulators. It remains well-defined even in the presence of disorder or interactions [125].

On the other hand, the interband contribution to the conductivity reads:

$$\sigma_{ij}^{\text{inter}}(\omega) = -ie^2\hbar \int \frac{d^2k}{(2\pi)^2} \sum_{\substack{\lambda',\lambda \\ \lambda' \neq \lambda}} \left(\frac{f(\varepsilon_\lambda) - f(\varepsilon_{\lambda'})}{\varepsilon_\lambda - \varepsilon_{\lambda'}} \right) \frac{\langle \psi_\lambda(\mathbf{k}) | v_i | \psi_{\lambda'}(\mathbf{k}) \rangle \langle \psi_{\lambda'}(\mathbf{k}) | v_j | \psi_\lambda(\mathbf{k}) \rangle}{\varepsilon_\lambda - \varepsilon_{\lambda'} + \hbar\tilde{\omega}}. \tag{3.2.29}$$

This term describes vertical transitions between occupied and unoccupied states across different bands and is responsible for photon absorption at finite frequencies.

Finally, we note that the optical conductivity is, in general, a complex tensor quantity with both real and imaginary parts, expressed as

$$\sigma_{ij}(\omega) = \mathbb{R}\mathrm{e}\{\sigma_{ij}(\omega)\} + i\mathbb{I}\mathrm{m}\{\sigma_{ij}(\omega)\} \tag{3.2.30}$$

These components are not independent; they are fundamentally connected through the Kramers–Kronig relations, which ensure causality in the system's response [126–128]:

$$\mathbb{R}\mathrm{e}\{\sigma_{ij}(\omega)\} = \frac{1}{\pi}\mathcal{P}\int_{-\infty}^{\infty}\frac{\mathbb{I}\mathrm{m}\{\sigma_{ij}(\omega')\}}{\omega'-\omega}d\omega', \tag{3.2.31}$$

$$\mathbb{I}\mathrm{m}\{\sigma_{ij}(\omega)\} = -\frac{1}{\pi}\mathcal{P}\int_{-\infty}^{\infty}\frac{\mathbb{R}\mathrm{e}\{\sigma_{ij}(\omega')\}}{\omega'-\omega}d\omega'. \tag{3.2.32}$$

Physically, the real part of the optical conductivity, $\mathbb{R}\mathrm{e}\{\sigma_{ij}(\omega)\}$, quantifies the dissipative response of the material — that is, the net absorption of energy from the incident electromagnetic field due to processes such as interband or intraband transitions [129]. In contrast, the imaginary part, $\mathbb{I}\mathrm{m}\{\sigma_{ij}(\omega)\}$, characterizes the non-dissipative (reactive) response, associated with energy temporarily stored in the material's polarization or current oscillations. This component contributes to the phase shift between the applied field and the induced current but does not correspond to net energy loss [129, 130].

3.3 Optical conductivity of graphene

To illustrate the concepts discussed throughout this chapter, we now present a detailed calculation of the optical conductivity of pristine graphene. Starting from its low-energy Hamiltonian and eigenstates near the Dirac points, one finds that the conductivity tensor reduces to a scalar form due to isotropy. The components take the following expressions:

$$\mathbb{R}\mathrm{e}\{\sigma^{\xi}(\omega)\} = D\delta(\omega) + \mathbb{R}\mathrm{e}\{\sigma^{\xi,\mathrm{inter}}(\omega)\} \tag{3.3.1}$$

$$\mathbb{I}\mathrm{m}\{\sigma^{\xi}(\omega)\} = \mathbb{I}\mathrm{m}\{\sigma^{\xi,\mathrm{intra}}(\omega)\} + \mathbb{I}\mathrm{m}\{\sigma^{\xi,\mathrm{inter}}(\omega)\} \tag{3.3.2}$$

$$\sigma^{\xi}_{xy}(\omega) = -\sigma^{\xi}_{xy}(\omega) = 0 \tag{3.3.3}$$

where the subscripts intra and inter label the intraband and interband contributions, respectively. The term $D = \pi\lim_{\omega\to 0}[\omega\mathbb{I}\mathrm{m}\{\sigma^{\xi}(\omega)\}] = \pi\lim_{\omega\to 0}[\omega\mathbb{I}\mathrm{m}\{\sigma^{\xi,\mathrm{intra}}(\omega)\}]$ is known as the Drude weight, which characterizes the strength of the intraband (free-carrier) response.

It is important to note that the full optical conductivity tensor $\sigma_{ij}(\omega)$ is obtained by summing over contributions from both valleys, i.e., $\sigma_{ij}(\omega) = \sum_{\xi=\pm}\sigma^{\xi}_{ij}(\omega)$. In general, for an isotropic system, the structure of the conductivity remains the same as in the expressions above, except for the absence of the valley index.

3.3.1 Interband contribution

Graphene is a two-band system consisting of a conduction and a valence band. We denote the band indices by $\lambda, \lambda' = \pm$, where $+(-)$ refers to the conduction (valence) band. We define the following matrix elements:

$$v_{ij}^{\xi}(\mathbf{k}) = \left\langle \psi_{+}^{\xi}(\mathbf{k}) \right| v_i \left| \psi_{-}^{\xi}(\mathbf{k}) \right\rangle \left\langle \psi_{-}^{\xi}(\mathbf{k}) \right| v_j \left| \psi_{+}^{\xi}(\mathbf{k}) \right\rangle, \tag{3.3.4}$$

such that the interband optical conductivity in Eq. (3.2.29), can be written as

$$\sigma^{\xi,\text{inter}}(\omega) = -\frac{ie^2\hbar}{(2\pi)^2}\left[\int d^2k \left(\frac{f(\varepsilon_+)-f(\varepsilon_-)}{2d(\mathbf{k})}\right)\left(\frac{v_{ij}^{\xi}(\mathbf{k})}{2d(\mathbf{k})+\hbar\tilde{\omega}} - \frac{v_{ji}^{\xi}(\mathbf{k})}{2d(\mathbf{k})-\hbar\tilde{\omega}}\right)\right], \tag{3.3.5}$$

where we have defined $2d(\mathbf{k}) = \varepsilon_+(\mathbf{k}) - \varepsilon_-(\mathbf{k})$. At zero temperature, the Fermi-Dirac distribution reduces to a Heaviside step function, and the interband conductivity becomes

$$\sigma^{\xi,\text{inter}}(\omega) = \frac{ie^2\hbar}{(2\pi)^2}\left[\int' d^2k \, \frac{1}{2d(\mathbf{k})}\left(\frac{v_{ij}^{\xi}(\mathbf{k})}{2d(\mathbf{k})+\hbar\tilde{\omega}} - \frac{v_{ji}^{\xi}(\mathbf{k})}{2d(\mathbf{k})-\hbar\tilde{\omega}}\right)\right], \tag{3.3.6}$$

where the prime on the integral denotes the region in $\mathbf{k}$-space for which $\varepsilon_-(\mathbf{k}) < \varepsilon_F < \varepsilon_+(\mathbf{k})$. Now, we write the matrix elements as $v_{ij}^{\xi}(\mathbf{k}) = \mathbb{R}\text{e}\{v_{ij}^{\xi}(\mathbf{k})\} + i\,\mathbb{I}\text{m}\{v_{ij}^{\xi}(\mathbf{k})\}$ and use the Kramers–Kronig relations [Eq. (3.2.27)] to express the conductivity as

$$\begin{aligned}\sigma^{\xi,\text{inter}}(\omega) = \frac{e^2\hbar}{(2\pi)^2}\int d^2k \, \frac{1}{2d(\mathbf{k})}\Bigg\{&\mathbb{I}\text{m}\{v_{ij}^{\xi}\}\mathcal{P}\left(\frac{-4d(\mathbf{k})}{[2d(\mathbf{k})]^2-(\hbar\omega)^2}\right) + \mathbb{R}\text{e}\{v_{ij}^{\xi}\}\pi\delta(2d(\mathbf{k})-\hbar\omega) + \\ &i\left[\mathbb{R}\text{e}\{v_{ij}^{\xi}\}\mathcal{P}\left(\frac{-2\hbar\omega}{[2d(\mathbf{k})]^2-(\hbar\omega)^2}\right) + \mathbb{I}\text{m}\{v_{ij}^{\xi}\}\pi\delta(2d(\mathbf{k})-\hbar\omega)\right]\Bigg\} \\ = \mathbb{R}\text{e}\{\sigma^{\xi,\text{inter}}(\omega)\} &+ i\,\mathbb{I}\text{m}\{\sigma^{\xi,\text{inter}}(\omega)\}.\end{aligned} \tag{3.3.7}$$

We have neglected terms proportional to $\delta(2d(\mathbf{k})+\hbar\omega)$, as they describe emission processes. Since we assume the system is initially in its ground state, only absorption processes—described by $\delta(2d(\mathbf{k})-\hbar\omega)$—are considered.

Finally, we obtain the real and imaginary parts of the interband conductivity:

$$\begin{aligned}\mathbb{R}\text{e}\{\sigma^{\xi,\text{inter}}(\omega)\} = -g_s\sigma_0\frac{\hbar^2}{4\pi}\int d^2k\frac{1}{2d(\mathbf{k})}\Bigg[&\mathbb{I}\text{m}\{v_{ij}^{\xi}(\mathbf{k})\}\mathcal{P}\left(\frac{4d(\mathbf{k})}{[2d(\mathbf{k})]^2-[\hbar\omega]^2}\right) \\ &- \pi\mathbb{R}\text{e}\{v_{ij}^{\xi}(\mathbf{k})\}\delta(2d(\mathbf{k})-\hbar\omega)\Bigg],\end{aligned} \tag{3.3.8}$$

$$\begin{aligned}\mathbb{I}\text{m}\{\sigma^{\xi,\text{inter}}(\omega)\} = -g_s\sigma_0\frac{\hbar^2}{4\pi}\int d^2k\frac{1}{2d(\mathbf{k})}\Bigg[&\mathbb{R}\text{e}\{v_{ij}^{\xi}(\mathbf{k})\}\mathcal{P}\left(\frac{2\hbar\omega}{[2d(\mathbf{k})]^2-[\hbar\omega]^2}\right) \\ &+ \pi\mathbb{I}\text{m}\{v_{ij}^{\xi}(\mathbf{k})\}\delta(2d(\mathbf{k})-\hbar\omega)\Bigg]\end{aligned} \tag{3.3.9}$$

where $\sigma_0 = 2e^2/h$ is the universal conductivity quantum and $g_s = 2$ accounts for spin degeneracy.

Real part of interband conductivity

Considering the real part of the interband contribution, we have:

$$\mathbb{R}\mathrm{e}\{\sigma_{ij}^{\xi,\mathrm{inter}}(\omega)\} = g_s\sigma_0\frac{\hbar^2}{4}\int' d^2k\,\frac{\mathbb{R}\mathrm{e}\{v_{ij}^{\xi}\}(\mathbf{k})}{2d(\mathbf{k})}\delta(2d(\mathbf{k})-\hbar\omega), \tag{3.3.10}$$

where we have taken $\mathbb{I}\mathrm{m}\{v_{ij}^{\xi}\}=0$ since v_{ij}^{ξ} is Hermitian and given by

$$v_{ij}^{\xi} = \frac{v_F^2}{2}\{\delta_i^j[1+(\delta_i^y-\delta_i^x)\cos(2\theta)]-\xi[1-\delta_i^j]\sin(2\theta)\}. \tag{3.3.11}$$

Note that v_{ij}^{ξ} does not depend on the band, and is valid for interband and intraband transitions. Due to the azimuthal symmetry of the graphene dispersion relation, $\varepsilon_\eta = \eta\hbar v_F k$ with $\eta=\pm$ the band index, we can switch to polar coordinates. The delta function then becomes

$$\delta(2d(k)-\hbar\omega) = \Theta(\hbar\omega-\hbar\omega_F)\frac{\delta(k-k_r)}{|\partial_k[2d(k_r)]|}, \tag{3.3.12}$$

where k_r is the solution of $2d(k)=\hbar\omega$, and defines the radii of the resonance curves. The step function arises from the Pauli blocking condition $k>k_F$, where k_F is the radii of the Fermi contour, $\varepsilon_\eta(k)=\varepsilon_F$, and thus $\hbar\omega > 2d(k_F)\equiv\hbar\omega_F$ defines the critical frequency. Therefore, the conductivity becomes

$$\mathbb{R}\mathrm{e}\{\sigma_{ij}^{\xi,\mathrm{inter}}(\omega)\} = g_s\sigma_0\frac{\hbar^2}{4}\int_0^{2\pi}d\theta\int_{k_F}^{\infty}kdk\,\Theta(\hbar\omega-\hbar\omega_F)\frac{\mathbb{R}\mathrm{e}\{v_{ij}^{\xi}\}}{2\hbar v_F k}\frac{\delta(k-k_r)}{2\hbar v_F}. \tag{3.3.13}$$

Only the components $\mathbb{R}\mathrm{e}\{v_{ij}^{\xi}\}$ depend on the angular variable. After solving the angular part, we note that the conductivity tensor reduces to a scalar. Therefore, the real part of the interband conductivity is given by

$$\mathbb{R}\mathrm{e}\{\sigma^{\xi,\mathrm{inter}}(\omega)\} = g_s\sigma_0\frac{\pi}{16}\Theta(\hbar\omega-2|\varepsilon_F|), \tag{3.3.14}$$

which shows that it depends only on the Fermi energy.

Imaginary part of interband conductivity

On the other hand, the imaginary part of the interband contribution is given by

$$\mathbb{I}\mathrm{m}\{\sigma^{\xi,\mathrm{inter}}(\omega)\} = -g_s\sigma_0\frac{\hbar^2}{4\pi}\int d^2k\frac{\mathbb{R}\mathrm{e}\{v_{ij}^{\xi}(\mathbf{k})\}}{2d(\mathbf{k})}\mathcal{P}\left(\frac{2\hbar\omega}{[2d(\mathbf{k})]^2-[\hbar\omega]^2}\right). \tag{3.3.15}$$

Following a similar procedure to the real part, we change to polar coordinates and perform the angular integration:

$$\mathbb{I}\mathrm{m}\{\sigma^{\xi,\mathrm{inter}}(\omega)\} = -g_s\sigma_0\frac{v_F\hbar}{8\pi}\mathcal{P}\int_{k_F}^{\infty}\frac{2\hbar\omega}{[2d(\mathbf{k})]^2-[\hbar\omega]^2}\,dk. \tag{3.3.16}$$

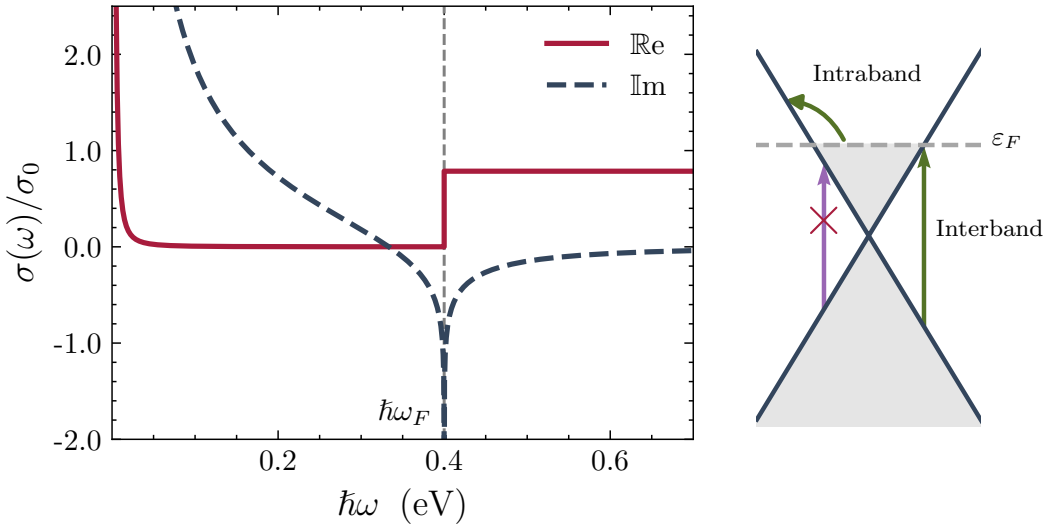

Figure 3.2: Real and imaginary parts of the optical conductivity of graphene as a function of photon energy $\hbar\omega$, at zero temperature and finite Fermi level. On the side, we include a schematic diagram illustrating the possible optical transitions: intraband (within the same band), interband (across bands), and the forbidden transitions due to Pauli blocking. We consider $\varepsilon_F = 0.2$ eV.

Thus, the imaginary part of the interband conductivity becomes

$$\mathbb{I}\mathrm{m}\{\sigma^{\xi,\mathrm{inter}}(\omega)\} = g_s\sigma_0\frac{1}{16}\ln\left|\frac{\hbar\omega - 2|\varepsilon_F|}{\hbar\omega + 2|\varepsilon_F|}\right|. \tag{3.3.17}$$

Finally, the total interband conductivity for graphene is given by

$$\sigma^{\mathrm{inter}}(\omega) = g_s g_v \sigma_0 \frac{\pi}{16}\left[\Theta(\hbar\omega - 2|\varepsilon_F|) + \frac{i}{\pi}\ln\left|\frac{\hbar\omega - 2|\varepsilon_F|}{\hbar\omega + 2|\varepsilon_F|}\right|\right], \tag{3.3.18}$$

where we have included $g_v = 2$ as the valley degeneracy [131]

3.3.2 Intraband contribution

To obtain the intraband contribution to the optical conductivity, it is sufficient to compute its imaginary part, from which the full expression can be reconstructed. The imaginary part of the intraband conductivity is given by

$$\mathbb{I}\mathrm{m}\{\sigma_{ij}^{\xi,\mathrm{intra}}\} = \frac{e^2\hbar}{\hbar\omega}\int\frac{d^2k}{(2\pi)^2}\sum_\eta\left(-\frac{\partial f(\varepsilon_\eta)}{\partial\varepsilon_\eta}\right)\left\langle\psi_\eta^\xi(\mathbf{k})\right|v_i\left|\psi_\eta^\xi(\mathbf{k})\right\rangle\left\langle\psi_\eta^\xi(\mathbf{k})\right|v_j\left|\psi_\eta^\xi(\mathbf{k})\right\rangle, \tag{3.3.19}$$

where $f(\varepsilon)$ is the Fermi-Dirac distribution. The matrix elements can be expressed in terms of v_{ij}^ξ as in Eq. (3.3.11). At zero temperature, the Fermi-Dirac distribution becomes

a step function, and its derivative turns into a Dirac delta function $\left(-\partial f(\varepsilon_\eta)/\partial \varepsilon_\eta\right) = \delta(\varepsilon_\eta - \varepsilon_F)$. Thus, the expression simplifies to

$$\mathbb{I}\mathrm{m}\{\sigma_{ij}^{\xi,\mathrm{intra}}\} = g_s\sigma_0\frac{\hbar^2}{4\pi\hbar\omega}\sum_\eta\int d^2k\, v_{ij}^{\xi}\delta(\varepsilon_\eta - \varepsilon_F). \tag{3.3.20}$$

Switching to polar coordinates, we can write

$$\mathbb{I}\mathrm{m}\{\sigma^{\xi,\mathrm{intra}}\} = g_s\sigma_0\frac{\hbar v_F}{4\hbar\omega}\sum_\eta\int dk\, k\delta(k - k_F), \tag{3.3.21}$$

Depending on the sign of the Fermi level, only one of the bands contributes, so the sum over η effectively gives a single contribution. This leads to the result

$$\mathbb{I}\mathrm{m}\{\sigma^{\xi,\mathrm{intra}}\} = g_s g_v\sigma_0\frac{1}{4\hbar\omega}|\varepsilon_F|. \tag{3.3.22}$$

Therefore, the full intraband conductivity becomes

$$\sigma^{\mathrm{intra}}(\omega) = g_s\sigma_0\frac{\pi}{2}\left[\delta(\hbar\omega) + i\frac{1}{\pi\hbar\omega}\right]|\varepsilon_F| \tag{3.3.23}$$

where we have used the Kramers-Kronig relation to include the real part [Eq. (3.3.1)].

Figure 3.2 shows the full optical conductivity. The intraband contribution dominates at low frequencies, exhibiting a Drude-like peak centered at $\omega = 0$. At higher frequencies, the interband transitions become active once the photon energy exceeds $\hbar\omega_F = 2|\varepsilon_F|$, resulting in a step-like increase in the real part. The imaginary part shows a dispersive behavior, with a sign change near the onset of interband transitions.

We notice, the optical conductivity of graphene presents a unique behavior due to its gapless, linear dispersion relation. At zero frequency, the interband contribution leads to a universal value for the real part of the conductivity, given by $\sigma^{\min} = \frac{e^2}{4\hbar}$, independent of material parameters or doping. This quantized response is a direct consequence of the relativistic-like nature of Dirac electrons in graphene and has been confirmed experimentally through optical absorption measurements [11, 12, 117].

Moreover, the inclusion of a finite Fermi level introduces a frequency window where interband transitions are Pauli-blocked, and the optical response is purely intraband. This results in a prominent Drude peak in the imaginary part of the conductivity, which diverges as $1/\omega$ when $\omega \to 0$. Such behavior is a hallmark of metallic conduction and can be tuned via doping, making graphene a versatile platform for terahertz and infrared optoelectronics [132, 133].

4

Kekulé-modulated α-$\mathcal{T}_3$ model

In this chapter, we introduce a hybrid model, a α-$\mathcal{T}_3$ model featuring a $\sqrt{3} \times \sqrt{3}$ Kekulé pattern modulation [101]. Such a hybrid system may result from the depositing of adatoms in a hexagonal lattice, where the two sublattices are displaced in the perpendicular direction, like in germanene and silicene. We derive analytical expressions for the energy dispersion and the eigenfunctions using a tight-binding approximation of nearest-neighbor hopping electrons. Finally, we include the effects of the perpendicular electric field on the band structure.

4.1 Overview

The model we propose is a hybrid system based on a honeycomb lattice (like silicene, germanene, or stanene) with an atom located at the center of each hexagon, appearing with Kekulé periodicity and a hybridizing with only one of the sublattices, as shown in Fig. 4.1 (a). This model is conceptually related to the proposal realizations of the Kek-O model [24, 112], with the key difference that we assume hybridization occurs in our system. We name this system as “Kekulé-modulated α-$\mathcal{T}_3$ model" (Kek-α), which provides a robust platform for studying valley and flat-band physics.

Experimental realizations of Kekulé-modulated systems have been reported, such as graphene on a SiC substrate intercalated with Li atoms [see Fig. 4.1 (b)], which induces Kekulé-O phase distortions [24, 54]. Importantly, the intercalation of Cs atoms in graphene layers has been experimentally achieved and shown to induce hybridization between the Cs and carbon atoms [see Fig. 4.1 (c)], leading to Brillouin zone folding and origin a flat band [74]. Moreover, theoretical proposals, such as SnI layers with Ag adatoms, achieve geometries closely resembling our proposed model [134], as shown in Fig. 4.1 (d). Building upon these developments, we envision that silicene or germanene with sublattices displaced along the z-plane [135], combined with Kekulé-patterned deposition of adatoms capable of selectively hybridizing with one sublattice, could realize

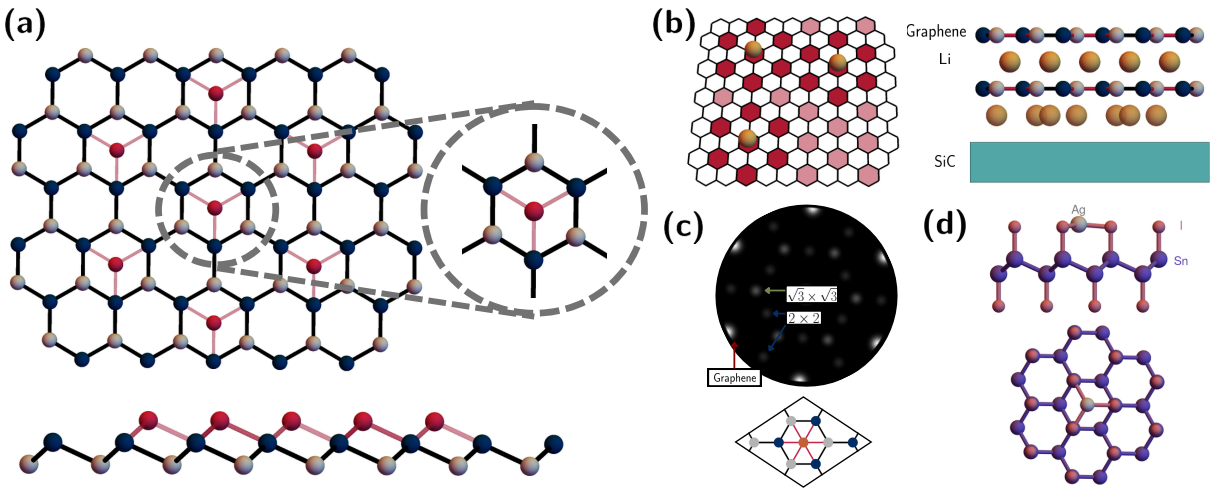

Figure 4.1: (a) Lattice structure of the proposed model. The system consists of a buckled honeycomb lattice with adatoms deposited in a $\sqrt{3}\times\sqrt{3}$ pattern. **(b)** Schematic experimental setup illustrating the realization of the Kek-O model. Adapted from [24, 54]. **(c)** Low-Energy Electron Diffraction (LEED) pattern for a Cs(2×2)/graphene/Cs($\sqrt{3}\times\sqrt{3}$)/Ir(111) heterostructure, along with the atomic geometry of the Cs/graphene unit cell. Adapted from [74]. **(d)** Crystal structure of a SnI monolayer with Ag adatoms, shown from the side (top) and top (bottom) views. Adapted from [134].

the Kek-α model experimentally. Evidence of adatom in silicene and germanene further supports the feasibility of this approach [136–139].

Given the increasing interest in space-modulated and flat-band materials, we aim to anticipate potential future developments in these systems.

4.2 Tight-binding model

We consider a honeycomb lattice with adatoms on its surface disposed with a $\sqrt{3}\times\sqrt{3}$ Kekulé periodicity. We call this superlattice with seven atoms per unit cell, Kekulé-modulated α-$\mathcal{T}_3$ model. The adatoms are located on top of the center of the hexagon (central atoms), forming a third triangular sublattice C with a larger lattice parameter that only couples with sublattice B, as shown in Fig. 4.2 (a).

The corresponding tight-binding Hamiltonian is:

$$H = -t\sum_{\mathbf{r}}\sum_{j=1}^{3} b_{\mathbf{r}}^{\dagger} a_{\mathbf{r}-\boldsymbol{\delta}_j} - \sum_{\mathbf{r}'}\sum_{j=1}^{3} t' c_{\mathbf{r}'}^{\dagger} b_{\mathbf{r}'-\boldsymbol{\delta}_j} + \text{H.c.}, \tag{4.2.1}$$

where the first term describes the honeycomb lattice, with t the hopping energy between nearest neighbor sites belonging to sublattices A and B, connected by the vectors $\boldsymbol{\delta}_1 = \frac{a}{2}(\sqrt{3},-1)$, $\boldsymbol{\delta}_2 = -\frac{a}{2}(\sqrt{3},1)$, $\boldsymbol{\delta}_3 = a(0,1)$. Here a is the atomic distance.

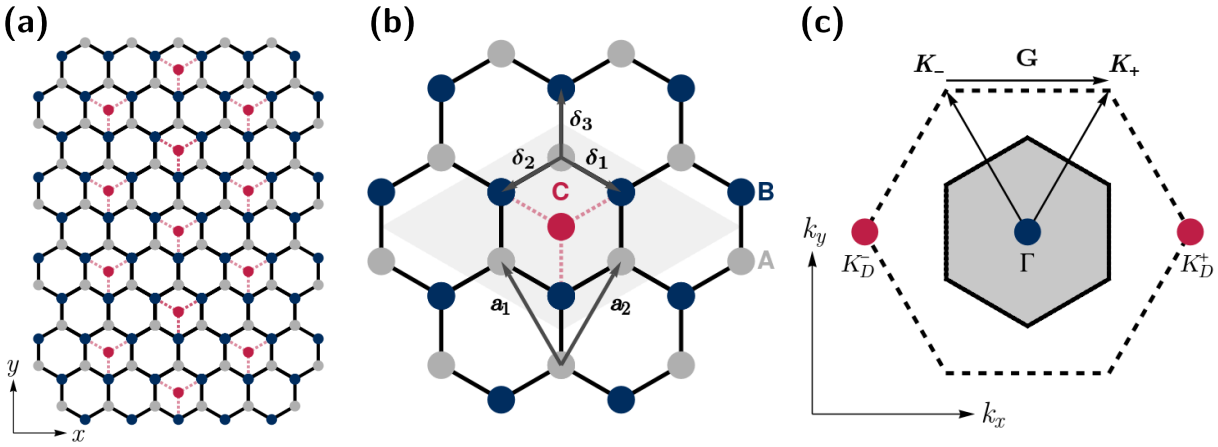

Figure 4.2: **(a)** Lattice structure of Kekulé-modulated α-$\mathcal{T}_3$ model. Atoms on sublattices A and B are depicted as gray and blue circles, respectively. The central atoms in red appear with Kekulé periodicity and only connect with the B sublattice. **(b)** The basis vectors of the honeycomb lattice are $\mathbf{a}_1$ and $\mathbf{a}_2$. The vectors $\boldsymbol{\delta}_1$, $\boldsymbol{\delta}_2$, and $\boldsymbol{\delta}_3$ connect each A or B atom to its nearest neighbors. The gray parallelogram represents the unit cell of the superlattice. **(c)** Reciprocal space with vectors $\mathbf{K}_\pm$. The original (honeycomb lattice) Brillouin zone is represented as a black dashed hexagon. The $K_D^\pm$ valleys (at the red Dirac points) are coupled by the wave vector $\mathbf{G} = \mathbf{K}_+ - \mathbf{K}_-$ and folded onto the center of the superlattice Brillouin zone (blue point).

Thus, the honeycomb lattice vectors are $\mathbf{a}_1 = \boldsymbol{\delta}_3 - \boldsymbol{\delta}_1$ and $\mathbf{a}_2 = \boldsymbol{\delta}_3 - \boldsymbol{\delta}_2$, such that the atoms have positions $\mathbf{r} = n\mathbf{a}_1 + m\mathbf{a}_2$ $(n, m \in \mathbb{Z})$ in sublattice B and $\mathbf{r} + \boldsymbol{\delta}_3$ in sublattice A (see Fig. 1(b)). The second term describes the coupling between central atoms at $\mathbf{r}' = n(2\mathbf{a}_1 - \mathbf{a}_2) + m(2\mathbf{a}_2 - \mathbf{a}_1)$ and nearest neighbor atoms in sublattice B, with $t' = \alpha t$ the corresponding hopping energy. The parameter α varies continuously between 0 and 1, interpolating between the honeycomb $(\alpha = 0)$ and a dice lattice with Kekulé periodicity $(\alpha = 1)$.

In order to describe the superlattice (Kek-α) with the hexagonal Brillouin zone, we consider additional sites added in sublattice C but with zero amplitude hoppings, in such a way that we can sum over all the cells $\mathbf{r}' = \mathbf{r} + \boldsymbol{\delta}_3$ replacing $t' \to t_{\mathbf{r},j}$, with

$$t_{\mathbf{r},j} = \alpha t\{1 + 2\mathbb{R}e[e^{i\mathbf{G}\cdot(\mathbf{r}+\boldsymbol{\delta}_j)}]\}, \tag{4.2.2}$$

where the Kekulé wave vector is the "distance" between valleys, defined as $\mathbf{G} = \mathbf{K}_+ - \mathbf{K}_-$ (see Fig. 4.2 (b)). A detailed derivation of the hopping amplitudes is provided in Appendix B.1.

The corresponding Hamiltonian in momentum space is given by

$$H = -\sum_{\mathbf{k}} a_{\mathbf{k}}^\dagger f(\mathbf{k}) b_{\mathbf{k}} - \alpha \sum_{\mathbf{k}} \left[b_{\mathbf{k}}^\dagger f(\mathbf{k}) c_{\mathbf{k}} + b_{\mathbf{k}+\mathbf{G}}^\dagger f(\mathbf{k}+\mathbf{G}) c_{\mathbf{k}} + b_{\mathbf{k}-\mathbf{G}}^\dagger f(\mathbf{k}-\mathbf{G}) c_{\mathbf{k}} \right] + \text{H.c.}, \tag{4.2.3}$$

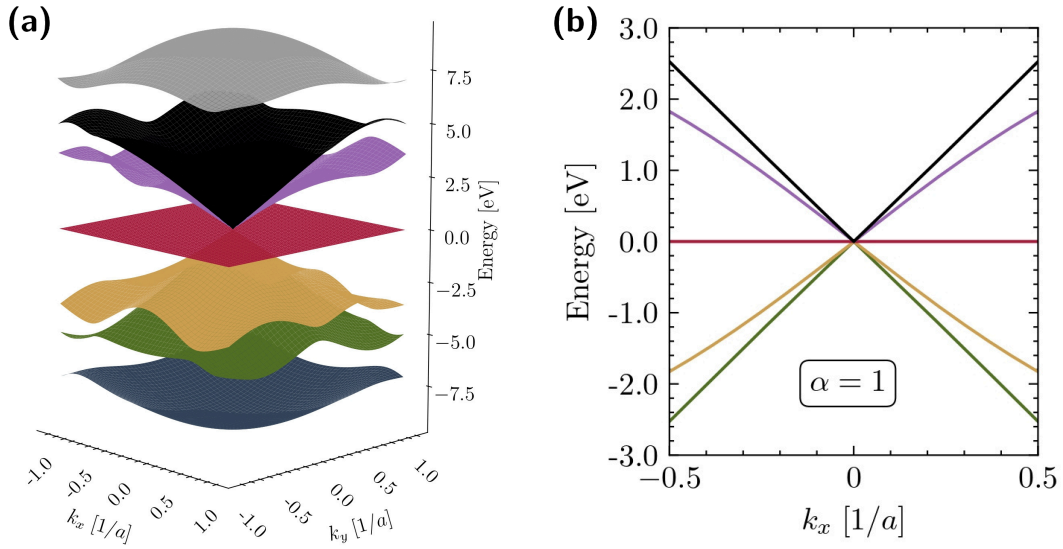

Figure 4.3: (a) Energy band structure of the Kek-α model obtained by a direct diagonalization of the tight-binding Hamiltonian defined by the lattice shown in Fig. 4.2 (b). **(b)** Dispersion relation near the center of the superlattice Brillouin zone. The spectrum displays dispersive bands plus a flat band at zero energy originating from the bonded central atoms. We consider $t = 2.7$ eV and $\alpha = 1$.

where we have defined,

$$f(\mathbf{k}) = t\sum_{j=1}^{3} e^{i\mathbf{k}\cdot\boldsymbol{\delta}_j}. \tag{4.2.4}$$

with the momentum $\mathbf{k}$ varying in the original (honeycomb lattice) Brillouin zone. In order to restrict $\mathbf{k}$ to the superlattice Brillouin zone, we group the annihilation operators at $\mathbf{k}$ and $\mathbf{k}\pm\mathbf{G}$ in the column vector $\Psi_{\mathbf{k}} = (a_{\mathbf{k}}, a_{\mathbf{k}-\mathbf{G}}, a_{\mathbf{k}+\mathbf{G}}, b_{\mathbf{k}}, b_{\mathbf{k}-\mathbf{G}}, b_{\mathbf{k}+\mathbf{G}}, c_{\mathbf{k}}, c_{\mathbf{k}-\mathbf{G}}, c_{\mathbf{k}+\mathbf{G}})^{\mathrm{T}}$, and write the Hamiltonian in a 9×9 matrix form:

$$H = -\Psi_{\mathbf{k}}^{\dagger}\mathcal{H}(\mathbf{k})\Psi_{\mathbf{k}}, \tag{4.2.5}$$

where

$$\mathcal{H}(\mathbf{k}) = \begin{pmatrix} \mathbf{0} & \mathcal{F}(\mathbf{k}) & \mathbf{0} \\ \mathcal{F}^{\dagger}(\mathbf{k}) & \mathbf{0} & \alpha\mathcal{E}(\mathbf{k}) \\ \mathbf{0} & \alpha\mathcal{E}^{\dagger}(\mathbf{k}) & \mathbf{0} \end{pmatrix}, \tag{4.2.6}$$

and

$$\mathcal{F}(\mathbf{k}) = \begin{pmatrix} f_0 & 0 & 0 \\ 0 & f_{-1} & 0 \\ 0 & 0 & f_1 \end{pmatrix}, \quad \mathcal{E}(\mathbf{k}) = \begin{pmatrix} f_0 & f_0 & f_0 \\ f_{-1} & f_{-1} & f_{-1} \\ f_1 & f_1 & f_1 \end{pmatrix}, \tag{4.2.7}$$

with $f_n = f(\mathbf{k} + n\mathbf{G})$, and we have used the relation $f(\mathbf{k}\pm 2\mathbf{G}) = f(\mathbf{k}\mp\mathbf{G})$ [25]. The full derivation, including the detailed basis transformation and intermediate steps, is provided in Appendix B.2.

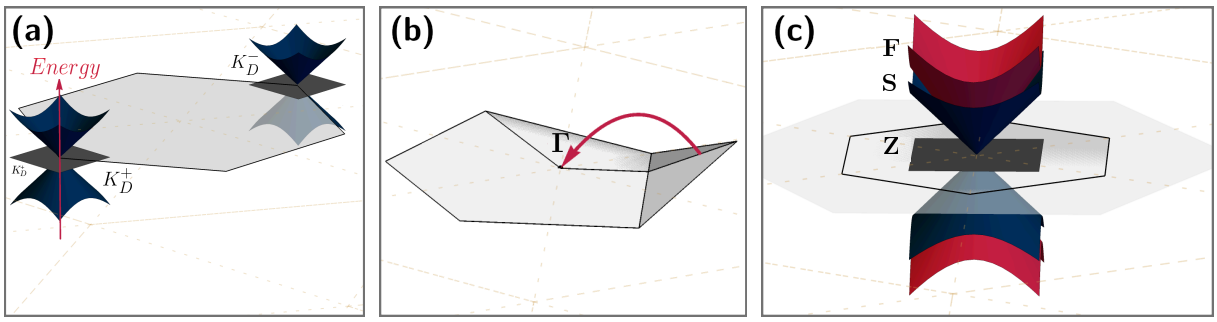

Figure 4.4: (a) Brillouin zone of the $\alpha-\mathcal{T}_3$ model in reciprocal space is shown as a gray hexagon. The two inequivalent valleys are situated in the corners of the hexagon. **(b)** Brillouin zone folding due to the Kekulé periodicity. **(c)** Energy dispersion relation of Kek-α around the Γ in the folded Brillouin zone. The label **Z** designates the flat band with "zero" velocity, **S** denotes the "slow" cone with velocity v_F, and **F** signifies the "fast" cone with velocity $\Delta_\alpha v_F$.

In Fig. 4.3, we show the energy dispersion of Kek-α superlattice. The Kekulé periodicity brings the valleys into the Γ point, as observed in Kekulé-distorted graphene [25], with the addition of a flat band due to the presence of central sites. Here, we assume that the coupling occurs only with one sublattice, while other possible couplings are neglected due to their significantly weaker magnitude, as a consequence of the sublattice displacement along the z-axis.

4.3 Low energy Hamiltonian

An effective Hamiltonian for low energies can be obtained considering $\alpha \lesssim 1$ and by noticing that the rows and columns of the matrices and associated with modes $a_{\mathbf{k}}$, $b_{\mathbf{k}}$, and $c_{\mathbf{k}}$ (illustrated in blue and gray in Fig. 4.3) lead to high energy bands, thus negligible in the low energy limit. Consequently, in this limit the spectrum is primarily determined by six modes, denoted as $u_{\mathbf{k}} = (a_{\mathbf{k}-\mathbf{G}}, a_{\mathbf{k}+\mathbf{G}}, b_{\mathbf{k}-\mathbf{G}}, b_{\mathbf{k}+\mathbf{G}}, c_{\mathbf{k}-\mathbf{G}}, c_{\mathbf{k}+\mathbf{G}})$. Projecting onto this subspace results in the reduction of the nine-band Hamiltonian to an effective six-band Hamiltonian

$$H_{\text{eff}} = u_{\mathbf{k}}^{\dagger} \begin{pmatrix} \mathbf{0} & g(\mathbf{k}) & \mathbf{0} \\ g^{\dagger}(\mathbf{k}) & \mathbf{0} & \alpha h(\mathbf{k}) \\ \mathbf{0} & \alpha h^{\dagger}(\mathbf{k}) & \mathbf{0} \end{pmatrix} u_{\mathbf{k}}, \tag{4.3.1}$$

where

$$g(\mathbf{k}) = \begin{pmatrix} f_{-1} & 0 \\ 0 & f_1 \end{pmatrix}, \qquad h(\mathbf{k}) = \begin{pmatrix} f_{-1} & f_{-1} \\ f_1 & f_1 \end{pmatrix}. \tag{4.3.2}$$

We identify the K valley with $+\mathbf{G}$ and the K' valley with $-\mathbf{G}$. The $\mathbf{k}$-dependence of $f_{\pm 1}$ may be linearized near $\mathbf{k} = 0$, leading to $f_{\pm 1}(k_x, k_y) = \hbar v_F(\mp k_x + i k_y)$, where $v_F = 3at/2\hbar$

is the Fermi velocity. Finally, we can write a Dirac-like equation for the Kek-α model as

$$\mathcal{H}\begin{pmatrix}\Psi_K\\ \Psi_{K'}\end{pmatrix} = \varepsilon\begin{pmatrix}\Psi_K\\ \Psi_{K'}\end{pmatrix},\ \mathcal{H} = \begin{pmatrix}\hbar v_F \mathbf{k}\cdot\mathbf{S} & Q\\ Q^\dagger & \hbar v_F \mathbf{k}\cdot\mathbf{S}^*\end{pmatrix}, \tag{4.3.3}$$

$$\Psi_K = \begin{pmatrix}\psi_{A,K}\\ -\psi_{B,K}\\ \psi_{C,K}\end{pmatrix}, \qquad \Psi_{K'} = \begin{pmatrix}\psi_{A,K'}\\ \psi_{B,K'}\\ \psi_{C,K'}\end{pmatrix}, \tag{4.3.4}$$

$$Q = \alpha\hbar v_F \begin{pmatrix}0 & 0 & 0\\ 0 & 0 & ke^{i\theta_k}\\ 0 & ke^{i\theta_k} & 0\end{pmatrix}, \tag{4.3.5}$$

where $k = |\mathbf{k}|$, $\theta_\mathbf{k} = \tan^{-1}(k_x/k_y)$, $\mathbf{S} = (S_x, S_y)$. The pseudospin operators S_x and S_y are defined as

$$S_x = \begin{pmatrix}0 & 1 & 0\\ 1 & 0 & \alpha\\ 0 & \alpha & 0\end{pmatrix},\ \ S_y = \begin{pmatrix}0 & -i & 0\\ i & 0 & -\alpha i\\ 0 & \alpha i & 0\end{pmatrix}. \tag{4.3.6}$$

To determine the energy spectrum of the Kek-α model, we start from the Bloch Hamiltonian in Eq. (B.2.9). The energy eigenvalues are obtained by solving the characteristic equation $\det[\mathcal{H}(\mathbf{k}) - \varepsilon\mathbb{I}_{6\times6}] = 0$, where $\mathbb{I}_{6\times6}$ is the identity matrix. By computing the determinant blockwise, the problem simplifies to evaluating:

$$\begin{aligned}\det[\mathcal{H}(\mathbf{k}) - \varepsilon\mathbb{I}_{6\times6}] &= \det[-\varepsilon(\varepsilon^2\mathbb{I}_{2\times2} - \alpha^2 h(\mathbf{k})h^\dagger(\mathbf{k})) + \varepsilon g(\mathbf{k})g^\dagger(\mathbf{k})],\\ &= \det[\varepsilon\mathbb{I}_{2\times2}]\cdot\det[\alpha^2 h(\mathbf{k})h^\dagger(\mathbf{k}) + g(\mathbf{k})g^\dagger(\mathbf{k}) - \varepsilon^2\mathbb{I}_{2\times2}].\end{aligned} \tag{4.3.7}$$

This reveals a doubly degenerate flat band at $\varepsilon = 0$. For the remaining four bands, we focus on the second determinant, which reduces to

$$\begin{aligned}\det[\alpha^2 h(\mathbf{k})h^\dagger(\mathbf{k}) + g(\mathbf{k})g^\dagger(\mathbf{k}) - \varepsilon^2\mathbb{I}_{2\times2}] &= \det\left[\begin{pmatrix}(2\alpha^2+1)|f_{-1}|^2 - \varepsilon^2 & 2f_{-1}f_1^*\\ 2f_1 f_{-1}^* & (2\alpha^2+1)|f_1|^2 - \varepsilon^2\end{pmatrix}\right],\\ &= \varepsilon^4 - 2\varepsilon^2(2\alpha^2+1)|f_1|^2 + (4\alpha^2+1)|f_1|^4,\end{aligned} \tag{4.3.8}$$

assuming $|f_{-1}|^2 = |f_1|^2$. Solving this quartic equation yields:

$$\begin{aligned}\varepsilon_\pm^2 &= \left[(2\alpha^2+1) \pm \sqrt{(2\alpha^2+1)^2 - (4\alpha^2+1)}\right]|f_1|^2,\\ &= [2\alpha^2(1\pm1)+1]|f_1|^2,\end{aligned} \tag{4.3.9}$$

which corresponds to two pairs of particle-hole symmetric bands. Expressing $|f_1|^2$ in terms of the Dirac momentum, $|f_1|^2 = \hbar^2 v_F^2 k^2$, we find the dispersion relation:

$$\varepsilon_\eta^\xi(\mathbf{k}) = \eta\hbar v_F(\Delta_\alpha)^\xi k \tag{4.3.10}$$

where $\Delta_\alpha = \sqrt{4\alpha^2+1}$, η is the index band, $\eta = 1$ for the conduction band, $\eta = -1$ for the valence band, and $\eta = 0$ for the flat band, and $\xi = \{0, 1\}$ distinguishes between the two propagation velocities.

This result reveals the low-energy band structure of the Kek-α model: a distinctive double cone structure, referred to as "fast" ($\mathbf{F}_\pm$) and "slow" ($\mathbf{S}_\pm$) cones, along with a doubly-degenerate flat band denoted as "zero" ($\mathbf{Z}$). The index $\xi = \{0, 1\}$ labels the two degenerate flat bands ($\mathbf{Z}^\xi$) and the two cones, defining two velocities: the 'fast velocity' $v_F\Delta_\alpha$ ($\xi = 1$) and the 'slow velocity' v_F ($\xi = 0$), associated to the fast cones $\mathbf{F}_\pm$ and slow cones $\mathbf{S}_\pm$, respectively.

In the α-$\mathcal{T}_3$ model, rescaling the energy renders the spectrum independent of α [22, 96]. However, in our case, such rescaling is not possible, and the spectrum remains α-dependent because the Kekulé term couples with one sublattice only. Thus, when the two valleys fold onto the Γ point (see Fig. 4.4 (b)) one of the cones show a strong dependence on α and the other remains independent.

The eigenfunctions ψ^ξ_η are given by

$$\psi^0_0(\mathbf{k}) = \frac{1}{\sqrt{2}}\begin{pmatrix} 0 \\ 0 \\ -1 \\ 0 \\ 0 \\ 1 \end{pmatrix}, \quad \psi^1_0(\mathbf{k}) = \frac{1}{\sqrt{8\alpha^2+2}}\begin{pmatrix} 2\alpha e^{-i2\theta_\mathbf{k}} \\ 0 \\ -1 \\ 2\alpha e^{i2\theta_\mathbf{k}} \\ 0 \\ -1 \end{pmatrix},$$

for the flat bands, and

$$\psi^0_\pm(\mathbf{k}) = \frac{1}{2}\begin{pmatrix} \pm e^{-i2\theta_\mathbf{k}} \\ -e^{-i\theta_\mathbf{k}} \\ 0 \\ \mp e^{i2\theta_\mathbf{k}} \\ e^{i\theta_\mathbf{k}} \\ 0 \end{pmatrix}, \quad \psi^1_\pm(\mathbf{k}) = \frac{1}{2\Delta_\alpha}\begin{pmatrix} e^{-i2\theta_\mathbf{k}} \\ \pm\Delta_\alpha e^{-i\theta_\mathbf{k}} \\ 2\alpha \\ e^{i2\theta_\mathbf{k}} \\ \pm\Delta_\alpha e^{i\theta_\mathbf{k}} \\ 2\alpha \end{pmatrix},$$

for the slow and fast cone, respectively. Two distinctive aspects of the present model are reflected in these eigenstates. First, the states ψ^0_0 and ψ^1_0 are degenerate. This is due to the Brillouin zone folding induced by the Kekulé periodicity, which merges the valley states associated with the flat band. Second, only the fast states $\psi^1_\pm$ depend on the coupling parameter α, while the slow states $\psi^0_\pm$ remain identical to those of pristine graphene. This introduces an asymmetry between the fast and slow states of the nested cones which is absent in the pure Kek-Y model, where both cones depend on the Kekulé coupling. We verify that the low-energy analytical approximation, at low-energy, remain consistent with numerical calculations up to $\alpha = 0.45$.

4.4 Gapped Kek-α with a deformed flat band

In the ideal case, the proposed Kek-α model features a gapless energy spectrum with two Dirac cones and a perfectly flat band lying at the Fermi level, resembling known properties of the α-$\mathcal{T}_3$ lattice. However, real systems often deviate from this idealized scenario, and one physically relevant perturbation is the applied perpendicular electric

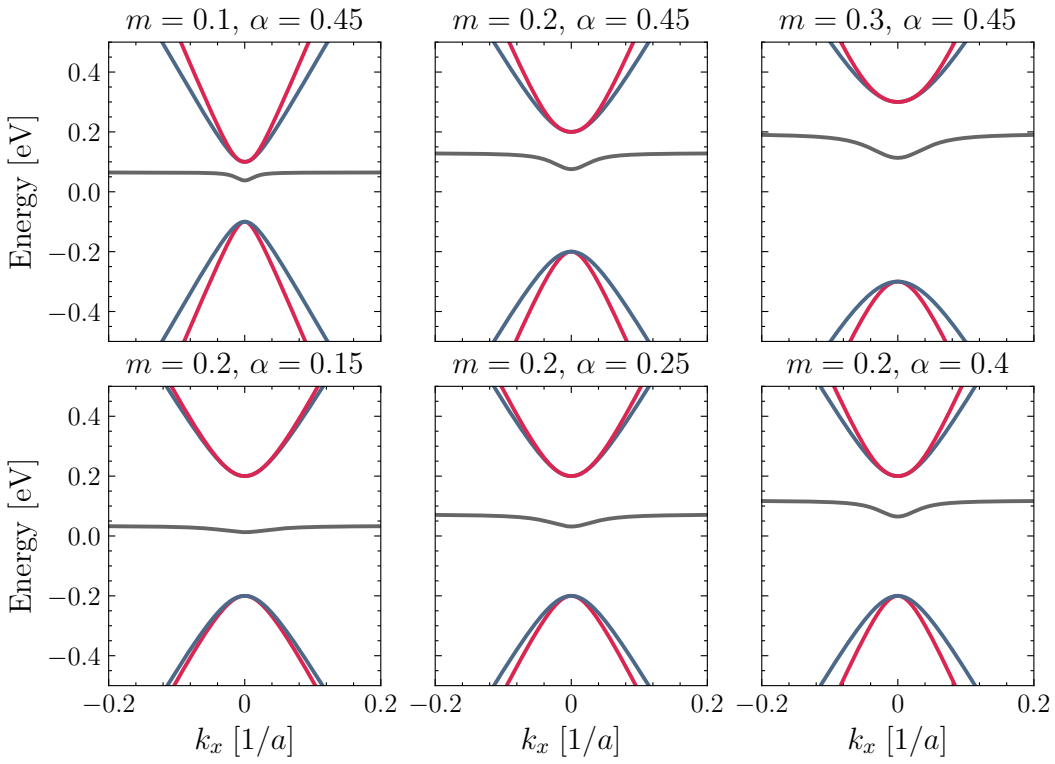

Figure 4.5: Band structure near the center of the superlattice Brillouin zone for the gapped Kek-α model. Top: evolution with on-site energy m. Bottom: evolution with coupling parameter α. The spectrum consists of two dispersive bands and a curved flat band originating from the central atoms. Calculations are performed with $t = 2.7$ eV.

field. The effect of this field can be captured in the effective model through an on-site potential m acting only on the A and B sites, which introduces an energy imbalance between the lattice sites. Once this term is included, the band structure becomes gapped and, more interestingly, the flat band is no longer preserved: it shifts away from the Fermi level and becomes dispersive.

We performed numerical tight-binding calculations considering nearest-neighbor hoppings in the enlarged unit cell [see Fig. 4.2 (b)]. The band structures were obtained by diagonalizing the corresponding 7×7 Bloch Hamiltonian $H(\mathbf{k})$ along the k_x-axis path in reciprocal space, where we compute the seven eigenvalues of $H(\mathbf{k})$ at each momentum point. The explicit matrix representation and numerical implementation are provided in Appendix C. The resulting band structure reveals that the previously flat band becomes curved under the effect of a finite m around the Γ point, exhibiting a characteristic deformation whose nature depends on both m and the coupling parameter α. Figure 4.5 shows the band structure near Γ point for several values of m (top row) and α (bottom row). As expected, increasing m opens a band gap at the Γ point. Simultaneously, the flat band moves away from the Fermi level and acquires a finite bandwidth. This deformation becomes more pronounced as m increases. Similarly, varying α modifies both

the curvature of the flat band and the separation between the Dirac cones. These observations are consistent with previous findings on gapped α-$\mathcal{T}_3$ systems [140], where it has been shown that the introduction of a band gap leads to a deformation of the flat band.

Finally, the deformed flat band is no longer pinned at the Fermi level, and its acquired curvature results in a finite density of states, which may have significant implications for transport and optical properties. A comprehensive theoretical analysis is still needed to quantify and interpret these effects. Moreover, a detailed study of the mechanism behind breaking the flat band's degeneracy, goes beyond the scope of the present work and requires a more thorough analysis. Nevertheless, our findings highlight that the interplay between the on-site potential m and the coupling parameter α gives rise to a rich and tunable band structure, offering potential avenues for the design of flat-band systems with controllable electronic features.

5

Optical response of Kekulé systems

This chapter is devoted to the study of the optical conductivity in honeycomb lattice with Kekulé modulation. Three distinct variants of the Kekulé pattern are considered: the Kek-O model, the Kek-Y model, and the Kekulé-modulated α-$\mathcal{T}_3$ model (Kek-α) model, the latter being introduced and developed in this work.

The optical conductivities of the Kek-O and Kek-Y models have been previously reported in the literature. For this reason, only their key results are briefly presented here as a point of reference and comparison [56, 58, 141]. In contrast, the optical response of the Kek-α model is derived in full detail, including the joint density of states, the identification of allowed optical transitions, and the explicit conductivity calculation. These results were also disseminated in Ref. [101].

In addition to the zero-temperature results, a separate section discusses the effects of finite temperature on optical conductivity. Finally, we analyze specific spectral features that can interpreted as signatures of Kekulé periodicity, which may serve as experimental indicators of this modulation type in two-dimensional systems.

5.1 Current response in Kekulé-modulated systems

The lattice and band structures of the Kekulé models play a crucial role in determining the allowed optical transitions and the overall frequency-dependent response [see Fig. 5.1]. In particular, the presence or absence of a band gap, the location of Dirac cones, and the degree of valley splitting all directly impact the joint density of states and the optical conductivity.

The optical conductivity tensor in the three cases of Kekulé modulation reduces to a scalar response function, with real and imaginary parts

$$\mathbb{R}\mathrm{e}\{\sigma(\omega)\} = D\delta(\omega) + \mathbb{R}\mathrm{e}\{\sigma^{\mathrm{inter}}(\omega)\}\,, \tag{5.1.1}$$

$$\mathbb{I}\mathrm{m}\{\sigma(\omega)\} = \mathbb{I}\mathrm{m}\{\sigma^{\mathrm{intra}}(\omega)\} + \mathbb{I}\mathrm{m}\{\sigma^{\mathrm{inter}}(\omega)\}\,, \tag{5.1.2}$$

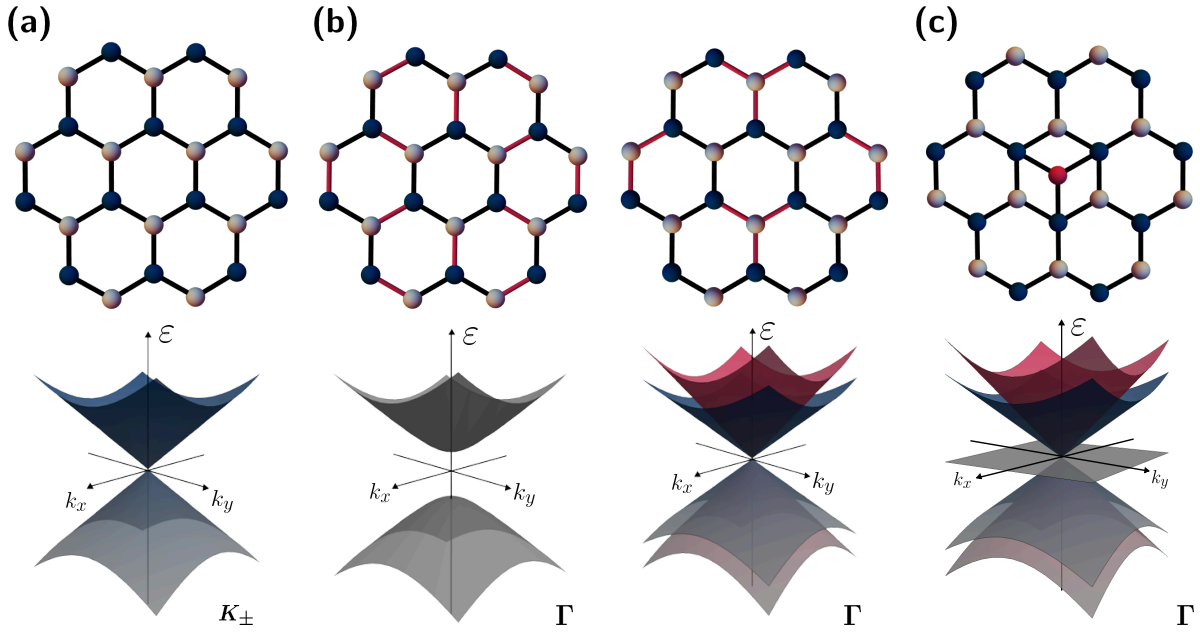

Figure 5.1: Lattice structure and band structure of **(a)** pristine graphene, **(b)** Kekulé-distorted graphene (Kek-O and Kek-Y), and **(c)** the Kekulé-modulated α-$\mathcal{T}_3$ model (Kek-α). These band structures are shown here to highlight the key differences that influence the optical response of each system.

where the intraband and interband contributions are obtained from the current-current Kubo formula as

$$\sigma^{\text{intra}}(\omega) = i g_s \frac{\sigma_0}{4\pi\hbar\omega} \sum_\lambda \int d^2k\, \delta(\varepsilon_\lambda - \varepsilon_F) \left(\frac{\partial \varepsilon_\lambda}{\partial k_x}\right)^2, \tag{5.1.3}$$

$$\mathbb{R}\text{e}\{\sigma^{\text{inter}}(\omega)\} = g_s \sigma_0 \frac{\hbar\omega}{4} \sum_\lambda \int' d^2k\, V_{\lambda,\lambda'}(\mathbf{k})\, \delta(\varepsilon_\lambda(\mathbf{k}) - \varepsilon_{\lambda'}(\mathbf{k}) - \hbar\omega), \tag{5.1.4}$$

$$\mathbb{I}\text{m}\{\sigma^{\text{inter}}(\omega)\} = g_s \sigma_0 \frac{\hbar\omega}{2\pi} \sum_{\lambda,\lambda'} \mathcal{P} \int' d^2k\, V_{\lambda,\lambda'}(\boldsymbol{k}) \frac{\varepsilon_\lambda(\boldsymbol{k}) - \varepsilon_{\lambda'}(\boldsymbol{k})}{(\hbar\omega)^2 - (\varepsilon_\lambda(\boldsymbol{k}) - \varepsilon_{\lambda'}(\boldsymbol{k}))^2}, \tag{5.1.5}$$

assuming zero temperature. Here, $\sigma_0 = 2e^2/h$, λ is the band index and $\mathcal{P}$ denotes Principal Value integral. The function $V_{\lambda,\lambda'}(\mathbf{k})$ arises from the product of matrix elements of the velocity operator or in terms of the interband Berry connection as $V_{\lambda,\lambda'}(\mathbf{k}) = \mathcal{A}_{\lambda,\lambda'}(\mathbf{k})\mathcal{A}_{\lambda',\lambda}(\mathbf{k})$ where $\mathcal{A}_{\lambda,\lambda'}(\mathbf{k}) = i\langle\lambda,\mathbf{k}|\partial_{k_i}|\lambda',\mathbf{k}\rangle$ is the k_i-component, with $i = \{x, y\}$, of the interband Berry connection. We choose $i = x$ for concreteness given the isotropy of the model. The elements $V_{\lambda,\lambda'}(\mathbf{k})$ are given by:

$$V_{\lambda,\lambda'}(\mathbf{k}) = \frac{\langle\lambda,\mathbf{k}|\,\partial_{k_x}\mathcal{H}\,|\lambda',\mathbf{k}\rangle\,\langle\lambda',\mathbf{k}|\,\partial_{k_x}\mathcal{H}\,|\lambda,\mathbf{k}\rangle}{[\varepsilon_\lambda(\mathbf{k}) - \varepsilon_{\lambda'}(\mathbf{k})]^2}. \tag{5.1.6}$$

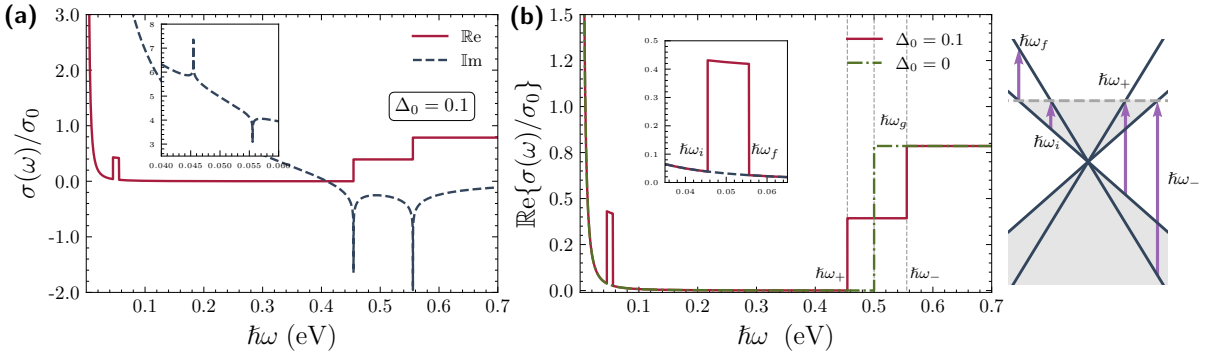

Figure 5.2: **(a)** Real and imaginary parts of the optical conductivity $\sigma(\omega)$ for the Kek-Y model. **(b)** The real part of $\sigma(\omega)$ for $\Delta_0 = 0$ (graphene) and $\Delta_0 = 0.1$ (Kek-Y). The diagram on the right shows the allowed transitions contributing to the conductivity. We take $\varepsilon_F = 0.25\,\text{eV}$.

The prime indicates integration over domains defined by the position of the Fermi energy according to the condition $\varepsilon_{\lambda'}(\mathbf{k}) < \varepsilon_F < \varepsilon_\lambda(\mathbf{k})$. We have included in Eq. (5.1.1) the Drude weight $D = \pi \lim_{\omega\to 0}[\omega \mathbb{I}\text{m}\{\sigma^{\text{intra}}(\omega)\}]$ [142].

These expressions form the basis for the analysis of the frequency-dependent conductivity for the Kekulé-modulated systems in the following sections.

5.2 Kekulé-distorted graphene

5.2.1 Kek-Y phase

The broken-valley degeneracy generates that the spectrum Kek-Y phase distortion consists of two concentric gapless Dirac cones, referred to as "fast" ($\mathbf{F}_\pm$) and "slow" ($\mathbf{S}_\pm$) cones [25, 58]. The energy dispersion relation is given by

$$\varepsilon_\eta^\xi(\mathbf{k}) = \eta\hbar v_F(1 + \xi\Delta_0)k \tag{5.2.1}$$

where Δ_0 is the Kekulé modulation parameter, $\eta = \pm 1$ is the index band for the conduction and valence band, respectively. The index $\xi = \pm 1$ labels the two cones, defining two velocities: the 'fast velocity' $v_F(1 + \Delta_0)$ ($\xi = 1$) and the 'slow velocity' $v_F(1 - \Delta_0)$ ($\xi = -1$), associated to the fast cones $\mathbf{F}_\pm$ and slow cones $\mathbf{S}_\pm$, respectively.

The Fermi contours, defined by the condition $\varepsilon_\eta^\xi(\mathbf{k}) = \varepsilon_F$, depend on the position of the Fermi energy and the magnitude of the modulation parameter Δ_0. In the Kek-Y phase, allowed optical transitions occur only between states belonging to different cones — a phenomenon known as intervalley transitions (e.g., $\mathbf{S}_- \to \mathbf{F}_+$, $\mathbf{S}_+ \to \mathbf{F}_-$, $\mathbf{S}_+ \to \mathbf{F}_+$). Transitions between states within the same cone are forbidden due to symmetry constraints specific to the Kek-Y distortion [58, 60].

The total conductivity has intraband and interband contributions, $\sigma(\omega) = \sigma^{\text{intra}}(\omega) +$

$\sigma^{\text{inter}}(\omega)$. The intraband conductivity, as in pristine graphene, is given by

$$\sigma^{\text{intra}}(\omega) = g_s\sigma_0\frac{\pi}{2}\left[\delta(\hbar\omega) + i\frac{1}{\pi\hbar\omega}\right]|\varepsilon_F|. \tag{5.2.2}$$

This expression remains unchanged from the pristine graphene case, as the distortion does not affect the transport properties within each cone. A modification of the intraband contribution would arise, for instance, in the presence of anisotropic effects in the energy spectrum [143].

We divide the interband contribution as

$$\sigma^{\text{inter}}(\omega) = \sigma^{\text{inter}}_{>}(\omega)\Theta(\hbar\omega - |\varepsilon_F|) + \sigma^{\text{inter}}_{<}(\omega)\Theta(|\varepsilon_F| - \hbar\omega), \tag{5.2.3}$$

where $\sigma^{\text{inter}}_{>}(\omega)$ considers contributions above the Fermi energy, that is the sum of all permitted interband transitions, excluding $\mathbf{S}_+ \to \mathbf{F}_+$ (or $\mathbf{F}_- \to \mathbf{S}_-$ when $\varepsilon_F < 0$), and $\sigma^{\text{inter}}_{<}(\omega)$ considers contributions below the Fermi energy, that is, the intervalley transitions $\mathbf{S}_+ \to \mathbf{F}_+$ and $\mathbf{F}_- \to \mathbf{S}_-$. Therefore

$$\sigma^{\text{inter}}_{>}(\omega) = g_s\sigma_0\frac{\pi}{16}\left\{\Theta(\hbar\omega - \hbar\omega_+) + \Theta(\hbar\omega - \hbar\omega_-) - \frac{i}{\pi}\ln\left|\frac{\hbar\omega + \hbar\omega_+}{\hbar\omega - \hbar\omega_+}\cdot\frac{\hbar\omega + \hbar\omega_-}{\hbar\omega - \hbar\omega_-}\right|\right\}, \tag{5.2.4}$$

$$\sigma^{\text{inter}}_{<}(\omega) = g_s\frac{\sigma_0\pi}{16}\left\{\Theta\left(\hbar\omega - \hbar\omega_i\right)\Theta\left(\hbar\omega_f - \hbar\omega\right) + \frac{i}{\pi}\ln\left|\frac{\hbar\omega - \hbar\omega_f}{\hbar\omega + \hbar\omega_f}\cdot\frac{\hbar\omega + \hbar\omega_i}{\hbar\omega - \hbar\omega_i}\right|\right\}. \tag{5.2.5}$$

In this case , $\hbar\omega_g = 2|\varepsilon_F|$ corresponds to the onset for the intravalley transitions, while $\hbar\omega_- = 2|\varepsilon_F|/(1-\Delta_0)$, $\hbar\omega_+ = 2|\varepsilon_F|/(1+\Delta_0)$, and $\hbar\omega_i = 2\Delta_0|\varepsilon_F|/(1+\Delta_0)$, $\hbar\omega_f = 2\Delta_0|\varepsilon_F|/(1-\Delta_0)$, to the intervalley transitions.

We note that the Kekulé-Y distortion opens an inter-cone transition channel that is absent in pristine graphene (see Fig. 5.2) [58, 59]. The characteristic step-like absorption spectrum of graphene is split into two half-steps due to the onset of absorption in each valley occurring at different characteristic frequencies, resembling the behavior of a 3/2 pseudospin Dirac semimetal. Additionally, an absorption feature below the Fermi energy emerges from the intervalley transition $\mathbf{S}_+ \to \mathbf{F}_+$. This low-energy absorption may serve as a distinctive signature of the Kekulé-Y phase [59, 63].

5.2.2 Kek-O phase

The Kek-O pattern induces a band gap in honeycomb lattice. The low-energy spectrum for Kek-O consists of a doubly degenerate massive band [25, 40]. The energy dispersion relation is given by

$$\varepsilon_\eta(\mathbf{k}) = \eta\sqrt{(\hbar v_F k)^2 + (\tilde{\Delta})^2} \tag{5.2.6}$$

where $\eta = \pm 1$ is the index band for the conduction and valence band, respectively. And the parameter $\tilde{\Delta} = 3t\Delta_0$, with Δ_0 the Kekulé modulation parameter and t the hopping parameter. The band gap at the Γ point is $\varepsilon_g = 2\tilde{\Delta}$.

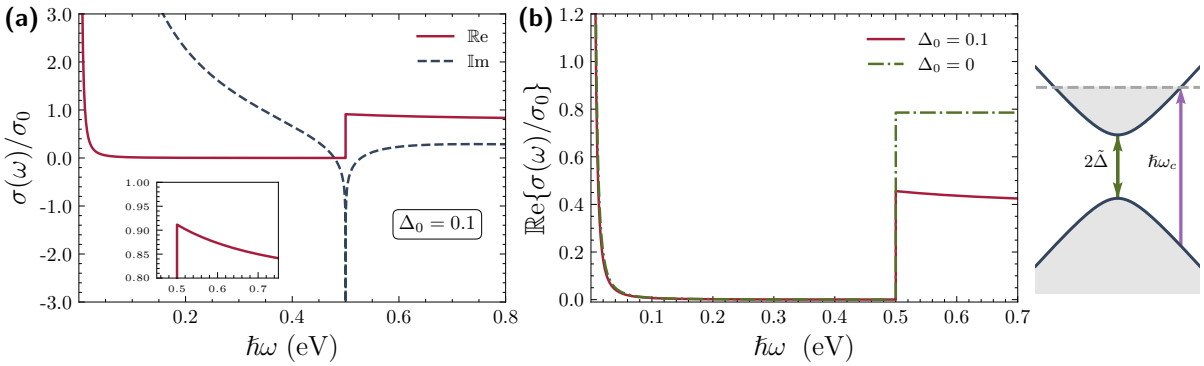

Figure 5.3: **(a)** Real and imaginary parts of the optical conductivity $\sigma(\omega)$ for the Kek-O model. **(b)** The real part of $\sigma(\omega)$ for $\Delta_0 = 0$ (graphene) and $\Delta_0 = 0.1$ (Kek-O). The diagram on the right shows the allowed transitions contributing to the conductivity. We take $\varepsilon_F = 0.25\,\text{eV}$.

The Fermi contours, defined by the equation $\varepsilon_\eta^\xi(\mathbf{k}) = \varepsilon_F$ determined by the position of ε_F and the size of Δ_0. In this system, there is a single type of interband transition: from the valence band to the conduction band. The critical photon energy required to activate such transitions depends on the Fermi level. When $|\varepsilon_F| < \tilde{\Delta}$, no intraband transitions occur, and the minimum photon energy for interband transitions is $2\tilde{\Delta}$.

The total conductivity has intraband and interband contributions, $\sigma(\omega) = \sigma^{\text{intra}}(\omega) + \sigma^{\text{inter}}(\omega)$. The intraband conductivity, as in gapped graphene [ref], is given by

$$\sigma^{\text{intra}}(\omega) = g_s\sigma_0\frac{\pi}{2}\left[\delta(\hbar\omega) + i\frac{1}{\pi\hbar\omega}\right]\frac{|\varepsilon_F|^2 - (\tilde{\Delta})^2}{|\varepsilon_F|}\Theta(|\varepsilon_F| - \tilde{\Delta}), \tag{5.2.7}$$

The interband contribution has real and imaginary part are given by

$$\mathbb{R}e\{\sigma^{inter}(\omega)\} = g_s g_v \sigma_0 \frac{\pi}{16}\left[1 + \left(\frac{2\tilde{\Delta}}{\hbar\omega}\right)^2\right]\Theta(\hbar\omega - \hbar\omega_c), \tag{5.2.8}$$

$$\mathbb{I}m\{\sigma^{inter}(\omega)\} = g_s g_v \sigma_0 \left\{\frac{\tilde{\Delta}^2}{2\hbar\omega}\frac{1}{\hbar\omega_c} + \frac{1}{16}\left[1 + \left(\frac{2\tilde{\Delta}}{\hbar\omega}\right)^2\right]\ln\left|\frac{\hbar\omega - \hbar\omega_c}{\hbar\omega + \hbar\omega_c}\right|\right\}, \tag{5.2.9}$$

where $\hbar\omega_c = \max\{2\tilde{\Delta}, 2|\varepsilon_F|\}$.

We observe that the optical conductivity of the Kekulé-O model does not differ qualitatively from that of gapped graphene [144]. In particular, the onset of optical absorption occurs at twice the band gap, and the overall frequency dependence resembles that of a conventional massive Dirac system (see Fig. 5.3). This similarity indicates that the Kek-O modulation does not leave a distinct optical signature. Although the Kekulé distortion folds the two Dirac cones to the Γ point, the valley degeneracy remains effectively unbroken, as the cones become indistinguishable in both energy and momentum space. As

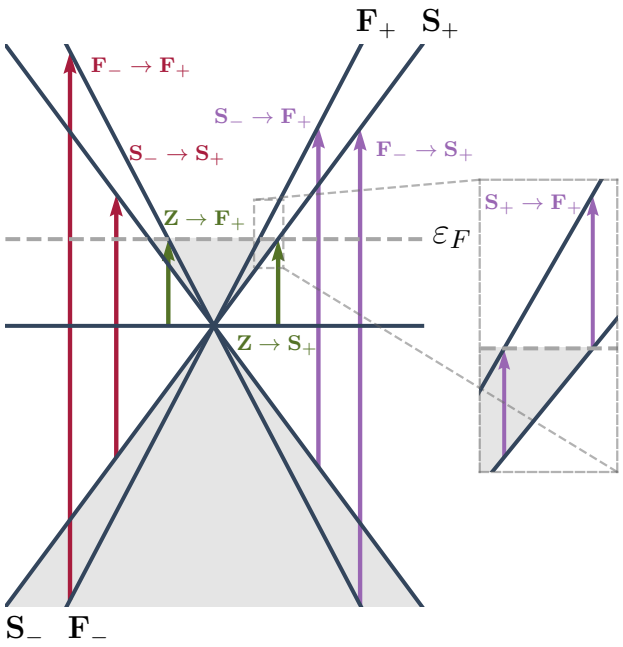

Figure 5.4: Schematic representation of optical interband transitions (arrows) in the double cone structure (blue) of the Kek-α model. They are categorized as intervalley (purple), intravalley (red), and flat-valley (green) transitions. Shaded regions represent filled electron states up to the Fermi energy $\varepsilon_F > 0$ (gray dashed line). The inset shows the available conduction-to-conduction intervalley band transitions opened below ε_F by the folding of the Brillouin zone.

a result, no additional features—such as valley splitting or anisotropic interband transitions—emerge to differentiate the optical response from that of a trivial gap-opening mechanism.

It is worth emphasizing that, to our knowledge, the optical conductivity of the Kekulé-O phase has not been previously calculated or discussed in detail in the literature.

5.3 Kekulé-modulated $\alpha-\mathcal{T}_3$ model

5.3.1 Joint density of states

As a previous step to the calculation of the optical conductivity, we first explore the spectrum of interband transitions through the joint density of states (JDOS), which for transitions $(\xi',\eta')\to(\xi,\eta)$, from the ξ',η' band to the ξ,η at energy $\hbar\omega$ reads as

$$\mathcal{J}^{\xi,\xi'}_{\eta,\eta'}(\omega) = g_s \int' \frac{d^2k}{(2\pi)^2}\,\delta(\varepsilon^{\xi}_{\eta}(\mathbf{k}) - \varepsilon^{\xi'}_{\eta'}(\mathbf{k}) - \hbar\omega)\,, \tag{5.3.1}$$

where $g_s = 2$ is the spin degeneracy. The prime indicates an integration domain restricted to that region of $\mathbf{k}$-space for which $\varepsilon^{\xi'}_{\eta'}(\mathbf{k}) < \varepsilon_F < \varepsilon^{\xi}_{\eta}(\mathbf{k})$ (Pauli blocking), where ε_F is the Fermi energy. Given that $\varepsilon^{\xi}_{\eta}(\mathbf{k}) \propto k$ (see Eq. (5.2.6)), this inequality defines the radii of the wave vectors available for the allowed transition $(\xi', \eta') \to (\xi, \eta)$ at fixed photon energy, $\eta'\hbar v_F(\Delta_\alpha)^{\xi'}k < \varepsilon_F < \eta\hbar v_F(\Delta_\alpha)^{\xi}k$. According to the delta function, with $\omega > 0$, an additional restriction is imposed by energy conservation $\varepsilon^{\xi}_{\eta}(\mathbf{k}) - \varepsilon^{\xi'}_{\eta'}(\mathbf{k}) = \hbar\omega$, which defines a circle with radius $k = \omega/(\eta v_F(\Delta_\alpha)^{\xi} - \eta' v_F(\Delta_\alpha)^{\xi'})$. The combination of these conditions allows to find the critical energies for the interband transitions. It can be anticipated that the JDOS will display the usual linear-in-ω dependence of graphene-like systems.

Three sets of vertical transitions are distinguished in the present model:

(1) *Intravalley* transitions $(\xi, \eta' = -) \to (\xi, \eta = +)$, which we denote as $\mathbf{F}_- \to \mathbf{F}_+$ ($\xi = 1$) and $\mathbf{S}_- \to \mathbf{S}_+$ ($\xi = 0$). They are depicted with red arrows in Fig. **??** for $\varepsilon_F > 0$.

The JDOS of these transitions is

$$\mathcal{J}^{\xi,\xi}_{+,-}(\omega) = \frac{g_s}{8\pi}\frac{\hbar\omega}{(\hbar v_F)^2}\frac{1}{(\Delta_\alpha)^{2\xi}}\,, \quad \hbar\omega > 2|\varepsilon_F|\,. \tag{5.3.2}$$

Note that for the transition between slow cones ($\xi = 0$), $\mathbf{S}_- \to \mathbf{S}_+$ the result is the same as for a single valley of pristine graphene. Also, when $\alpha \to 0$, $\mathcal{J}^{1,1}_{+,-}(\omega) = \mathcal{J}^{0,0}_{+,-}(\omega)$ and the result for graphene is recovered.

(2) *Intervalley* transitions $(\xi, \eta') \to (\bar{\xi}, \eta = +)$ [with $\bar{\xi} = 1 - \xi$] for $\varepsilon_F > 0$ (purple arrows in Fig. **??**), which we refer to as $\{\mathbf{F}_- \to \mathbf{S}_+, \mathbf{S}_- \to \mathbf{F}_+, \mathbf{S}_+ \to \mathbf{F}_+\}$, or transitions $(\xi', \eta' = -) \to (\bar{\xi}', \eta)$ for $\varepsilon_F < 0$, collected in the set $\{\mathbf{S}_- \to \mathbf{F}_+, \mathbf{F}_- \to \mathbf{S}_+, \mathbf{F}_- \to \mathbf{S}_-\}$, both sets are ordered in a decreasing energy onset sequence. The downward transitions $\mathbf{F}_+ \to \mathbf{S}_+$ ($\varepsilon_F > 0$) and $\mathbf{S}_- \to \mathbf{F}_-$ ($\varepsilon_F < 0$), are excluded from the corresponding set. The transition $\mathbf{S}_+ \to \mathbf{F}_+$ is shown in the inset of Fig. 5.4.

The JDOS for the transitions with $\eta' \neq \eta$ reads as

$$\mathcal{J}^{\xi,\bar{\xi}}_{+,-}(\omega) = \frac{g_s}{2\pi}\frac{\hbar\omega}{(\hbar v_F)^2}\frac{1}{(\Delta_\alpha + 1)^2}\,, \quad \hbar\omega > \left(\frac{\Delta_\alpha + 1}{(\Delta_\alpha)^{\xi}}\right)|\varepsilon_F|\,, \tag{5.3.3}$$

while for transitions with $\eta' = \eta$,

$$\mathcal{J}^{1,0}_{+,+}(\omega) = \frac{g_s}{2\pi}\frac{\hbar\omega}{(\hbar v_F)^2}\frac{1}{(\Delta_\alpha - 1)^2}\,, \tag{5.3.4}$$

with

$$\left(\frac{\Delta_\alpha - 1}{\Delta_\alpha}\right)|\varepsilon_F| < \hbar\omega < (\Delta_\alpha - 1)|\varepsilon_F|\,. \tag{5.3.5}$$

The appearance of this window below $|\varepsilon_F|$ is a clear signature of the present hybrid model; as $\alpha \to 0$, it leads to the formation of a singularity, an effect known as band nesting [145, 146]. Later, we will see how this impacts the conductivity and serves as a distinctive feature of Kekulé periodicity.

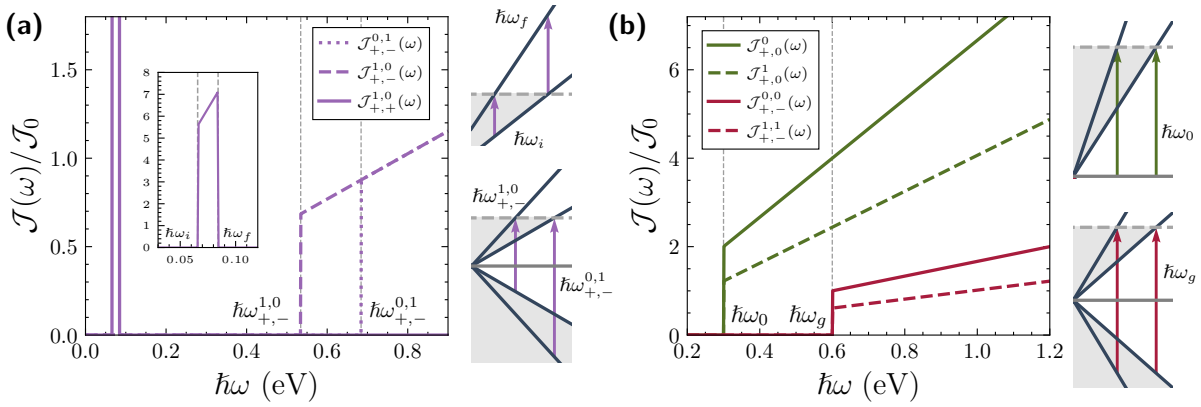

Figure 5.5: Joint density of states for **(a)** intervalley, **(b)** intravalley and flat-valley transitions. The inset in **(a)** shows the contribution of intervalley transitions between bands with the same index η (see inset in Fig. 5.4), which occur in an energy window bounded by critical energies labeled as $\hbar\omega_i$ and $\hbar\omega_f$ (see (5.3.5)). The results are normalized to the JDOS between the two bands of a Dirac point at $\hbar\omega = 2|\varepsilon_F|$, $\mathcal{J}_0 = (g_s/8\pi)(2|\varepsilon_F|/\hbar^2 v_F^2)$. We take $\varepsilon_F = 0.3$ eV and $\alpha = 0.4$.

(3) *Flat-valley* transitions $(\xi', \eta' = 0) \to (\xi, \eta = +)$ $(\varepsilon_F > 0)$ or $(\xi', \eta' = -) \to (\xi, \eta = 0)$ $(\varepsilon_F < 0)$, denoted as $\{\mathbf{Z}^{\xi'} \to \mathbf{F}_+,\ \mathbf{Z}^{\xi'} \to \mathbf{S}_+\}$ (green arrows in Fig. **??**) or $\{\mathbf{F}_- \to \mathbf{Z}^{\xi},\ \mathbf{S}_- \to \mathbf{Z}^{\xi}\}$, respectively. For the former set, Eq. (5.3.1) with $\varepsilon^{\xi'}_{\eta'} = 0$, gives

$$\mathcal{J}^{\xi}_{+,0}(\omega) = \frac{g_s}{2\pi}\frac{\hbar\omega}{(\hbar v_F)^2}\frac{1}{(\Delta_\alpha)^{2\xi}}\,, \quad \hbar\omega > |\varepsilon_F|\,. \tag{5.3.6}$$

For the latter set, taking $\varepsilon^{\xi}_{\eta} = 0$ in (5.3.1), $\mathcal{J}^{\xi'}_{0,-}(\omega) = \mathcal{J}^{\xi'}_{+,0}(\omega)$.

Figure 5.5 displays the JDOS for the complete set of interband transitions of the present model. The corresponding onsets in Eqs. (5.3.2)-(5.3.6) have been labeled according to the definition

$$\hbar\omega^{\xi,\xi'}_{\eta,\eta'} = (\eta - \eta'(\Delta_\alpha)^{\xi'-\xi})|\varepsilon_F|\,. \tag{5.3.7}$$

Thus, $\hbar\omega_g \equiv \hbar\omega^{1,1}_{+,-} = \hbar\omega^{0,0}_{+,-} = 2|\varepsilon_F|$ corresponds to the onset for the intravalley transitions, while $\hbar\omega^{0,1}_{+,-} = (\Delta_\alpha + 1)|\varepsilon_F|$, $\hbar\omega^{1,0}_{+,-} = (\Delta_\alpha + 1)|\varepsilon_F|/\Delta_\alpha$ (see (5.3.3)), and $\hbar\omega^{1,0}_{+,+} = (\Delta_\alpha - 1)|\varepsilon_F|/\Delta_\alpha \equiv \hbar\omega_i$, $\Delta_\alpha\hbar\omega^{1,0}_{+,+} = (\Delta_\alpha - 1)|\varepsilon_F| \equiv \hbar\omega_f$ (see (5.3.5)), to the intervalley transitions. The corresponding energy onset for the flat-valley transitions are labeled as $\hbar\omega_0 \equiv \hbar\omega^{\xi,\xi'}_{+,0} = \hbar\omega^{\xi',\xi'}_{0,-} = |\varepsilon_F|$.

It can be seen how for transitions sharing the onset, the α-dependent slope provides a way to identify its nature. It is worthwhile to note also that for a decreasing magnitude of the parameter α, the number of transitions between cones with the same band index, $\mathbf{S}_+ \to \mathbf{F}_+$ or $\mathbf{F}_- \to \mathbf{S}_-$, notably increase because $\mathcal{J}^{+,-}_{+,+}(\omega) \propto (\Delta_\alpha - 1)^{-2}$, although the frequency region (5.3.5) narrows.

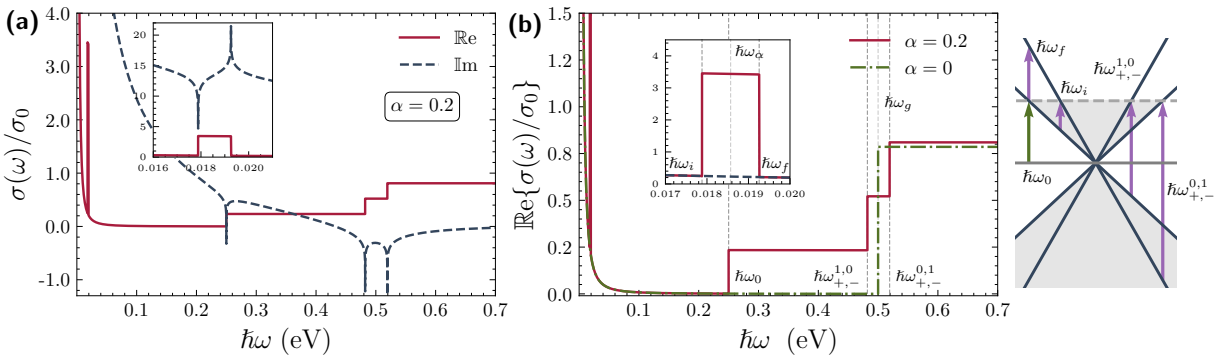

Figure 5.6: **(a)** Real and imaginary parts of the optical conductivity $\sigma(\omega)$ for the Kek-α model. The inset shows the absorption window due to $\mathbb{R}\mathrm{e}\{\sigma_\alpha^{\mathrm{inter}}(\omega)\}$ (Eq. (5.3.12)) and the corresponding singularities in $\mathbb{I}\mathrm{m}\{\sigma_\alpha^{\mathrm{inter}}(\omega)\}$. **(b)** The real part of $\sigma(\omega)$ for $\alpha = 0$ (graphene) and $\alpha = 0.2$ (Kek-α). The modulated central atom increases and splits the interband conductivity into three steps, and introduces and additional box-shaped energy window for optical absorption well below the Fermi energy, due to conduction-to-conduction intervalley transitions. The diagram on the right shows the allowed transitions contributing to the conductivity. We take $\varepsilon_F = 0.25\,\mathrm{eV}$.

5.3.2 Optical conductivity

The total conductivity has intraband and interband contributions, $\sigma(\omega) = \sigma^{\mathrm{intra}}(\omega) + \sigma^{\mathrm{inter}}(\omega)$. The intraband conductivity, as in pristine graphene [64, 131, 142, 147], is given by

$$\sigma^{\mathrm{intra}}(\omega) = g_s\sigma_0\frac{\pi}{2}\left[\delta(\hbar\omega) + i\frac{1}{\pi\hbar\omega}\right]|\varepsilon_F|, \tag{5.3.8}$$

where each cone contributed independently and the flat band did not, since it has uniformly zero group velocity.

We divide the interband contribution as

$$\sigma^{\mathrm{inter}}(\omega) = \sigma^{\mathrm{inter}}_{>}(\omega)\Theta(\hbar\omega - |\varepsilon_F|) + \sigma^{\mathrm{inter}}_{<}(\omega)\Theta(|\varepsilon_F| - \hbar\omega), \tag{5.3.9}$$

where $\sigma^{\mathrm{inter}}_{>}(\omega)$ considers contributions above the Fermi energy, that is the sum of all permitted interband transitions, excluding $\mathbf{S}_+ \to \mathbf{F}_+$ (or $\mathbf{F}_- \to \mathbf{S}_-$ when $\varepsilon_F < 0$), therefore

$$\sigma^{\mathrm{inter}}_{>}(\omega) = [\sigma^{\mathrm{inter}}_{>}(\omega)]^{0,1}_{+,0} + [\sigma^{\mathrm{inter}}_{>}(\omega)]^{1,0}_{+,-} + [\sigma^{\mathrm{inter}}_{>}(\omega)]^{0,1}_{+,-}, \tag{5.3.10}$$

with each transition contribution given by,

$$\left[\sigma^{\mathrm{inter}}_{>}(\omega)\right]^{\xi,\xi'}_{\eta,\eta'} = g_s\sigma_0\frac{\pi}{4\hbar^2 v_F^2}\frac{\mathcal{V}^{\xi,\xi'}_{\eta,\eta'}}{(\eta(\Delta_\alpha)^\xi - \eta'(\Delta_\alpha)^{\xi'})^2}\times$$
$$\times\left\{\Theta(\hbar\omega - \hbar\omega^{\xi,\xi'}_{\eta,\eta'}) - \frac{i}{\pi}\ln\left[\frac{|\hbar\omega + \hbar\omega^{\xi,\xi'}_{\eta,\eta'}|}{|\hbar\omega - \hbar\omega^{\xi,\xi'}_{\eta,\eta'}|}\right]\right\}. \tag{5.3.11}$$

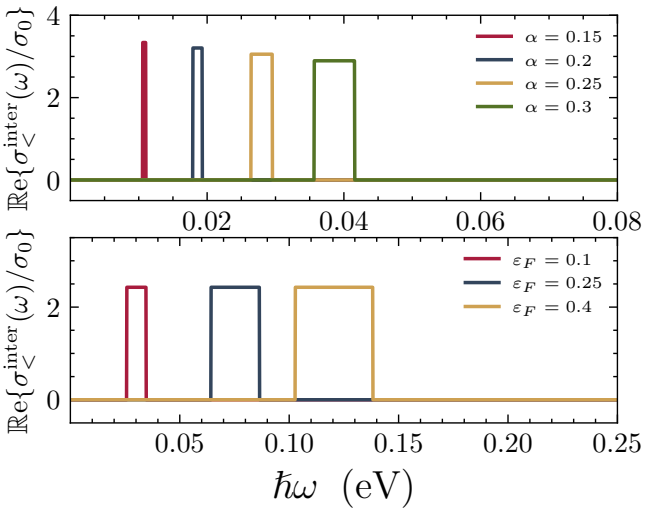

Figure 5.7: Top: $\mathbb{R}\mathrm{e}\{\sigma_<^{\mathrm{inter}}(\omega)\}$ for several values of α at fixed $\varepsilon_F = 0.25\,\mathrm{eV}$. The absorption window displays a red shift and narrows as parameter α decreases, with its magnitude increasing (see Eq. (5.3.12)). Bottom: $\mathbb{R}\mathrm{e}\{\sigma_<^{\mathrm{inter}}\}$ for varying ε_F with fixed value of $\alpha = 0.45$. A red shift and a narrowing of the spectrum is observed as ε_F diminish, but now its magnitude remains constant.

where we have defined the dimensionless coefficients $\mathcal{V}_{\eta,\eta'}^{\xi,\xi'}$, defined for allowed interband transitions, we have $[\eta\eta'(4\alpha^2-1)+\Delta_\alpha]^2/4\Delta_\alpha^2$ for intervalley transitions, $4\alpha^2/(2\alpha^2+1)$ for the transition $\mathbf{Z}^1 \to \mathbf{S}_+$ (or $\mathbf{S}_- \to \mathbf{Z}^1$) and zero otherwise.

On the other hand, $\sigma_<^{\mathrm{inter}}(\omega)$ considers contributions below the Fermi energy, that is, the intervalley transitions $\mathbf{S}_+ \to \mathbf{F}_+$ and $\mathbf{F}_- \to \mathbf{S}_-$, then

$$\sigma_<^{\mathrm{inter}}(\omega) = g_s \frac{\sigma_0 \pi}{4\hbar^2 v_F^2} \frac{\mathcal{V}_{+,+}^{1,0}}{(\Delta_\alpha - 1)^2} \left\{ \Theta(\hbar\omega - \hbar\omega_i)\Theta\left(\hbar\omega_f - \hbar\omega\right) + \right.$$
$$\left. + \frac{i}{\pi} \ln \left| \frac{\hbar\omega - \hbar\omega_f}{\hbar\omega + \hbar\omega_f} \cdot \frac{\hbar\omega + \hbar\omega_i}{\hbar\omega - \hbar\omega_i} \right| \right\}. \tag{5.3.12}$$

Intravalley transitions ($\mathbf{S}_- \to \mathbf{S}_+$ and $\mathbf{F}_- \to \mathbf{F}_+$) in the Kek-Y graphene model were previously shown to be forbidden using Fermi's golden rule [58]. This can be attributed to the fact that the **S** cone is entirely chiral, while the **F** cone is entirely antichiral. A more formal verification was provided using symmetry arguments, which impose a selection rule in the context of the Zitterbewegung effect [60]. In addition, we find that the transitions $\mathbf{Z}^\xi \to \mathbf{F}_+$, between a flat band and the fast cone are absent, reducing the number of transitions with the flat band, compared to the α-$\mathcal{T}_3$ model.

The real and imaginary parts of the total optical conductivity $\sigma(\omega)$, for $\varepsilon_F = 0.25$ eV, are shown in Fig. 6(a), in Fig. 6(b) we compare the real part of the conductivity for $\alpha = 0$ (graphene) and $\alpha = 0.4$. Compared with the usual optical response of graphene, these plots show three distinctive features: an intervalley window for transitions below the Fermi energy (see the inset in Fig. 6(a)), a flat band to slow cone step at $\hbar\omega = \varepsilon_F$

and the splitting of the step at $\hbar\omega = 2\varepsilon_F$ in two steps, one at $\hbar\omega_{+,-}^{0,1} = (\Delta_\alpha + 1)|\varepsilon_F|$, and the other at $\hbar\omega_{+,-}^{1,0} = (\Delta_\alpha + 1)|\varepsilon_F|/\Delta_\alpha$. Notably, the addition of the central atom results in increased maximum absorption compared to that of other graphene-like systems, with this distinct three-step structure in the optical conductivity [58, 59]. This effect, along with the modified energy dispersion, resembles the behavior of a 5/2-pseudospin Dirac semimetal [148], suggesting that lattice modulation may alter the system's effective pseudospin.

When $\alpha \to 0$, the $\sigma_<^{\text{inter}}(\omega)$ contribution and the flat-band term in Eq. (5.3.11) vanish, reducing the interband conductivity to the well-known expression for pristine graphene's interband conductivity [131], $\sigma^{\text{inter}}(\omega) = \sigma_{\text{gr}}^{\text{inter}}(\omega)$, where

$$\sigma_{\text{gr}}^{\text{inter}}(\omega) = g_s \frac{\sigma_0 \pi}{16} \left\{ \Theta(\hbar\omega - 2|\varepsilon_F|) - \frac{i}{\pi} \ln \left| \frac{\hbar\omega + 2|\varepsilon_F|}{\hbar\omega - 2|\varepsilon_F|} \right| \right\}. \tag{5.3.13}$$

We further analyze the interband contributions below the Fermi energy $\sigma_<^{\text{inter}}(\omega)$ in Fig. 5.7. The frequency range of this conductivity is determined by $\hbar\omega_{fi} = \hbar(\omega_f - \omega_i) = (\Delta_\alpha - 1)^2|\varepsilon_F|/\Delta_\alpha$, and it is centered at $\hbar\omega_< = \hbar(\omega_i + \omega_f)/2 = (\Delta_\alpha^2 - 1)|\varepsilon_F|/(2\Delta_\alpha)$, as shown in the inset of Fig. 6(b). Notice that $\omega_< = (\omega_{+,-}^{0,1} - \omega_{+,-}^{1,0})/2$, i.e. $\omega_<$ is related with the frequency difference of the transitions $\mathbf{S}_- \to \mathbf{F}_+$ and $\mathbf{F}_- \to \mathbf{S}_+$. The energy $\hbar\omega_<$ is often referred to as the beat frequency [59] and is the result of interference between the two closely spaced critical frequencies. For $\alpha \to 0$, the contribution $\sigma_<^{\text{inter}}(\omega)$ vanishes, as the band $\varepsilon_+^+(\mathbf{k})$ and $\varepsilon_+^-(\mathbf{k})$ nearly overlap, resulting in $\nabla_{\mathbf{k}}[\varepsilon_+^+(\mathbf{k}) - \varepsilon_+^-(\mathbf{k})] \approx 0$ and resulting in an absorption peak in conductivity. This effect, known as band nesting, has also been observed in transition metal dichalcogenides [145, 146] and space-modulated 2D materials, such as twisted bilayer graphene [73, 149, 150].

5.4 Effects of finite temperature on optical conductivity

In realistic conditions, temperature plays a crucial role in the optical response of materials. Thermal effects can smear spectral features and modify absorption profiles in Dirac systems [58, 131, 141, 151]. Conceptually, this occurs because finite temperature introduces a thermal distribution of carriers around the Fermi level, effectively averaging the optical response over a range of energies. As a result, sharp transitions at zero temperature broadened, and the conductivity becomes a thermally weighted version of its zero-temperature counterpart.

The conductivity at finite temperature can be calculated from a convolution integral between the zero-temperature counterpart, $\sigma(\omega; T, \mu')$, and the peaked function, $\partial f/\partial\mu'$, with $f[\mu(T), \mu'] = (\exp\{\beta[\mu(T) - \mu']\} + 1)^{-1}$, which takes the form [152]:

$$\sigma[\omega; T, \mu(T)] = \frac{\beta}{4} \int_{-\infty}^{\infty} \frac{\sigma(\omega; 0, \mu')}{\cosh^2\{\beta[\mu(T) - \mu']/2\}} \, d\mu' \tag{5.4.1}$$

where μ' is the Fermi energy $\varepsilon_F = \mu(T = 0)$ and $\beta = 1/k_B T$.

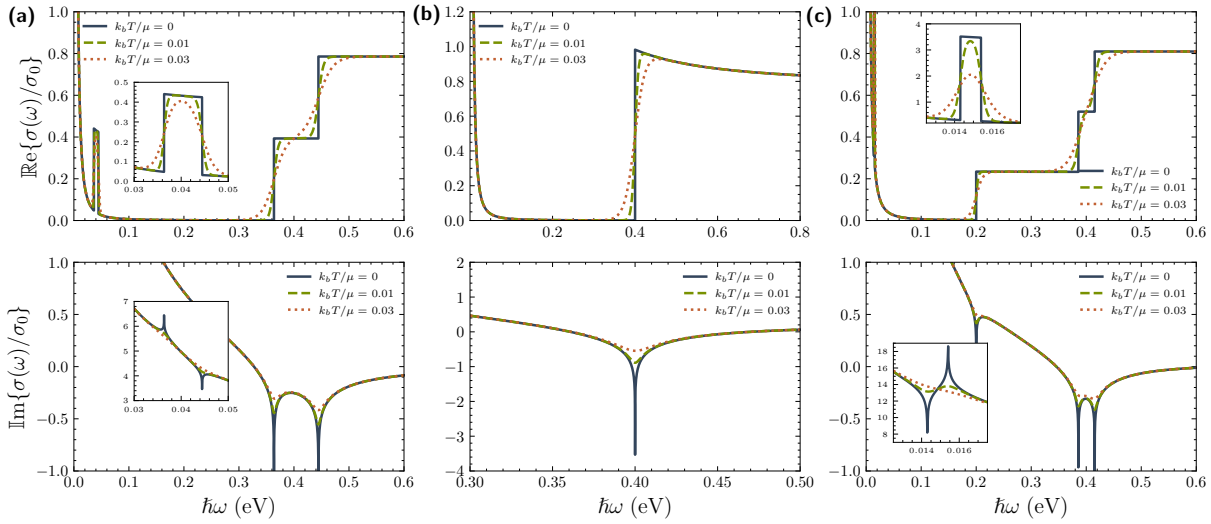

Figure 5.8: Real and imaginary parts of the optical conductivity considering the effect of finite temperature for the **(a)** Kek-Y, **(b)** Kek-O, and **(c)** Kek-α models. We take $\mu = 0.2$ eV, with $\tilde{\Delta} = 0.1$ for the Kek-Y and Kek-O models, and $\alpha = 0.2$ for the Kek-α model.

To obtain finite-temperature expressions for the three models under consideration, we find that the essential components of the conductivity are modified as follows:

$$|\varepsilon_F| \quad \rightarrow \quad 2k_BT\ln[2\cosh(\beta\mu/2)] \tag{5.4.2}$$

$$\Theta(\hbar\omega-\hbar\omega_\mu) \quad \rightarrow \quad \frac{1}{2}\left\{\tanh\left[\frac{\beta\mu}{2\hbar\omega_\mu}(\hbar\omega+\hbar\omega_\mu)\right]+\tanh\left[\frac{\beta\mu}{2\hbar\omega_\mu}(\hbar\omega-\hbar\omega_\mu)\right]\right\} \tag{5.4.3}$$

$$\begin{aligned}\Theta(\hbar\omega-\hbar\omega_\mu)\Theta(\hbar\omega'_\mu-\hbar\omega) \quad \rightarrow \quad & \frac{1}{2}\left\{\tanh\left[\frac{\beta\mu}{2\hbar\omega_\mu}(\hbar\omega+\hbar\omega_\mu)\right]+\right.\\ & \left.+\tanh\left[\frac{\beta\mu}{2\hbar\omega_\mu}(\hbar\omega-\hbar\omega_\mu)\right]-(\hbar\omega_\mu\rightarrow\hbar\omega'_\mu)\right\}\end{aligned} \tag{5.4.4}$$

$$|\hbar\omega\pm\hbar\omega_\mu| \quad \rightarrow \quad \sqrt{(\hbar\omega\pm\hbar\omega_\mu)^2+\left[\hbar\omega_\mu(k_BT)^2/\mu\right]} \tag{5.4.5}$$

Here, ω_μ is the critical frequency associated with interband transitions (e.g., for graphene, $\omega_\mu = 2\mu/\hbar$). The Eq. (5.4.2) corresponds to the intraband contribution, the Eqs. (5.4.3) modifies the real part of the interband response, and the Eq. (5.4.5) smooths the logarithmic divergence in the imaginary part of the interband conductivity.

In particular, for the imaginary part of the interband contribution, evaluating the convolution integral in Eq. (5.4.1) is generally not analytically tractable. However, a thermal regularization can be introduced to approximate the result [131], effectively smoothing the singularity, as shown in Eq. (5.4.5). This approach is accurate at low temperatures. At higher temperatures, however, a full numerical evaluation of the convolution integral is required for reliable results.

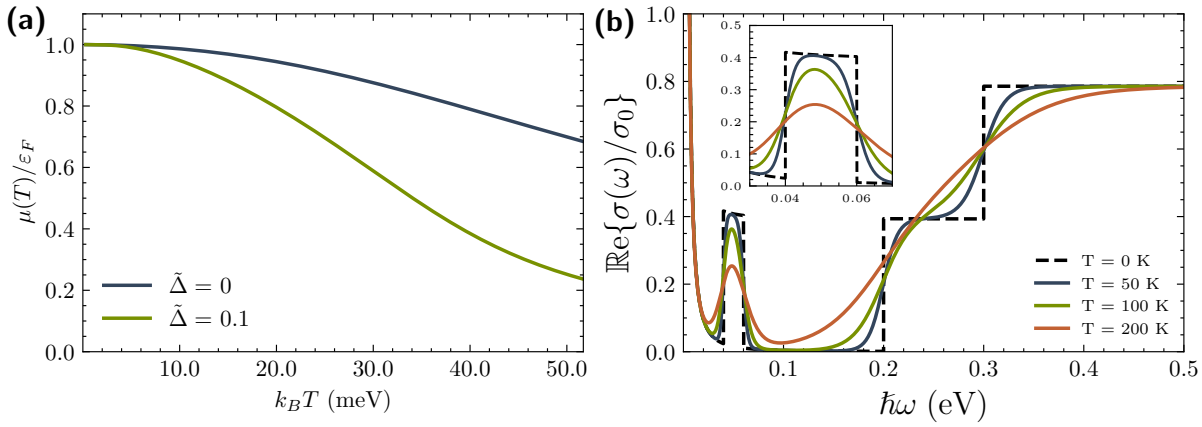

Figure 5.9: (a) Temperature-dependent chemical potential $\mu(T)$ for different values of the effective gap $\tilde{\Delta}$, with a fixed Fermi energy $\varepsilon_F = 110$ meV. **(b)** Real part of the optical conductivity of the Kek-Y model at different temperatures, computed for $\varepsilon_F = 120$ meV and $\Delta_0 = 100$ meV.

An accurate description of temperature effects in Dirac systems also requires determining the temperature-dependent chemical potential $\mu(T)$, which ensures carrier density conservation. This is particularly important when calculating optical properties at finite temperature. The resulting implicit equation, expressed in terms of the Fermi energy $\varepsilon_F = \mu(0)$, takes the form [151]:

$$\varepsilon_F^2 - \tilde{\Delta}^2 = 2(k_B T)^2 \Lambda[T, \mu(T), \tilde{\Delta}], \tag{5.4.6}$$

where

$$\Lambda[T, \mu(T), \tilde{\Delta}] = \beta\tilde{\Delta} \ln\left(\frac{1 + e^{\beta(\mu-\tilde{\Delta})}}{1 + e^{-\beta(\mu+\tilde{\Delta})}}\right) + \mathrm{Li}_2\left(-e^{-\beta(\mu+\tilde{\Delta})}\right) - \mathrm{Li}_2\left(-e^{\beta(\mu-\tilde{\Delta})}\right), \tag{5.4.7}$$

$\mathrm{Li}_2(x)$ is the dilogarithm function, and $\tilde{\Delta}$ denotes the effective energy gap. Note that in Eq.(5.4.6), only the Kek-O model corresponds to $\tilde{\Delta} \neq 0$, while for the Kek-Y and Kek-α models, $\tilde{\Delta} = 0$.

In Fig. 5.9, we present the corresponding chemical potentials $\mu(T)$ at a fixed positive value of ε_F. The function $\mu(T)$ remains positive in both cases. In the presence of a gap leads to a more rapid decrease of $\mu(T)$ as a function of temperature compared to the simplest case of gapless.

5.5 Optical signature of Kekulé periodicity

The Kek-Y and Kek-α models exhibit a characteristic absorption window in the low-frequency optical response (see Fig. 5.7), which is absent in the Kek-O model. This absorption feature originates from the breaking of valley degeneracy due to the Kekulé

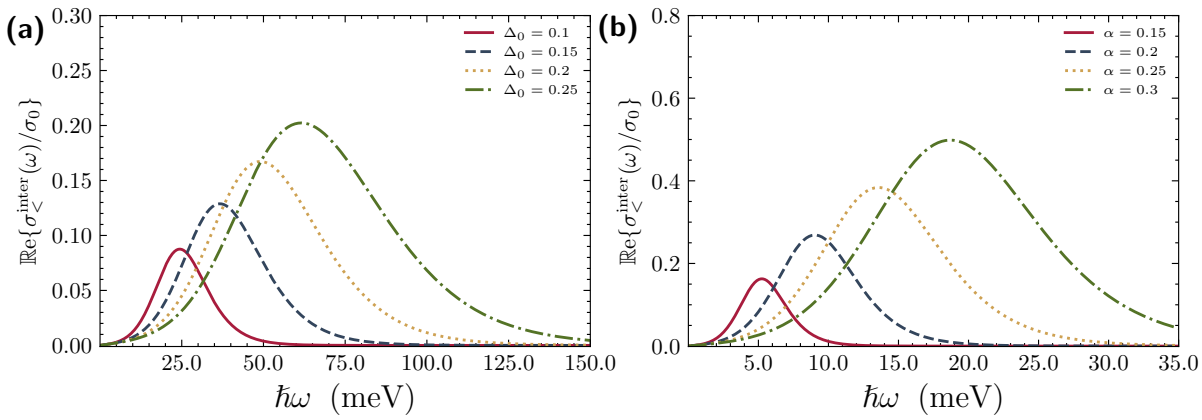

Figure 5.10: Interband contribution to the optical conductivity below the Fermi energy, $\mathbb{R}\mathrm{e}\{\sigma_<^{\mathrm{inter}}(\omega)\}$, for **(a)** the Kek-Y model and **(b)** the Kek-α model, for different values of Δ_0 and α, respectively. The calculations are performed at $T = 298$ K and $\varepsilon_F = 120$ meV.

periodicity. In contrast to pristine graphene, where inter-valley transitions are forbidden, the folding of the Brillouin zone in Kekulé-modulated systems enables optical transitions between states in different valleys.

This phenomenon leads to the interband transitions below the Fermi energy, a hallmark of Kekulé-modulated structures with gapless spectra. In both the Kek-Y and Kek-α models, this contribution is associated with the $\mathbf{S}^+ \to \mathbf{F}^+$ intervalley transition, as shown in Fig. 5.2 and Fig. 5.6. The folding of the Brillouin zone causes certain conduction bands to become nearly parallel, specifically $\varepsilon_+^+(\mathbf{k})$ and $\varepsilon_+^-(\mathbf{k})$. This implies that their energy difference has a small group velocity $\nabla_{\mathbf{k}}[\varepsilon_+^+(\mathbf{k}) - \varepsilon_+^-(\mathbf{k})] \approx 0$, which leads to an enhancement in optical absorption, this is known as band nesting [63]. We notice that the intraband contribution remains unchanged across all Kekulé models. The Kekulé modulation does not affect transport within the same valley, meaning the Dirac cone structure remains intact.

We present the optical response at finite temperature in Fig. 5.10. We observe that the absorption feature extends into the infrared regime. In the Kek-α model, the spectrum at small values of α lies in the far-infrared, whereas in the Kek-Y model, it lies in the mid-infrared range. In both cases, the absorption strength is tunable via the Kekulé parameter: Δ_0 for Kek-Y and α for Kek-α.

Moreover, in both models, the absorption magnitude is proportional to the strength of the Kekulé modulation, i.e., to Δ_0 or α. Notably, the Kek-α model exhibits a larger absorption magnitude than the Kek-Y case. Furthermore, at zero temperature, the absorption appears as a well-defined window. At finite temperature, thermal broadening smooths the optical response, transforming the window into a well-defined peak, as shown in Fig 5.11. This effect is particularly noticeable in the Kek-α model, where the magnitude of the peak becomes directly proportional to α (see Fig. 5.10) in contrast to the zero-temperature where the opposite occurs (see Fig. 5.7).

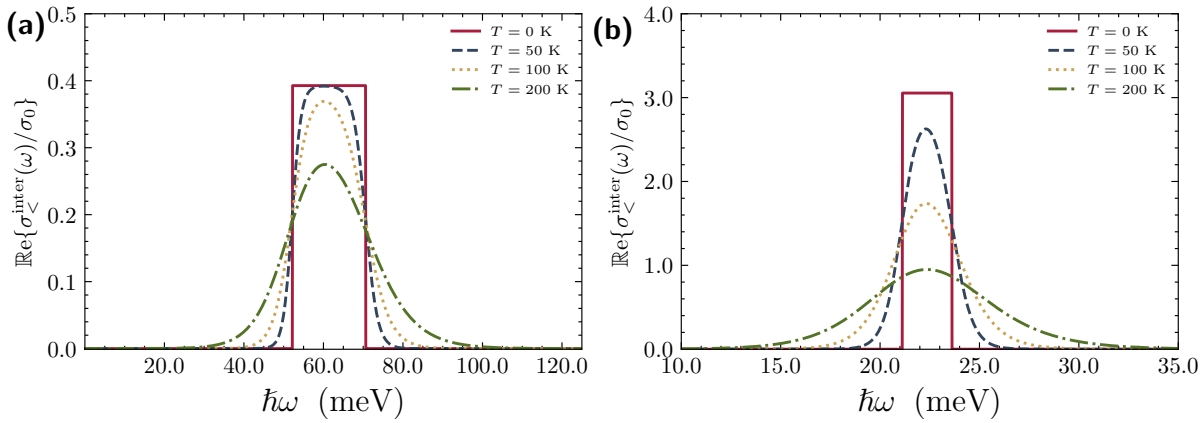

Figure 5.11: Interband contribution to the optical conductivity below the Fermi energy, $\mathbb{R}\mathrm{e}\{\sigma^{\mathrm{inter}}_{<}(\omega)\}$, for **(a)** the Kek-Y model and **(b)** the Kek-α model at different temperatures. We consider $\varepsilon_F = 200$ meV, with $\Delta_0 = 0.15$ for the Kek-Y model and $\alpha = 0.25$ for the Kek-α model.

We identify a pronounced resonance peak at the center of the spectrum, referred to as the Kekulé frequency, given by:

$$\omega_{\mathrm{Kek}} = \frac{\omega_+ - \omega_-}{2} = \begin{cases} \dfrac{2\Delta_0}{1-\Delta_0^2}\dfrac{|\mu|}{\hbar} & \text{for Kek-Y,} \\ \dfrac{(\Delta_\alpha^2 - 1)}{2\Delta_\alpha}\dfrac{|\mu|}{\hbar} & \text{for Kek-}\alpha, \end{cases} \tag{5.5.1}$$

where ω_+ and ω_- correspond to the transition frequencies $\mathbf{F}_- \to \mathbf{S}_+$ and $\mathbf{S}_- \to \mathbf{F}_+$, respectively.

This resonance is interpreted as a beat frequency, arising from the interference of two absorption channels with closely spaced frequencies. Such interference results in an observable peak in the conductivity spectrum [59]. The Kekulé periodicity lifts the valley degeneracy, introducing two closely spaced absorption edges for each valley. The interference between these two gives rise to the resonant Kekulé frequency, ω_{Kek}.

Finally, this phenomenon is particularly relevant in the context of space-modulated 2D materials, such as twisted bilayer graphene [73, 149, 150], and we expect that might serve as a fingerprint of Kekulé modulation in similar systems [58, 59, 63, 101].

6

Conclusions

This work has explored the electronic and optical properties of two-dimensional Dirac materials with Kekulé modulation, focusing on three distinct Kekulé phases: Kek-Y, Kek-O, and Kek-α.

Chapter 2 presented a review of the electronic structure of key Dirac materials, including pristine graphene, Kekulé-distorted graphene and the α-$\mathcal{T}_3$ model. These systems served as the foundation for understanding their characteristic low-energy behavior.

Building upon this background, in Chapter 4 we introduced a Kekulé modulation into the α-$\mathcal{T}_3$ model, resulting in a novel hybrid system: the Kekulé-modulated α-$\mathcal{T}_3$ model (Kek-α). We calculated the band structure and corresponding eigenfunctions. The model features a double-cone energy dispersion and a degenerate flat band, closely resembling the spectrum of the Kek-Y model. Additionally, we briefly explored the effects of a perpendicular electric field by introducing asymmetric on-site energies. This perturbation opens an energy gap and induces a curvature in the flat band, making it weakly dispersive. A similar behavior has been reported in the irradiated α-$\mathcal{T}_3$ model under circularly polarized light [140], though the underlying mechanisms differ. In our case, the full understanding of this effect remains an open problem that requires further investigation. Another interesting direction for future work is the inclusion of spin-orbit coupling. Given that the considered lattice exhibits buckling, the intrinsic spin-orbit interaction could be significant and may lead to nontrivial topological phases.

To characterize the quantum transport properties of these systems, we studied their optical response. Chapter 3 established the theoretical framework by introducing linear response theory and the Kubo formalism, including a detailed derivation of graphene's optical conductivity as a benchmark. In Chapter 5 , we applied this framework to compute the optical conductivity of Kek-Y, Kek-O, and Kek-α.

The optical response of the Kek-Y model has been reported in earlier works [56, 58]; however, our analysis extends and refines its characterization. Both the Kek-Y and Kek-α models exhibit highly tunable optical response governed by the Kekulé parameters Δ_0

and α, respectively. Notably, new features emerge in their conductivity spectra due to the opening of intervalley channels, which are absent in pristine graphene and the α-$\mathcal{T}_3$ model. In contrast, the Kek-O phase optical spectrum does not differ qualitatively from that of gapped graphene, without prominent signatures of Kekulé periodicity. Interestingly, it has been shown that the Kek-Y model mimics the behavior of a pseudospin-3/2 Dirac system. In our study, the Kek-α phase revealed an optical conductivity with a distinct three-step structure, reminiscent of a pseudospin-5/2 Dirac semimetal. For all three phases, our analytical results recover the well-known expressions for pristine graphene in the appropriate low-energy limits.

We also studied the effects of finite temperature on the optical conductivity. By using the standard convolution method, we obtained the finite-temperature response from the zero-temperature conductivity. The results showed that thermal broadening primarily smooths the spectral features around the critical frequencies, due to the broadening of the Fermi-Dirac distribution. We computed and analyzed the temperature dependence of the conductivity for all three phases. Finally, we identified an absorption resonance in the Kek-Y and Kek-α models, associated with a beat frequency between the valleys. This peak emerges in the optical conductivity at finite temperature and serves as a signature of intervalley coupling. We analyzed how the peak position and intensity depend on the Kekulé parameters and temperature, and identified the characteristic frequency at which this resonance occurs.

In summary, the study of the electronic and optical properties of Kekulé-modulated Dirac systems reveals key features of valley coupling and symmetry breaking, which may serve as robust optical signatures for detecting Kekulé periodicity in related two-dimensional materials.

A

Detailed tight-binding model of the Kekulé-distorted graphene

We start from the tight-binding Hamiltonian of graphene with Kekulé bond modulation:

$$H = -\sum_{\mathbf{r}}\sum_{n=1}^{3} t_{\mathbf{r},n} a_{\mathbf{r}}^{\dagger} b_{\mathbf{r}+\boldsymbol{\delta}_n} + \text{H.c.} \tag{A.0.1}$$

where the bond-density wave is introduced as $t_{\mathbf{r},n} = t\{1 + 2\mathbb{R}\text{e}[\tilde{\Delta} e^{i(p\mathbf{K}_+ + q\mathbf{K}_-)\cdot\boldsymbol{\delta}_n + i\mathbf{G}\cdot\mathbf{r}}]\}$. with Kekulé wavevector $\mathbf{G} = \mathbf{K}_+ - \mathbf{K}_-$ and $\tilde{\Delta}$ the complex Kekulé parameter. The Hamiltonian can be split into two parts:

$$\begin{aligned} H &= -t\sum_{\mathbf{r}}\sum_{n=1}^{3} a_{\mathbf{r}}^{\dagger} b_{\mathbf{r}+\boldsymbol{\delta}_i} - 2t\sum_{\mathbf{r}}\sum_{n=1}^{3} \mathbb{R}\text{e}\{\tilde{\Delta} e^{i(p\mathbf{K}_+ + q\mathbf{K}_-)\cdot\boldsymbol{\delta}_n + i\mathbf{G}\cdot\mathbf{r}}\} a_{\mathbf{r}}^{\dagger} b_{\mathbf{r}+\boldsymbol{\delta}_n} + \text{H.c.}, \\ &= H_0 + H_K \end{aligned} \tag{A.0.2}$$

where H_0 corresponds to pristine graphene and H_K captures the Kekulé perturbation. To transform H_K to momentum space, we define $\alpha = (p\mathbf{K}_+ + q\mathbf{K}_-)\cdot\boldsymbol{\delta}_n$ and $\beta = \mathbf{G}\cdot\mathbf{r}$, and proceed with the Fourier transform:

$$\begin{aligned} H_K &= -t\sum_{\mathbf{r}}\sum_{n=1}^{3}[\tilde{\Delta} e^{i\alpha+i\beta} + \tilde{\Delta}^* e^{-i\alpha-i\beta}] a_{\mathbf{r}}^{\dagger} b_{\mathbf{r}+\boldsymbol{\delta}_n} + \text{H.c.}, \\ &= -\frac{t}{N}\sum_{\mathbf{k},\mathbf{k}'}\sum_{\mathbf{r}}\sum_{n=1}^{3}[\tilde{\Delta} e^{i\alpha+i\beta} + \tilde{\Delta}^* e^{-i\alpha-i\beta}] a_{\mathbf{k}}^{\dagger} e^{i(\mathbf{k}'-\mathbf{k})\cdot\mathbf{r}} e^{i\mathbf{k}'\cdot\boldsymbol{\delta}_n} b_{\mathbf{k}'} + \text{H.c.}, \\ &= -\frac{t}{N}\sum_{\mathbf{k},\mathbf{k}'}\sum_{\mathbf{r}}\sum_{n=1}^{3}\left[\tilde{\Delta} a_{\mathbf{k}}^{\dagger} e^{-i[\mathbf{k}-(\mathbf{k}'+\mathbf{G})]\cdot\mathbf{r}} e^{i(\mathbf{k}'+\mathbf{K}_{p,q})\cdot\boldsymbol{\delta}_n} b_{\mathbf{k}'} + \tilde{\Delta}^* a_{\mathbf{k}}^{\dagger} e^{-i[\mathbf{k}-(\mathbf{k}'-\mathbf{G})]\cdot\mathbf{r}} e^{i(\mathbf{k}'-\mathbf{K}_{p,q})\cdot\boldsymbol{\delta}_n} b_{\mathbf{k}'}\right] + \text{H.c.}, \end{aligned} \tag{A.0.3}$$

where we have used $\mathbf{K}_{p,q} = (p\mathbf{K}_+ + q\mathbf{K}_-)$. After summing over real space, we obtain momentum-conserving delta functions and the result:

$$H_K = -t\sum_{\mathbf{k}'}\sum_{n=1}^{3}\left[\tilde{\Delta}a^\dagger_{\mathbf{k}'+\mathbf{G}}e^{i(\mathbf{k}'+\mathbf{K}_{p,q})\cdot\boldsymbol{\delta}_n}b_{\mathbf{k}'} + \tilde{\Delta}^* a^\dagger_{\mathbf{k}'-\mathbf{G}}e^{i(\mathbf{k}'-\mathbf{K}_{p,q})\cdot\boldsymbol{\delta}_n}b_{\mathbf{k}'}\right] + \text{H.c.} \tag{A.0.4}$$

Using the definition of the structure factor for nearest-neighbor hopping $f(\mathbf{k}) = \sum_n e^{i\mathbf{k}\cdot\boldsymbol{\delta}_n}$. The full Hamiltonian in momentum space becomes:

$$\begin{aligned} H = &-\sum_{\mathbf{k}} a^\dagger_{\mathbf{k}} f(\mathbf{k}) b_{\mathbf{k}} - a^\dagger_{\mathbf{k}+\mathbf{G}}\tilde{\Delta} f(\mathbf{k}+p\mathbf{K}_+ + q\mathbf{K}_-)b_{\mathbf{k}} \\ &- a^\dagger_{\mathbf{k}-\mathbf{G}}\tilde{\Delta}^* f(\mathbf{k}-p\mathbf{K}_+ - q\mathbf{K}_-)b_{\mathbf{k}} + \text{H.c.}. \end{aligned} \tag{A.0.5}$$

We can expand the Hamiltonian by shifting each term by $+\mathbf{G}$ and $-\mathbf{G}$, resulting in the following form:

$$\begin{aligned} H = -\sum_{\mathbf{k}} \Big\{ & a^\dagger_{\mathbf{k}} f(\mathbf{k}) b_{\mathbf{k}} + a^\dagger_{\mathbf{k}+\mathbf{G}}\tilde{\Delta} f(\mathbf{k}+p\mathbf{K}_+ + q\mathbf{K}_-)b_{\mathbf{k}} + a^\dagger_{\mathbf{k}-\mathbf{G}}\tilde{\Delta}^* f(\mathbf{k}-p\mathbf{K}_+ - q\mathbf{K}_-)b_{\mathbf{k}} + \\ & + a^\dagger_{\mathbf{k}+\mathbf{G}} f(\mathbf{k}+\mathbf{G}) b_{\mathbf{k}+\mathbf{G}} + a^\dagger_{\mathbf{k}-\mathbf{G}}\tilde{\Delta} f(\mathbf{k}+p\mathbf{K}_+ + q\mathbf{K}_- + \mathbf{G})b_{\mathbf{k}+\mathbf{G}} + \\ & + a^\dagger_{\mathbf{k}}\tilde{\Delta}^* f(\mathbf{k}-p\mathbf{K}_+ - q\mathbf{K}_- + \mathbf{G})b_{\mathbf{k}-\mathbf{G}} + a^\dagger_{\mathbf{k}-\mathbf{G}} f(\mathbf{k}-\mathbf{G}) b_{\mathbf{k}-\mathbf{G}} + \\ & + a^\dagger_{\mathbf{k}}\tilde{\Delta} f(\mathbf{k}+p\mathbf{K}_+ + q\mathbf{K}_- - \mathbf{G})b_{\mathbf{k}-\mathbf{G}} + a^\dagger_{\mathbf{k}+\mathbf{G}}\tilde{\Delta}^* f(\mathbf{k}-p\mathbf{K}_+ - q\mathbf{K}_- - \mathbf{G})b_{\mathbf{k}-\mathbf{G}} \Big\} + \text{H.c.}, \end{aligned} \tag{A.0.6}$$

and rewrite the Hamiltonian as:

$$H = -\Psi^\dagger_{\mathbf{k}}\begin{pmatrix} \mathbf{0} & \mathcal{F}(\mathbf{k}) \\ \mathcal{F}^\dagger(\mathbf{k}) & \mathbf{0} \end{pmatrix}\Psi_{\mathbf{k}}, \tag{A.0.7}$$

where we have defined the spinor $\Psi_{\mathbf{k}} = (a_{\mathbf{k}}, a_{\mathbf{k}-\mathbf{G}}, a_{\mathbf{k}+\mathbf{G}}, b_{\mathbf{k}}, b_{\mathbf{k}-\mathbf{G}}, b_{\mathbf{k}+\mathbf{G}}, c_{\mathbf{k}}, c_{\mathbf{k}-\mathbf{G}}, c_{\mathbf{k}+\mathbf{G}})$, and the coupling matrix $\mathcal{F}(\mathbf{k})$ takes the form:

$$\mathcal{F}(\mathbf{k}) = \begin{pmatrix} f(\mathbf{k}) & f(\mathbf{k}+p\mathbf{K}_+ + q\mathbf{K}_- - \mathbf{G}) & f(\mathbf{k}-p\mathbf{K}_+ - q\mathbf{K}_- + \mathbf{G}) \\ f(\mathbf{k}-p\mathbf{K}_+ - q\mathbf{K}_-) & f(\mathbf{k}-\mathbf{G}) & f(\mathbf{k}+p\mathbf{K}_+ + q\mathbf{K}_- + \mathbf{G}) \\ f(\mathbf{k}+p\mathbf{K}_+ + q\mathbf{K}_-) & f(\mathbf{k}-p\mathbf{K}_+ - q\mathbf{K}_- - \mathbf{G}) & f(\mathbf{k}+\mathbf{G}) \end{pmatrix}, \tag{A.0.8}$$

which can be rewritten using the index equation $\nu = 1 + q - p \bmod 3$, leading to

$$\begin{aligned} f(\mathbf{k}+p\mathbf{K}_+ + q\mathbf{K}_-) &= f(\mathbf{k}+(p-\nu)\mathbf{K}_+ + (q+\nu)\mathbf{K}_- + \nu\mathbf{G}), \\ &= f(\mathbf{k}+(2p-q)\mathbf{K}_+ + (2q-p)\mathbf{K}_- + (\nu-1)\mathbf{G}). \end{aligned} \tag{A.0.9}$$

Given that $p, q \in \mathbb{Z}_3$, it follows $[(2p-q)\mathbf{K}_+ + (2q-p)\mathbf{K}_-]\cdot\boldsymbol{\delta}_n = 2\pi(p+q)/3$ for $n = 1, 2, 3$. Therefore, the function $f(\mathbf{k})$ can be rewritten as

$$f(\mathbf{k}+p\mathbf{K}_+ + q\mathbf{K}_-) = \Delta f(\mathbf{k}+(\nu-1)\mathbf{G}), \qquad \Delta = e^{i\frac{2\pi}{3}(p+q)}. \tag{A.0.10}$$

From the previous equation, it follows that $f(\mathbf{k}-p\mathbf{K}_+-q\mathbf{K}_-)=\Delta^* f(\mathbf{k}+(1-\nu)\mathbf{G})$. Therefore, the coupling matrix in Eq. (A.0.8) can be written as

$$\mathcal{F}_\nu(\mathbf{k})=\begin{pmatrix} f_0 & \Delta f_{\nu+1} & \Delta^* f_{-\nu-1} \\ \Delta^* f_{1-\nu} & f_{-1} & \Delta f_\nu \\ \Delta f_{\nu-1} & \Delta^* f_{-\nu} & f_1 \end{pmatrix}. \tag{A.0.11}$$

where $f_n(\mathbf{k})=f(\mathbf{k}+n\mathbf{G})$.

The low-energy spectrum of Kekulé-distorted graphene is governed by four dominant modes $u_\mathbf{k}=(a_{\mathbf{k}-\mathbf{G}},\, a_{\mathbf{k}+\mathbf{G}},\, b_{\mathbf{k}-\mathbf{G}},\, b_{\mathbf{k}+\mathbf{G}})$. In this basis, the Hamiltonian is expressed as:

$$H=-u_\mathbf{k}^\dagger\begin{pmatrix}\mathbf{0} & h_\nu(\mathbf{k}) \\ h_\nu^\dagger(\mathbf{k}) & \mathbf{0}\end{pmatrix}u_\mathbf{k}, \qquad h_\nu=\begin{pmatrix} f_{-1} & \tilde{\Delta} f_\nu \\ \tilde{\Delta}^* f_{-\nu} & f_1\end{pmatrix}. \tag{A.0.12}$$

where the functions $f_n(\mathbf{k})=f(\mathbf{k}+n\mathbf{G})$ are defined from the structure factor of the honeycomb lattice:

$$f_n(\mathbf{k})=-t\sum_{i=1}^{3} e^{i\mathbf{k}\cdot\boldsymbol{\delta}_i}e^{in\mathbf{G}\cdot\boldsymbol{\delta}_i}. \tag{A.0.13}$$

To obtain a low-energy approximation, we expand $f_n(\mathbf{k})$ around $\mathbf{k}=0$ to first order:

$$f(\mathbf{k}+n\mathbf{G})\approx f(n\mathbf{G})+[\mathbf{k}\cdot\nabla_\mathbf{k} f(\mathbf{k})|_{\mathbf{k}=0}]+\mathcal{O}(k^2)=-t\sum_{i=1}^{3}\left[(1+i\mathbf{k}\cdot\boldsymbol{\delta}_i)e^{in\mathbf{G}\cdot\boldsymbol{\delta}_i}\right]. \tag{A.0.14}$$

Using this expression, we obtain the following equation:

$$\begin{aligned} f(\mathbf{k}+n\mathbf{G}) &= -t[(1+i\mathbf{k}\cdot\boldsymbol{\delta}_1)e^{i\frac{2\pi}{3}n}+(1+i\mathbf{k}\cdot\boldsymbol{\delta}_2)e^{-i\frac{2\pi}{3}n}+(1+i\mathbf{k}\cdot\boldsymbol{\delta}_3)], \\ &= -t\left[e^{i\frac{2\pi}{3}n}+e^{-i\frac{2\pi}{3}n}+1+\frac{\sqrt{3}q_x}{2}i\left(e^{i\frac{2\pi}{3}n}-e^{-i\frac{2\pi}{3}n}\right)-\frac{q_y}{2}i(e^{i\frac{2\pi}{3}n}+e^{-i\frac{2\pi}{3}n}-2)\right], \\ &= -t\left[2\cos\left(\frac{2\pi n}{3}\right)+1-\sqrt{3}q_x\sin\left(\frac{2\pi n}{3}\right)-q_y i\left(\cos\left(\frac{2\pi n}{3}\right)-1\right)\right]. \end{aligned} \tag{A.0.15}$$

Evaluating explicitly for $n=\pm1$, and using the symmetry of the honeycomb lattice, we obtain:

$$f_{\pm1}(\mathbf{k})=-\frac{3t}{2}(\mp q_x+iq_y)=\hbar v_F(\mp q_x+iq_y), \tag{A.0.16}$$

where the Fermi velocity is defined as $v_F=\frac{3ta}{2\hbar}$, and (q_x,q_y) denote components of $\mathbf{k}$. For $n=0$, the result simplifies to:

$$f_0(\mathbf{k})=-3t. \tag{A.0.17}$$

To express the Hamiltonian in the valley-isotropic representation, we applied the unitary transformation $u_\mathbf{k}=(a_{\mathbf{k}-\mathbf{G}},\, a_{\mathbf{k}+\mathbf{G}},\, b_{\mathbf{k}-\mathbf{G}},\, b_{\mathbf{k}+\mathbf{G}})\rightarrow u_\mathbf{k}=(-b_{\mathbf{k}-\mathbf{G}},\, a_{\mathbf{k}-\mathbf{G}},\, a_{\mathbf{k}+\mathbf{G}},\, b_{\mathbf{k}+\mathbf{G}})$, leading to the transformed Hamiltonian:

$$\mathcal{H}(\mathbf{k})=\begin{pmatrix} v_F\mathbf{p}\cdot\boldsymbol{\sigma} & \tilde{\Delta}Q_\nu \\ \tilde{\Delta}^* Q_\nu^\dagger & v_F\mathbf{p}\cdot\boldsymbol{\sigma}\end{pmatrix}, \tag{A.0.18}$$

where $\mathbf{p} = (p_x, p_y)$, $\boldsymbol{\sigma} = (\sigma_x, \sigma_y)$ is the Pauli matrix vector acting on sublattice space, and the term $v_F \mathbf{p} \cdot \boldsymbol{\sigma}$ captures the linear Dirac dispersion. The off-diagonal matrix Q_v encodes the Kekulé-induced intervalley coupling and depends on the Kekulé texture:

$$Q_v = \begin{pmatrix} f_{-v}^* & 0 \\ 0 & -f_v \end{pmatrix} = \begin{cases} 3t\sigma_z, & v = 0 \\ v_F(vp_x - p_y i)\sigma_0, & |v| = 1 \end{cases} . \tag{A.0.19}$$

B

Details of the Kekulé-modulated α-$\mathcal{T}_3$ model

In this appendix provides supplementary derivations for the Kekulé-modulated α-$\mathcal{T}_3$ model, including the formulation of the spatially modulated hopping amplitudes, the symmetry constraints enforced by the superlattice structure, and the explicit construction of the tight-binding Hamiltonian in momentum space and its corresponding low-energy expansion.

B.1 Hopping amplitude

To reproduce the lattice structure shown in Fig. 4.1 (a), we introduce a hopping amplitude $t(\mathbf{r}, \boldsymbol{\delta}_j)$ that depends explicitly on the position $\mathbf{r}$ and on the nearest-neighbor vector $\boldsymbol{\delta}_j$. The modulation must respect the periodicity of the superlattice,

$$t(\mathbf{r}, \boldsymbol{\delta}_j) = t(\mathbf{r} + \mathbf{R}, \boldsymbol{\delta}_j), \tag{B.1.1}$$

where

$$\mathbf{R} = n(2\mathbf{a}_1 - \mathbf{a}_2) + m(2\mathbf{a}_2 - \mathbf{a}_1), \qquad n, m \in \mathbb{Z}. \tag{B.1.2}$$

For convenience, we assume a parametrization of the form

$$t(\mathbf{r}, \boldsymbol{\delta}_i) = \alpha\big[t + t'(\mathbf{r}, \boldsymbol{\delta}_i)\big], \tag{B.1.3}$$

where it is sufficient to require periodicity only for the modulation t'. We adopt the simple ansatz

$$t'(\mathbf{r}, \boldsymbol{\delta}_j) = 2t\mathbb{R}\mathrm{e}\{e^{i\mathbf{F}\cdot\boldsymbol{\delta}_j + i\mathbf{G}\cdot\mathbf{r}}\} = t\cos\big(\mathbf{F}\cdot\boldsymbol{\delta}_j + \mathbf{G}\cdot\mathbf{r}\big). \tag{B.1.4}$$

Imposing superlattice periodicity,

$$e^{i\mathbf{F}\cdot\boldsymbol{\delta}_j + i\mathbf{G}\cdot(\mathbf{r}+\mathbf{R})} = e^{i\mathbf{F}\cdot\boldsymbol{\delta}_j + i\mathbf{G}\cdot\mathbf{r}} \qquad \Rightarrow \qquad e^{i\mathbf{G}\cdot\mathbf{R}} = 1, \tag{B.1.5}$$

implies that $\mathbf{G}$ must belong to the reciprocal lattice of the superlattice. The reciprocal lattice of the Kekulé-modulated honeycomb coincides with the set generated by the graphene Dirac points $\mathbf{K}_\pm$. An identical argument applies to $\mathbf{F}$. Thus, we write

$$\mathbf{G} = p\mathbf{K}_+ + q\mathbf{K}_-, \qquad \mathbf{F} = u\mathbf{K}_+ + v\mathbf{K}_-, \qquad p,q,u,v \in \mathbb{Z}. \tag{B.1.6}$$

For all superlattice vectors $\mathbf{R}$, we require the following two conditions:

$$t'(\mathbf{R}, \boldsymbol{\delta}_3) = t'(\mathbf{R} + \mathbf{a}_i, \boldsymbol{\delta}_i) \neq 0, \tag{B.1.7}$$

$$t'(\mathbf{R}, \boldsymbol{\delta}_j) = t'(\mathbf{R} + \mathbf{a}_i, \boldsymbol{\delta}_j) = -\tfrac{1}{2}, \tag{B.1.8}$$

with $i,j \in \{1,2\}$, $i \neq j$. The first condition ensures that site C couples only through hoppings that carry the Kekulé periodicity, while the second condition imposes that certain bonds vanish, effectively disconnecting the remaining sites from the tight-binding model.

Imposing equality between the corresponding amplitudes yields

$$\mathbf{F}\cdot\boldsymbol{\delta}_3 = \mathbf{F}\cdot\boldsymbol{\delta}_2 + \mathbf{G}\cdot(\boldsymbol{\delta}_3 - \boldsymbol{\delta}_2) \quad \Rightarrow \quad \mathbf{F}\cdot(\boldsymbol{\delta}_3 - \boldsymbol{\delta}_2) = \mathbf{G}\cdot(\boldsymbol{\delta}_3 - \boldsymbol{\delta}_2), \tag{B.1.9}$$

which is satisfied if and only if $\mathbf{F} = \mathbf{G}$. With this identification, the modulation becomes

$$t'(\mathbf{r}, \boldsymbol{\delta}_j) = 2t\mathbb{R}\mathrm{e}\{e^{i\mathbf{G}\cdot(\mathbf{r}+\boldsymbol{\delta}_j)}\} = t\cos\big[\mathbf{G}\cdot(\mathbf{r}+\boldsymbol{\delta}_j)\big]. \tag{B.1.10}$$

To determine the coefficients p and q, we use the non-vanishing condition and set (without loss of generality) $t'(\mathbf{R}, \boldsymbol{\delta}_3) = 1$. This gives

$$\cos(\mathbf{G}\cdot\boldsymbol{\delta}_3) = 1 \quad \Rightarrow \quad \frac{2\pi}{3}(p+q) = 2\pi k, \qquad k \in \mathbb{Z}. \tag{B.1.11}$$

Choosing $k = 0$ yields $p = -q$. Next, imposing the vanishing condition

$$\cos(\mathbf{G}\cdot\boldsymbol{\delta}_2) = -\tfrac{1}{2}, \tag{B.1.12}$$

and using $p = -q$, we obtain

$$-\frac{4\pi}{6}p = \pm\frac{2\pi}{3} + 2\pi k, \qquad k \in \mathbb{Z}. \tag{B.1.13}$$

Setting $k = 0$ gives $p = \pm 1$. We choose $p = 1$ and thus $q = -1$. Therefore, $\mathbf{G} = \mathbf{K}_+ - \mathbf{K}_-$ is the Kekulé wave vector, and the final form of the hopping amplitude is

$$t_{\mathbf{r},j} \equiv t(\mathbf{r}, \boldsymbol{\delta}_j) = \alpha t\{1 + 2\mathbb{R}\mathrm{e}\{e^{i\mathbf{G}\cdot(\mathbf{r}+\boldsymbol{\delta}_j)}\}\}. \tag{B.1.14}$$

B.2 Tight-binding Hamiltonian

We start from the tight-binding Hamiltonian of Kekulé-modulated α-$\mathcal{T}_3$ model:

$$H = -t\sum_{\mathbf{r}}\sum_{j=1}^{3} b_{\mathbf{r}}^\dagger a_{\mathbf{r}-\boldsymbol{\delta}_j} - \sum_{\mathbf{r}}\sum_{j=1}^{3} t_{\mathbf{r},j}\, b_{\mathbf{r}}^\dagger c_{\mathbf{r}+\boldsymbol{\delta}_j} + \mathrm{H.c.}, \tag{B.2.1}$$

where the C sites hoppings is introduced as $t_{\mathbf{r},j} = \alpha t\{1 + 2\mathbb{R}\mathrm{e}[e^{i\mathbf{G}\cdot(\mathbf{r}+\boldsymbol{\delta}_j)}]\}$. with Kekulé wavevector $\mathbf{G} = \mathbf{K}_+ - \mathbf{K}_-$. The Hamiltonian can be split into two parts:

$$\begin{aligned} H &= -t\sum_{\mathbf{r}}\sum_{j=1}^{3} b_{\mathbf{r}}^{\dagger}a_{\mathbf{r}-\boldsymbol{\delta}_j} - \alpha t\sum_{\mathbf{r}}\sum_{j=1}^{3} b_{\mathbf{r}}^{\dagger}c_{\mathbf{r}+\boldsymbol{\delta}_j} - 2\alpha t\sum_{\mathbf{r}}\sum_{j=1}^{3}\mathbb{R}\mathrm{e}\{e^{i\mathbf{G}\cdot(\mathbf{r}+\boldsymbol{\delta}_j)}\}b_{\mathbf{r}}^{\dagger}c_{\mathbf{r}+\boldsymbol{\delta}_n} + \mathrm{H.c.},\\ &= H_\alpha + H_C \end{aligned} \tag{B.2.2}$$

where H_α corresponds to α-$\mathcal{T}_3$ model and H_C captures the additional sites in sublattice C. We proceed with the Fourier transform:

$$\begin{aligned} H_C &= -\alpha t\sum_{\mathbf{r}}\sum_{j=1}^{3}[e^{i\mathbf{G}\cdot\mathbf{r}+i\mathbf{G}\cdot\boldsymbol{\delta}_j} + e^{-i\mathbf{G}\cdot\mathbf{r}-i\mathbf{G}\cdot\boldsymbol{\delta}_j}]b_{\mathbf{r}}^{\dagger}c_{\mathbf{r}+\boldsymbol{\delta}_j} + \mathrm{H.c.},\\ &= -\frac{\alpha t}{N}\sum_{\mathbf{k},\mathbf{k}'}\sum_{\mathbf{r}}\sum_{j=1}^{3}[e^{i\mathbf{G}\cdot\mathbf{r}+i\mathbf{G}\cdot\boldsymbol{\delta}_j} + e^{-i\mathbf{G}\cdot\mathbf{r}-i\mathbf{G}\cdot\boldsymbol{\delta}_j}]b_{\mathbf{k}}^{\dagger}e^{i(\mathbf{k}'-\mathbf{k})\cdot\mathbf{r}}e^{i\mathbf{k}'\cdot\boldsymbol{\delta}_j}c_{\mathbf{k}'} + \mathrm{H.c.},\\ &= -\frac{\alpha t}{N}\sum_{\mathbf{k},\mathbf{k}'}\sum_{\mathbf{r}}\sum_{j=1}^{3}\left[b_{\mathbf{k}}^{\dagger}e^{-i[\mathbf{k}-(\mathbf{k}'+\mathbf{G})]\cdot\mathbf{r}}e^{i(\mathbf{k}'+\mathbf{G})\cdot\boldsymbol{\delta}_j}c_{\mathbf{k}'} + b_{\mathbf{k}}^{\dagger}e^{-i[\mathbf{k}-(\mathbf{k}'-\mathbf{G})]\cdot\mathbf{r}}e^{i(\mathbf{k}'-\mathbf{G})\cdot\boldsymbol{\delta}_j}c_{\mathbf{k}'}\right] + \mathrm{H.c.}, \end{aligned} \tag{B.2.3}$$

where N is the number of sites of the lattice. After summing over real space, we obtain momentum-conserving delta functions and the result:

$$H_C = -\alpha t\sum_{\mathbf{k}'}\sum_{n=1}^{3}\left[b_{\mathbf{k}'+\mathbf{G}}^{\dagger}e^{i(\mathbf{k}'+\mathbf{G})\cdot\boldsymbol{\delta}_j}c_{\mathbf{k}'} + b_{\mathbf{k}'-\mathbf{G}}^{\dagger}e^{i(\mathbf{k}'-\mathbf{G})\cdot\boldsymbol{\delta}_j}c_{\mathbf{k}'}\right] + \mathrm{H.c.} \tag{B.2.4}$$

Using the definition of the structure factor for nearest-neighbor hopping $f(\mathbf{k}) = t\sum_n e^{i\mathbf{k}\cdot\boldsymbol{\delta}_j}$. The full Hamiltonian in momentum space becomes:

$$H = -\sum_{\mathbf{k}} a_{\mathbf{k}}^{\dagger}f(\mathbf{k})b_{\mathbf{k}} - \alpha\sum_{\mathbf{k}}\left[b_{\mathbf{k}}^{\dagger}f(\mathbf{k})c_{\mathbf{k}} + b_{\mathbf{k}+\mathbf{G}}^{\dagger}f(\mathbf{k}+\mathbf{G})c_{\mathbf{k}} + b_{\mathbf{k}-\mathbf{G}}^{\dagger}f(\mathbf{k}-\mathbf{G})c_{\mathbf{k}}\right] + \mathrm{H.c.}\,. \tag{B.2.5}$$

We can expand the Hamiltonian by shifting each term by $+\mathbf{G}$ and $-\mathbf{G}$, resulting in the following form:

$$\begin{aligned} H = -\sum_{\mathbf{k}}\big\{ & a_{\mathbf{k}}^{\dagger}f(\mathbf{k})b_{\mathbf{k}} + b_{\mathbf{k}}^{\dagger}\alpha f(\mathbf{k})c_{\mathbf{k}} + b_{\mathbf{k}+\mathbf{G}}^{\dagger}\alpha f(\mathbf{k}+\mathbf{G})c_{\mathbf{k}} + b_{\mathbf{k}-\mathbf{G}}^{\dagger}\alpha f(\mathbf{k}-\mathbf{G})c_{\mathbf{k}} +\\ & + a_{\mathbf{k}+\mathbf{G}}^{\dagger}f(\mathbf{k}+\mathbf{G})b_{\mathbf{k}+\mathbf{G}} + b_{\mathbf{k}+\mathbf{G}}^{\dagger}\alpha f(\mathbf{k}+\mathbf{G})c_{\mathbf{k}+\mathbf{G}} + b_{\mathbf{k}-\mathbf{G}}^{\dagger}\alpha f(\mathbf{k}-\mathbf{G})c_{\mathbf{k}+\mathbf{G}} + b_{\mathbf{k}}^{\dagger}\alpha f(\mathbf{k})c_{\mathbf{k}+\mathbf{G}} +\\ & + a_{\mathbf{k}-\mathbf{G}}^{\dagger}f(\mathbf{k}-\mathbf{G})b_{\mathbf{k}-\mathbf{G}} + b_{\mathbf{k}-\mathbf{G}}^{\dagger}\alpha f(\mathbf{k}-\mathbf{G})c_{\mathbf{k}-\mathbf{G}} + b_{\mathbf{k}}^{\dagger}\alpha f(\mathbf{k})c_{\mathbf{k}-\mathbf{G}} + b_{\mathbf{k}+\mathbf{G}}^{\dagger}\alpha f(\mathbf{k}+\mathbf{G})c_{\mathbf{k}-\mathbf{G}}\big\} + \mathrm{H.c.}, \end{aligned} \tag{B.2.6}$$

and rewrite the Hamiltonian as:

$$H = -\Psi_{\mathbf{k}}^{\dagger}\begin{pmatrix} \mathbf{0} & \mathcal{F}(\mathbf{k}) & \mathbf{0}\\ \mathcal{F}^{\dagger}(\mathbf{k}) & \mathbf{0} & \alpha\mathcal{E}(\mathbf{k})\\ \mathbf{0} & \alpha\mathcal{E}^{\dagger}(\mathbf{k}) & \mathbf{0}\end{pmatrix}\Psi_{\mathbf{k}}, \tag{B.2.7}$$

where we have defined the spinor $\Psi_{\mathbf{k}} = (a_{\mathbf{k}}, a_{\mathbf{k}-\mathbf{G}}, a_{\mathbf{k}+\mathbf{G}}, b_{\mathbf{k}}, b_{\mathbf{k}-\mathbf{G}}, b_{\mathbf{k}+\mathbf{G}}, c_{\mathbf{k}}, c_{\mathbf{k}-\mathbf{G}}, c_{\mathbf{k}+\mathbf{G}})^T$, and the coupling matrices $\mathcal{F}(\mathbf{k})$ and $\mathcal{E}(\mathbf{k})$ takes the form:

$$\mathcal{F}(\mathbf{k}) = \begin{pmatrix} f_0 & 0 & 0 \\ 0 & f_{-1} & 0 \\ 0 & 0 & f_1 \end{pmatrix}, \quad \mathcal{E}(\mathbf{k}) = \begin{pmatrix} f_0 & f_0 & f_0 \\ f_{-1} & f_{-1} & f_{-1} \\ f_1 & f_1 & f_1 \end{pmatrix}, \tag{B.2.8}$$

with $f_n = f(\mathbf{k} + n\mathbf{G})$, and we have used the relation $f(\mathbf{k} \pm 2\mathbf{G}) = f(\mathbf{k} \mp \mathbf{G})$ [25].

The low-energy spectrum of Kek-α model is governed by six dominant modes $u_{\mathbf{k}} = (a_{\mathbf{k}-\mathbf{G}}, a_{\mathbf{k}+\mathbf{G}}, b_{\mathbf{k}-\mathbf{G}}, b_{\mathbf{k}+\mathbf{G}}, c_{\mathbf{k}-\mathbf{G}}, c_{\mathbf{k}+\mathbf{G}})$. In this basis, the Hamiltonian is expressed as:

$$H_{\text{eff}} = u_{\mathbf{k}}^{\dagger} \begin{pmatrix} \mathbf{0} & g(\mathbf{k}) & \mathbf{0} \\ g^{\dagger}(\mathbf{k}) & \mathbf{0} & \alpha h(\mathbf{k}) \\ \mathbf{0} & \alpha h^{\dagger}(\mathbf{k}) & \mathbf{0} \end{pmatrix} u_{\mathbf{k}}, \quad g(\mathbf{k}) = \begin{pmatrix} f_{-1} & 0 \\ 0 & f_1 \end{pmatrix}, \quad h(\mathbf{k}) = \begin{pmatrix} f_{-1} & f_{-1} \\ f_1 & f_1 \end{pmatrix}. \tag{B.2.9}$$

where the functions $f_n(\mathbf{k}) = f(\mathbf{k} + n\mathbf{G})$ are defined from the structure factor of the honeycomb lattice:

$$f_n(\mathbf{k}) = -t \sum_{i=1}^{3} e^{i\mathbf{k}\cdot\boldsymbol{\delta}_i} e^{in\mathbf{G}\cdot\boldsymbol{\delta}_i}. \tag{B.2.10}$$

To obtain a low-energy approximation, we expand $f_n(\mathbf{k})$ around $\mathbf{k} = 0$ to first order:

$$f(\mathbf{k} + n\mathbf{G}) \approx f(n\mathbf{G}) + [\mathbf{k} \cdot \nabla_{\mathbf{k}} f(\mathbf{k})|_{\mathbf{k}=0}] + \mathcal{O}(k^2) = -t \sum_{i=1}^{3} \left[(1 + i\mathbf{k} \cdot \boldsymbol{\delta}_i) e^{in\mathbf{G}\cdot\boldsymbol{\delta}_i} \right] \tag{B.2.11}$$

apartir de esta expresión podemos desarrollar

$$\begin{aligned} f(\mathbf{k} + n\mathbf{G}) &= -t[(1 + i\mathbf{k} \cdot \boldsymbol{\delta}_1) e^{i\frac{2\pi}{3}n} + (1 + i\mathbf{k} \cdot \boldsymbol{\delta}_2) e^{-i\frac{2\pi}{3}n} + (1 + i\mathbf{k} \cdot \boldsymbol{\delta}_3)] \\ &= -t \left[e^{i\frac{2\pi}{3}n} + e^{-i\frac{2\pi}{3}n} + 1 + \frac{\sqrt{3}q_x}{2} i \left(e^{i\frac{2\pi}{3}n} - e^{-i\frac{2\pi}{3}n} \right) - \frac{q_y}{2} i (e^{i\frac{2\pi}{3}n} + e^{-i\frac{2\pi}{3}n} - 2) \right] \\ &= -t \left[2\cos\left(\frac{2\pi n}{3}\right) + 1 - \sqrt{3}q_x \sin\left(\frac{2\pi n}{3}\right) - q_y i \left(\cos\left(\frac{2\pi n}{3}\right) - 1 \right) \right] \end{aligned} \tag{B.2.12}$$

Evaluating explicitly for $n = \pm 1$, and using the symmetry of the honeycomb lattice, we obtain:

$$f_{\pm 1}(\mathbf{k}) = -\frac{3t}{2}(\mp q_x + i q_y) = \hbar v_F (\mp q_x + i q_y), \tag{B.2.13}$$

where the Fermi velocity is defined as $v_F = \frac{3ta}{2\hbar}$, and (q_x, q_y) denote components of $\mathbf{k}$.

To express the Hamiltonian in the Dirac-like representation, we applied the unitary transformation:

$u_{\mathbf{k}} = (a_{\mathbf{k}-\mathbf{G}}, a_{\mathbf{k}+\mathbf{G}}, b_{\mathbf{k}-\mathbf{G}}, b_{\mathbf{k}+\mathbf{G}}, c_{\mathbf{k}-\mathbf{G}}, c_{\mathbf{k}+\mathbf{G}}) \to u_{\mathbf{k}} = (a_{\mathbf{k}+\mathbf{G}}, -b_{\mathbf{k}+\mathbf{G}}, c_{\mathbf{k}+\mathbf{G}}, a_{\mathbf{k}-\mathbf{G}}, b_{\mathbf{k}-\mathbf{G}}, c_{\mathbf{k}-\mathbf{G}})$, leading to the transformed Hamiltonian:

$$\mathcal{H}(\mathbf{k}) = \begin{pmatrix} v_F \mathbf{p} \cdot \mathbf{S} & Q \\ Q^{\dagger} & v_F \mathbf{p} \cdot \mathbf{S}^* \end{pmatrix}, \tag{B.2.14}$$

where $\mathbf{p} = (p_x, p_y)$, $\boldsymbol{\sigma} = (\sigma_x, \sigma_y)$ is the Pauli matrix vector acting on sublattice space, and the term $v_F \mathbf{p} \cdot \boldsymbol{\sigma}$ captures the linear Dirac dispersion. The off-diagonal matrix Q encodes the Kekulé-induced intervalley coupling:

$$Q = \alpha v_F \begin{pmatrix} 0 & 0 & 0 \\ 0 & 0 & p_x + i p_y \\ 0 & p_x + i p_y & 0 \end{pmatrix}, \tag{B.2.15}$$

C

Numerical implementation of the tight-binding model

In this appendix, we describe the numerical procedure used to obtain the band structures presented for the Kekulé-modulated α–$\mathcal{T}_3$ model.

The band structures were computed using a tight-binding approach based on the Bloch Hamiltonian of the Kekulé-modulated α–$\mathcal{T}_3$ model. The enlarged $\sqrt{3} \times \sqrt{3}$ supercell contains six sites belonging to the honeycomb lattice (A_i and B_j) and one additional site C, giving rise to a 7×7 Bloch Hamiltonian $H(\mathbf{k})$ of the form

$$H(\mathbf{k}) = \begin{array}{c} \\ A_1 \\ B_1 \\ A_2 \\ B_2 \\ A_3 \\ B_3 \\ C \end{array} \begin{array}{c} \begin{array}{ccccccc} A_1 & B_1 & A_2 & B_2 & A_3 & B_3 & C \end{array} \\ \left(\begin{array}{ccccccc|c} & & & & & & & \\ & & & H_{A-B} & & & & H_{B-C} \\ & & & & & & & \\ & & & & & & & \\ & & & & & & & \\ & & & & & & & \\ \hline & & & H_{B-C}^{\dagger} & & & & H_{C-C} \end{array} \right) \end{array} \tag{C.0.1}$$

This Hamiltonian naturally decomposes into: (i) a 6×6 block H_{A-B} describing all intralayer honeycomb hoppings inside the $\sqrt{3} \times \sqrt{3}$ supercell; (ii) a 1×6 block H_{B-C} describing the B–C coupling (with $H_{B-C}^{\dagger}$ representing the reverse process); and (iii) a scalar term H_{C-C} for the on-site energy of the central C atom.

The atoms in the supercell are labeled as $A_1, B_1, A_2, B_2, A_3, B_3$ following a clockwise ordering starting from the top site of the hexagon, while the central site is denoted by C.

All calculations were performed within a nearest-neighbor tight-binding model. The perpendicular electric field was incorporated as a sublattice-staggered on-site potential m. The parameter α determines the coupling strength between the B sites and the

central C site. All interactions are expressed in terms of the three nearest-neighbor vectors

$$\boldsymbol{\delta}_1 = \tfrac{a}{2}(\sqrt{3}, -1), \qquad \boldsymbol{\delta}_2 = -\tfrac{a}{2}(\sqrt{3}, 1), \qquad \boldsymbol{\delta}_3 = a(0, 1), \tag{C.0.2}$$

so that the hopping amplitudes acquire complex Bloch-phase factors $t\, e^{i\mathbf{k}\cdot\boldsymbol{\delta}_j}$ for A–B bonds and $\alpha t\, e^{i\mathbf{k}\cdot\boldsymbol{\delta}_j}$ for B–C bonds.

An equivalent decomposition of the Hamiltonian is

$$H(\mathbf{k}) = H_{\text{in}}(\mathbf{k}) + H_{\text{out}}(\mathbf{k}) + H_m(\mathbf{k}), \tag{C.0.3}$$

where $H_{\text{in}}(\mathbf{k})$ contains all nearest-neighbor hoppings inside the supercell, $H_{\text{out}}(\mathbf{k})$ contains hoppings connecting to adjacent supercells, and $H_m(\mathbf{k})$ includes the on-site mass terms. The explicit 7×7 matrices used in the numerical calculations are:

$$H_{\text{in}}(\mathbf{k}) = -\begin{pmatrix} 0 & te^{i\mathbf{k}\cdot\boldsymbol{\delta}_1} & 0 & 0 & 0 & te^{i\mathbf{k}\cdot\boldsymbol{\delta}_2} & 0 \\ te^{-i\mathbf{k}\cdot\boldsymbol{\delta}_1} & 0 & te^{-i\mathbf{k}\cdot\boldsymbol{\delta}_3} & 0 & 0 & 0 & \alpha te^{i\mathbf{k}\cdot\boldsymbol{\delta}_2} \\ 0 & te^{i\mathbf{k}\cdot\boldsymbol{\delta}_3} & 0 & te^{i\mathbf{k}\cdot\boldsymbol{\delta}_2} & 0 & 0 & 0 \\ 0 & 0 & te^{-i\mathbf{k}\cdot\boldsymbol{\delta}_2} & 0 & te^{-i\mathbf{k}\cdot\boldsymbol{\delta}_1} & 0 & \alpha te^{i\mathbf{k}\cdot\boldsymbol{\delta}_3} \\ 0 & 0 & 0 & te^{i\mathbf{k}\cdot\boldsymbol{\delta}_1} & 0 & te^{i\mathbf{k}\cdot\boldsymbol{\delta}_3} & 0 \\ te^{-i\mathbf{k}\cdot\boldsymbol{\delta}_2} & 0 & 0 & 0 & te^{-i\mathbf{k}\cdot\boldsymbol{\delta}_3} & 0 & \alpha te^{i\mathbf{k}\cdot\boldsymbol{\delta}_1} \\ 0 & \alpha te^{-i\mathbf{k}\cdot\boldsymbol{\delta}_2} & 0 & \alpha te^{-i\mathbf{k}\cdot\boldsymbol{\delta}_3} & 0 & \alpha te^{-i\mathbf{k}\cdot\boldsymbol{\delta}_1} & 0 \end{pmatrix} \tag{C.0.4}$$

$$H_{\text{out}}(\mathbf{k}) = -\begin{pmatrix} 0 & 0 & 0 & te^{i\mathbf{k}\cdot\boldsymbol{\delta}_3} & 0 & 0 & 0 \\ 0 & 0 & 0 & 0 & te^{-i\mathbf{k}\cdot\boldsymbol{\delta}_2} & 0 & 0 \\ 0 & 0 & 0 & 0 & 0 & te^{i\mathbf{k}\cdot\boldsymbol{\delta}_1} & 0 \\ te^{-i\mathbf{k}\cdot\boldsymbol{\delta}_3} & 0 & 0 & 0 & 0 & 0 & 0 \\ 0 & te^{i\mathbf{k}\cdot\boldsymbol{\delta}_2} & 0 & 0 & 0 & 0 & 0 \\ 0 & 0 & te^{-i\mathbf{k}\cdot\boldsymbol{\delta}_1} & 0 & 0 & 0 & 0 \\ 0 & 0 & 0 & 0 & 0 & 0 & 0 \end{pmatrix} \tag{C.0.5}$$

and the mass term:

$$H_m(\mathbf{k}) = m\,\mathrm{diag}(+1, -1, +1, -1, +1, -1, 0). \tag{C.0.6}$$

The band structures shown in Figs. 4.3 and 4.5 were obtained by numerically solving the eigenvalue problem

$$H(\mathbf{k})\, c(\mathbf{k}) = E(\mathbf{k})\, c(\mathbf{k}), \tag{C.0.7}$$

with $E(\mathbf{k})$ and $c(\mathbf{k})$ the eigenvalues and eigenvectors, respectively.

References

[1] P. Avouris, Z. Chen, and V. Perebeinos, Nature Nanotechnology 2007 2:10 **2**, 605 (2007).

[2] P. A. Tran, L. Zhang, and T. J. Webster, Advanced Drug Delivery Reviews **61**, 1097 (2009).

[3] L. E. F. F. Torres, S. Roche, and J.-C. Charlier, *Introduction to graphene-based nanomaterials: from electronic structure to quantum transport* (Cambridge University Press, 2014).

[4] H. W. Kroto, J. R. Heath, S. C. O'Brien, R. F. Curl, and R. E. Smalley, Nature 1985 318:6042 **318**, 162 (1985).

[5] S. Iijima, Nature **354**, 56 (1991).

[6] N. D. Mermin, Physical Review **176**, 250 (1968).

[7] K. S. Novoselov, A. K. Geim, S. V. Morozov, D. Jiang, Y. Zhang, S. V. Dubonos, I. V. Grigorieva, and A. A. Firsov, Science **306**, 666 (2004).

[8] K. S. Novoselov, A. K. Geim, S. V. Morozov, D. Jiang, M. I. Katsnelson, I. V. Grigorieva, S. V. Dubonos, and A. A. Firsov, Nature 2005 438:7065 **438**, 197 (2005).

[9] X. Du, I. Skachko, A. Barker, and E. Y. Andrei, Nature Nanotechnology 2008 3:8 **3**, 491 (2008).

[10] K. Bolotin, K. Sikes, Z. Jiang, M. Klima, G. Fudenberg, J. Hone, P. Kim, and H. Stormer, Solid State Communications **146**, 351 (2008).

[11] R. R. Nair, P. Blake, A. N. Grigorenko, K. S. Novoselov, T. J. Booth, T. Stauber, N. M. R. Peres, and A. K. Geim, Science **320**, 1308 (2008).

[12] K. F. Mak, M. Y. Sfeir, Y. Wu, C. H. Lui, J. A. Misewich, and T. F. Heinz, Physical Review Letters **101**, 196405 (2008).

[13] C. Lee, X. Wei, J. W. Kysar, and J. Hone, Science **321**, 385 (2008).

[14] K. S. Kim, Y. Zhao, H. Jang, S. Y. Lee, J. M. Kim, K. S. Kim, J. H. Ahn, P. Kim, J. Y. Choi, and B. H. Hong, Nature 2009 457:7230 **457**, 706 (2009).

[15] A. A. Balandin, S. Ghosh, W. Bao, I. Calizo, D. Teweldebrhan, F. Miao, and C. N. Lau, Nano Letters **8**, 902 (2008).

[16] D. C. Elias, R. R. Nair, T. M. Mohiuddin, S. V. Morozov, P. Blake, M. P. Halsall, A. C. Ferrari, D. W. Boukhvalov, M. I. Katsnelson, A. K. Geim, and K. S. Novoselov, Science **323**, 610 (2009).

[17] X. Wang, X. Li, L. Zhang, Y. Yoon, P. K. Weber, H. Wang, J. Guo, and H. Dai, Science **324**, 768 (2009).

[18] A. C. Ferrari, F. Bonaccorso, V. Fal'ko, K. S. Novoselov, S. Roche, P. Bøggild, S. Borini, F. H. L. Koppens, V. Palermo, N. Pugno, J. A. Garrido, R. Sordan, A. Bianco, L. Ballerini, M. Prato, E. Lidorikis, J. Kivioja, C. Marinelli, T. Ryhänen, A. Morpurgo, J. N. Coleman, V. Nicolosi, L. Colombo, A. Fert, M. Garcia-Hernandez, A. Bachtold, G. F. Schneider, F. Guinea, C. Dekker, M. Barbone, Z. Sun, C. Galiotis, A. N. Grigorenko, G. Konstantatos, A. Kis, M. Katsnelson, L. Vandersypen, A. Loiseau, V. Morandi, D. Neumaier, E. Treossi, V. Pellegrini, M. Polini, A. Tredicucci, G. M. Williams, B. Hee Hong, J.-H. Ahn, J. Min Kim, H. Zirath, B. J. van Wees, H. van der Zant, L. Occhipinti, A. Di Matteo, I. A. Kinloch, T. Seyller, E. Quesnel, X. Feng, K. Teo, N. Rupesinghe, P. Hakonen, S. R. T. Neil, Q. Tannock, T. Löfwander, and J. Kinaret, Nanoscale **7**, 4598 (2015).

[19] Dirac Paul Adrien Maurice, Proceedings of the Royal Society of London. Series A, Containing Papers of a Mathematical and Physical Character **117**, 610 (1928).

[20] M. Katsnelson and K. Novoselov, Solid State Communications **143**, 3 (2007).

[21] T. Wehling, A. Black-Schaffer, and A. Balatsky, Advances in Physics **63**, 1 (2014).

[22] A. Raoux, M. Morigi, J.-N. Fuchs, F. Piéchon, and G. Montambaux, Physical Review Letters **112**, 26402 (2014).

[23] C. Gutiérrez, C.-J. Kim, L. Brown, T. Schiros, D. Nordlund, E. Lochocki, K. M. Shen, J. Park, and A. N. Pasupathy, Nature Physics **12**, 950 (2016).

[24] C. Bao, H. Zhang, T. Zhang, X. Wu, L. Luo, S. Zhou, Q. Li, Y. Hou, W. Yao, L. Liu, P. Yu, J. Li, W. Duan, H. Yao, Y. Wang, and S. Zhou, Physical Review Letters **126**, 206804 (2021).

[25] O. V. Gamayun, V. P. Ostroukh, N. V. Gnezdilov, I. Adagideli, and C. W. J. Beenakker, New Journal of Physics **20**, 23016 (2018).

[26] X.-F. Zhou, X. Dong, A. R. Oganov, Q. Zhu, Y. Tian, and H.-T. Wang, Physical Review Letters **112**, 085502 (2014).

[27] A. D. Zabolotskiy and Y. E. Lozovik, Physical Review B **94**, 165403 (2016).

[28] M. I. Katsnelson, The European Physical Journal B - Condensed Matter and Complex Systems **51**, 157 (2006).

[29] K. Kristinsson, O. V. Kibis, S. Morina, and I. A. Shelykh, Scientific Reports 2016 6:1 **6**, 1 (2016).

[30] N. M. Peres, Reviews of Modern Physics **82**, 2673 (2010).

[31] J. R. Schaibley, H. Yu, G. Clark, P. Rivera, J. S. Ross, K. L. Seyler, W. Yao, and X. Xu, Nature Reviews Materials 2016 1:11 **1**, 1 (2016).

[32] Y. J. Zhang, T. Oka, R. Suzuki, J. T. Ye, and Y. Iwasa, Science **344**, 725 (2014).

[33] L. Ponomarenko, R. Gorbachev, G. Yu, D. Elias, R. Jalil, A. Patel, A. Mishchenko, A. Mayorov, C. Woods, J. Wallbank, *et al.*, Nature **497**, 594 (2013).

[34] C.-Y. Hou, C. Chamon, and C. Mudry, Phys. Rev. Lett. **98**, 186809 (2007).

[35] M. Yankowitz, J. Xue, D. Cormode, J. D. Sanchez-Yamagishi, K. Watanabe, T. Taniguchi, P. Jarillo-Herrero, P. Jacquod, and B. J. LeRoy, Nature Physics **8**, 382 (2012).

[36] F. Escudero, A. Sinner, Z. Zhan, P. A. Pantaleón, and F. Guinea, Phys. Rev. Res. **6**, 023203 (2024).

[37] C.-H. Park, L. Yang, Y.-W. Son, M. L. Cohen, and S. G. Louie, Nature Physics **4**, 213 (2008).

[38] K. K. Gomes, W. Mar, W. Ko, F. Guinea, and H. C. Manoharan, Nature **483**, 306 (2012).

[39] D. Eom and J.-Y. Koo, Nanoscale **12**, 19604 (2020).

[40] V. V. Cheianov, V. I. Fal'ko, O. Syljuåsen, and B. L. Altshuler, Solid State Communications **149**, 1499 (2009).

[41] V. V. Cheianov, O. Syljuåsen, B. L. Altshuler, and V. Fal'ko, Physical Review B **80**, 233409 (2009).

[42] M. Farjam and H. Rafii-Tabar, Physical Review B **79**, 045417 (2009).

[43] K. Sugawara, K. Kanetani, T. Sato, and T. Takahashi, AIP Advances **1**, 22103 (2011).

[44] K. Kanetani, K. Sugawara, T. Sato, R. Shimizu, K. Iwaya, T. Hitosugi, and T. Takahashi, Proceedings of the National Academy of Sciences **109**, 19610 (2012).

[45] C. Chamon, Physical Review B **62**, 2806 (2000).

[46] L. Classen, M. M. Scherer, and C. Honerkamp, Phys. Rev. B **90**, 035122 (2014).

[47] C. Weeks and M. Franz, Physical Review B **81**, 85105 (2010).

[48] C.-Y. Hou, C. Chamon, and C. Mudry, Physical Review Letters **98**, 186809 (2007).

[49] C. A. Marianetti and H. G. Yevick, Physical Review Letters **105**, 245502 (2010).

[50] S.-H. Lee, H.-J. Chung, J. Heo, H. Yang, J. Shin, U.-I. Chung, and S. Seo, ACS Nano **5**, 2964 (2011).

[51] G. Giovannetti, M. Capone, J. Van Den Brink, and C. Ortix, Physical Review B **91**, 121417 (2015).

[52] S. Im, H. Im, K. Kim, J. Lee, J. Hwang, S. Mo, and C. Hwang, Advanced Physics Research **2**, 2200091 (2023).

[53] Y. Ye, J. Qian, X.-W. Zhang, C. Wang, D. Xiao, and T. Cao, Nano Letters **23**, 6536 (2023).

[54] A. C. Qu, P. Nigge, S. Link, G. Levy, M. Michiardi, P. L. Spandar, T. Matthé, M. Schneider, S. Zhdanovich, U. Starke, C. Gutiérrez, and A. Damascelli, Science Advances **8**, eabm5180 (2022).

[55] J. W. F. Venderbos, M. Manzardo, D. V. Efremov, J. van den Brink, and C. Ortix, Phys. Rev. B **93**, 045428 (2016).

[56] S. A. Herrera and G. G. Naumis, Phys. Rev. B **104**, 115424 (2021).

[57] X.-Y. Xiong, X.-D. Hu, Q. Zhu, and Z. Li, Physics Letters A **480**, 128957 (2023).

[58] S. A. Herrera and G. G. Naumis, Phys. Rev. B **101**, 205413 (2020).

[59] S. A. Herrera and G. G. Naumis, Phys. Rev. B **102**, 205429 (2020).

[60] A. Santacruz, P. E. Iglesias, R. Carrillo-Bastos, and F. Mireles, Phys. Rev. B **105**, 205405 (2022).

[61] E. Andrade, R. Carrillo-Bastos, M. M. Asmar, and G. G. Naumis, Phys. Rev. B **106**, 195413 (2022).

[62] Y. Mohammadi, ECS Journal of Solid State Science and Technology **10**, 061011 (2021).

[63] Y. Mohammadi, ECS Journal of Solid State Science and Technology **11**, 121004 (2022).

[64] M. A. Mojarro, V. G. Ibarra-Sierra, J. C. Sandoval-Santana, R. Carrillo-Bastos, and G. G. Naumis, Phys. Rev. B **102**, 165301 (2020).

[65] Z. Tajkov, J. Koltai, J. Cserti, and L. Oroszlány, Phys. Rev. B **101**, 235146 (2020).

[66] X. Y. Xu, K. T. Law, and P. A. Lee, Phys. Rev. B **98**, 121406 (2018).

[67] B. Roy and I. F. Herbut, Phys. Rev. B **82**, 035429 (2010).

[68] H. C. Po, L. Zou, A. Vishwanath, and T. Senthil, Phys. Rev. X **8**, 031089 (2018).

[69] Y. Da Liao, Z. Y. Meng, and X. Y. Xu, Phys. Rev. Lett. **123**, 157601 (2019).

[70] S.-M. Huang, Y.-P. Huang, and T.-K. Lee, Phys. Rev. B **101**, 235140 (2020).

[71] A. Blason and M. Fabrizio, Phys. Rev. B **106**, 235112 (2022).

[72] N. B. Kopnin, T. T. Heikkilä, and G. E. Volovik, Phys. Rev. B **83**, 220503 (2011).

[73] Y. Cao, V. Fatemi, S. Fang, K. Watanabe, T. Taniguchi, E. Kaxiras, and P. Jarillo-Herrero, Nature **556**, 43 (2018).

[74] N. Ehlen, M. Hell, G. Marini, E. H. Hasdeo, R. Saito, Y. Falke, M. O. Goerbig, G. Di Santo, L. Petaccia, G. Profeta, and A. Grüneis, ACS Nano **14**, 1055 (2020).

[75] D. Leykam, A. Andreanov, and S. Flach, Advances in Physics: X **3**, 1473052 (2018).

[76] R. Drost, T. Ojanen, A. Harju, and P. Liljeroth, Nature Physics **13**, 668 (2017).

[77] M. M. Al Ezzi, J. Hu, A. Ariando, F. Guinea, and S. Adam, Phys. Rev. Lett. **132**, 126401 (2024).

[78] C. Bao, H. Zhang, X. Wu, S. Zhou, Q. Li, P. Yu, J. Li, W. Duan, and S. Zhou, Phys. Rev. B **105**, L161106 (2022).

[79] A. de Jesús Espinosa-Champo and G. G. Naumis, Journal of Physics: Condensed Matter **36**, 275703 (2024).

[80] S. Deng, A. Simon, and J. Köhler, Journal of Solid State Chemistry **176**, 412 (2003).

[81] P. Roman-Taboada and G. G. Naumis, Phys. Rev. B **95**, 115440 (2017).

[82] R. Bistritzer and A. H. MacDonald, Proceedings of the National Academy of Sciences **108**, 12233 (2011).

[83] U. Mogera and G. U. Kulkarni, Carbon **156**, 470 (2020).

[84] D. Cvetkovic, P. Rowlinson, and S. Simic, *Spectral generalizations of line graphs: On graphs with least eigenvalue-2*, Vol. 314 (Cambridge University Press, 2004).

[85] C. S. Chiu, A. N. Carroll, N. Regnault, and A. A. Houck, Phys. Rev. Res. **4**, 023063 (2022).

[86] A. J. Kollár, M. Fitzpatrick, P. Sarnak, and A. A. Houck, Communications in Mathematical Physics **376**, 1909 (2020).

[87] E. H. Lieb, Phys. Rev. Lett. **62**, 1201 (1989).

[88] B. Sutherland, Physical Review B **34**, 5208 (1986).

[89] J. Vidal, R. Mosseri, and B. Douçot, Phys. Rev. Lett. **81**, 5888 (1998).

[90] D. Bercioux, D. F. Urban, H. Grabert, and W. Häusler, Physical Review A **80**, 063603 (2009).

[91] M. A. Mojarro, V. G. Ibarra-Sierra, J. C. Sandoval-Santana, R. Carrillo-Bastos, and G. G. Naumis, Phys. Rev. B **101**, 165305 (2020).

[92] D. O. Oriekhov, E. V. Gorbar, and V. P. Gusynin, Low Temperature Physics **44**, 1313 (2018).

[93] G. Tarnopolsky, A. J. Kruchkov, and A. Vishwanath, Physical Review Letters **122**, 106405 (2019).

[94] H. L. Yu and Z. Y. Zhai, Modern Physics Letters B **32**, 1850158 (2018).

[95] N. F. Q. Yuan and L. Fu, Physical Review B **98**, 045103 (2018).

[96] E. Illes, J. P. Carbotte, and E. J. Nicol, Physical Review B **92**, 245410 (2015).

[97] C.-D. Han and Y.-C. Lai, Phys. Rev. B **105**, 155405 (2022).

[98] A. Iurov, L. Zhemchuzhna, G. Gumbs, and D. Huang, Phys. Rev. B **107**, 195137 (2023).

[99] L.-L. Ye, C.-D. Han, and Y.-C. Lai, Applied Physics Letters **124**, 060501 (2024).

[100] T. Biswas and T. Kanti Ghosh, Journal of Physics: Condensed Matter **28**, 495302 (2016).

[101] L. E. Sánchez-González, M. A. Mojarro, J. A. Maytorena, and R. Carrillo-Bastos, Phys. Rev. B **111**, 115417 (2025).

[102] P. R. Wallace, Physical Review **71**, 622 (1947).

[103] A. H. Castro Neto, F. Guinea, N. M. R. Peres, K. S. Novoselov, and A. K. Geim, Reviews of Modern Physics **81**, 109 (2009).

[104] C. Bena and G. M. Baux, New Journal of Physics **11**, 095003 (2009).

[105] S. Reich, J. Maultzsch, C. Thomsen, and P. Ordejón, Physical Review B **66**, 035412 (2002).

[106] A. Manchon, H. C. Koo, J. Nitta, S. M. Frolov, and R. A. Duine, Nature Materials 2015 14:9 **14**, 871 (2015).

[107] G. G. Naumis, Revista Mexicana de Física **67**, 22 (2021).

[108] A. C. Qu, P. Nigge, S. Link, G. Levy, M. Michiardi, P. L. Spandar, T. Matthé, M. Schneider, S. Zhdanovich, U. Starke, C. Gutiérrez, and A. Damascelli, Science Advances **8** (2022), 10.1126/sciadv.abm5180.

[109] C. Wang, H. Wang, Q. Tian, J. Zong, X. Xie, W. Chen, Y. Zhang, K. Wang, X. Qiu, L. Wang, F. Li, H. Zhang, and Y. Zhang, The Journal of Physical Chemistry Letters **13**, 9396 (2022), pMID: 36190902.

[110] E. Andrade, R. Carrillo-Bastos, and G. G. Naumis, Journal of Physics: Condensed Matter **37**, 193003 (2025).

[111] W. P. Su, J. R. Schrieffer, and A. J. Heeger, Phys. Rev. Lett. **42**, 1698 (1979).

[112] S. G. y. García, Y. Betancur-Ocampo, F. Sánchez-Ochoa, and T. Stegmann, Nano Letters **24**, 2322 (2024), pMID: 38329068.

[113] Y. Chen, S. Xu, Y. Xie, C. Zhong, C. Wu, and S. B. Zhang, Phys. Rev. B **98**, 035135 (2018).

[114] H. Bruus and K. Flensberg, *Many-body quantum theory in condensed matter physics: an introduction* (Oxford university press, 2004).

[115] R. Kubo, Journal of the Physical Society of Japan **12**, 570 (1957).

[116] X. Kuang, P. A. Pantaleón Peralta, J. Angel Silva-Guillén, S. Yuan, F. Guinea, and Z. Zhan, Journal of Physics: Condensed Matter **36**, 173001 (2024).

[117] T. Low and P. Avouris, ACS Nano **8**, 1086 (2014), pMID: 24484181.

[118] J. Aizpurua, T. Taubner, F. J. G. de Abajo, M. Brehm, and R. Hillenbrand, Opt. Express **16**, 1529 (2008).

[119] A. Polman, M. Kociak, and F. J. García de Abajo, Nature materials **18**, 1158 (2019).

[120] X. Yan, C. Liu, C. A. Gadre, L. Gu, T. Aoki, T. C. Lovejoy, N. Dellby, O. L. Krivanek, D. G. Schlom, R. Wu, *et al.*, Nature **589**, 65 (2021).

[121] S. S. Sunku, G. X. Ni, B. Y. Jiang, H. Yoo, A. Sternbach, A. S. McLeod, T. Stauber, L. Xiong, T. Taniguchi, K. Watanabe, P. Kim, M. M. Fogler, and D. N. Basov, Science **362**, 1153 (2018).

[122] G. D. Mahan, *Many-particle physics* (Springer Science & Business Media, 2013).

[123] Y. A. Il'inskii and L. V. Keldysh, *Electromagnetic response of material media* (Springer Science & Business Media, 2013).

[124] A. W. W. Ludwig, M. P. A. Fisher, R. Shankar, and G. Grinstein, Phys. Rev. B **50**, 7526 (1994).

[125] R. Resta, Journal of Physics: Condensed Matter **30**, 414001 (2018).

[126] H. A. Kramers, *La diffusion de la lumiere par les atomes* (1928).

[127] R. de L. Kronig, J. Opt. Soc. Am. **12**, 547 (1926).

[128] J. S. Toll, Phys. Rev. **104**, 1760 (1956).

[129] M. Fox, *Optical properties of solids*, Vol. 3 (Oxford university press, 2010).

[130] K. Aly, Physica B: Condensed Matter **655**, 414723 (2023).

[131] L. A. Falkovsky, Journal of Physics: Conference Series **129**, 012004 (2008).

[132] Q. Zhou, Q. Qiu, and Z. Huang, Optics Laser Technology **157**, 108558 (2023).

[133] A. Montanaro, G. Piccinini, V. Mišeikis, V. Sorianello, M. A. Giambra, S. Soresi, L. Giorgi, A. D'Errico, K. Watanabe, T. Taniguchi, *et al.*, Nature Communications **14**, 6471 (2023).

[134] J. Wang, Y. Xu, and S.-C. Zhang, Phys. Rev. B **90**, 054503 (2014).

[135] J. C. Garcia, D. B. de Lima, L. V. C. Assali, and J. F. Justo, The Journal of Physical Chemistry C **115**, 13242 (2011).

[136] R. Quhe, R. Fei, Q. Liu, J. Zheng, H. Li, C. Xu, Z. Ni, Y. Wang, D. Yu, Z. Gao, *et al.*, Scientific reports **2**, 853 (2012).

[137] H. Sahin and F. M. Peeters, Phys. Rev. B **87**, 085423 (2013).

[138] Q. Pang, C. ling Zhang, L. Li, Z. qiang Fu, X. mei Wei, and Y. ling Song, Applied Surface Science **314**, 15 (2014).

[139] M. Ye, R. Quhe, J. Zheng, Z. Ni, Y. Wang, Y. Yuan, G. Tse, J. Shi, Z. Gao, and J. Lu, Physica E: Low-dimensional Systems and Nanostructures **59**, 60 (2014).

[140] A. Iurov, L. Zhemchuzhna, G. Gumbs, and D. Huang, Physical Review B **107**, 195137 (2023).

[141] M. Yarmohammadi, AIP Advances **6**, 085008 (2016).

[142] J. Horng, C.-F. Chen, B. Geng, C. Girit, Y. Zhang, Z. Hao, H. A. Bechtel, M. Martin, A. Zettl, M. F. Crommie, Y. R. Shen, and F. Wang, Phys. Rev. B **83**, 165113 (2011).

[143] M. A. Mojarro, R. Carrillo-Bastos, and J. A. Maytorena, Phys. Rev. B **103**, 165415 (2021).

[144] T. G. Pedersen, A.-P. Jauho, and K. Pedersen, Phys. Rev. B **79**, 113406 (2009).

[145] A. Carvalho, R. M. Ribeiro, and A. H. Castro Neto, Phys. Rev. B **88**, 115205 (2013).

[146] L. Mennel, V. Smejkal, L. Linhart, J. Burgdörfer, F. Libisch, and T. Mueller, Nano letters **20**, 4242 (2020).

[147] K. F. Mak, M. Y. Sfeir, Y. Wu, C. H. Lui, J. A. Misewich, and T. F. Heinz, Phys. Rev. Lett. **101**, 196405 (2008).

[148] B. Dóra, J. Kailasvuori, and R. Moessner, Phys. Rev. B **84**, 195422 (2011).

[149] M. Koshino and Y.-W. Son, Phys. Rev. B **100**, 075416 (2019).

[150] H. Ochoa and A. Asenjo-Garcia, Phys. Rev. Lett. **125**, 037402 (2020).

[151] M. A. Mojarro, R. Carrillo-Bastos, and J. A. Maytorena, Phys. Rev. B **108**, L161401 (2023).

[152] P. F. Maldague, Surface Science **73**, 296 (1978).

Publications and presentations

The results of this dissertation have been disseminated through academic presentations and peer-reviewed publications. A summary of the main outputs derived from this research is presented below.

Publications

- **Luis. E. Sánchez-González**, M. A. Mojarro, Jesús A. Maytorena and R. Carrillo-Bastos. *Band structure and optical response of Kekulé-modulated α-$\mathcal{T}_3$ model.* Phys. Rev B. Mar 2025. DOI: https://doi.org/10.1103/PhysRevB.111.115417 (Chapter 4 and 5)

Presentations

- Oral presentation: APS Global Physics Summit 2025: March Meeting, Anaheim, California, US, march 2025. Title: *Band structure and optical response of Kekulé-modulated $\alpha - \mathcal{T}_3$ model*
- Oral presentation: Seminario del departamento de Optica. Optics Department of CICESE. January 2025 Title: *Respuesta óptica de materiales de Dirac bidimensionales.*
- Poster: LXVII Congreso Nacional de Física, Universidad Autónoma de Chihuahua, octubre 2024. Title: *Respuesta óptica del modelo $\alpha - \mathcal{T}_3$ con periodicidad Kekulé.*
- Poster: Symposium of Nanoscience and Nanomaterials 2024, Centro de Nanociencias y Nanotecnología UNAM, Ensenada, BC, MX, april 2024. Title: *Kekulé-modulated $\alpha - \mathcal{T}_3$ model*